

Tesis Doctoral

# Turbulencia Hall-MHD en un campo magnético fuerte

Martín, Luis N.

2013

Este documento forma parte de la colección de tesis doctorales y de maestría de la Biblioteca Central Dr. Luis Federico Leloir, disponible en [digital.bl.fcen.uba.ar](http://digital.bl.fcen.uba.ar). Su utilización debe ser acompañada por la cita bibliográfica con reconocimiento de la fuente.

This document is part of the doctoral theses collection of the Central Library Dr. Luis Federico Leloir, available in [digital.bl.fcen.uba.ar](http://digital.bl.fcen.uba.ar). It should be used accompanied by the corresponding citation acknowledging the source.

Cita tipo APA:

Martín, Luis N.. (2013). Turbulencia Hall-MHD en un campo magnético fuerte. Facultad de Ciencias Exactas y Naturales. Universidad de Buenos Aires.

Cita tipo Chicago:

Martín, Luis N.. "Turbulencia Hall-MHD en un campo magnético fuerte". Facultad de Ciencias Exactas y Naturales. Universidad de Buenos Aires. 2013.

**EXACTAS** UBA

Facultad de Ciencias Exactas y Naturales



**UBA**

Universidad de Buenos Aires



UNIVERSIDAD DE BUENOS AIRES  
Facultad de Ciencias Exactas y Naturales  
Departamento de Física

# Turbulencia Hall-MHD en un campo magnético fuerte

Trabajo de Tesis para optar por el título de Doctor  
de la Universidad de Buenos Aires en el área Ciencias Físicas

**Lic. Luis N. Martin**

Director de Tesis: Dr. Pablo Dmitruk  
Consejero de estudios: Dra. Cristina Caputo  
Lugar de Trabajo: Dpto. de Física FCEYN, UBA

BUENOS AIRES, 2013



---

## Resumen

En términos generales existen dos perspectivas para modelar la dinámica de los plasmas. Por un lado están los modelos cinéticos y por el otro los modelos de medios continuos (o modelos de fluidos). La teoría cinética describe a los plasmas desde la naturaleza microscópica del sistema. Las teorías de fluidos por otro lado describen de manera natural los fenómenos a escalas macroscópicas.

La mayor complicación del estudio de la turbulencia magnetohidrodinámica (y también la hidrodinámica) es que es un problema de multiescalas. Los rangos de escala que están en los extremos (macro y micro) son claros dominios de una y otra teoría, sin embargo las escalas que se encuentran entre las escalas MHD y la escala de Kolmogorov (o de disipación) son un rango controversial al respecto.

En esta tesis se introducen efectos cinéticos en la magnetohidrodinámica de medios continuos, a través de modelos de dos fluidos que consideran la separación entre iones y electrones. En particular, se desarrolla un modelo aproximado de dos fluidos para plasmas con campo magnético fuerte que presenta importantes ventajas computacionales. El interés en el efecto del término Hall con campo magnético fuerte está motivado por las observaciones geofísicas, astrofísicas y la implementación tecnológica de confinamiento por medio de guías magnéticas.

El primer paso consistió en testear el modelo aproximado frente al modelo Hall-MHD general. Luego desarrollamos un estudio detallado que incluyó múltiples puntos de vista. Mostramos que el efecto Hall afecta los valores de las magnitudes globales y sus tiempos característicos. La distribución de energía por escalas se ve también modificada, incrementándose el rango de escalas disipativas. Se modifican las estructuras del flujo cambiando su forma y tamaño en las escalas comprendidas entre el ion skin depth (o escala de Hall) y la escala de Kolmogorov. Se reduce la intermitencia espacial y la autosimilaridad del flujo se incrementa tendiendo a la monofractalidad. Se analiza el efecto sobre la formación y estructura de las hojas de corriente. Se analizan las propiedades estadísticas del flujo, en particular la fractalidad y el efecto sobre la dimensionalidad de las estructuras responsables de la disipación. Finalmente, extendemos los primeros efectos cinéticos más allá del efecto Hall introduciendo la inercia electrónica y presentamos resultados preliminares que muestran que la masa electrónica afecta la dinámica más allá de los efectos del término Hall.

Palabras clave: Efecto Hall, Turbulencia, Magnetohidrodinámica, MHD, Hall-MHD

---

## Abstract

### Hall-MHD turbulence in a strong magnetic field

There are broadly two approaches for modeling the dynamics of plasma. On one side are the kinetic theory models and on the other continuum models (or fluid models). The kinetic theory describes the plasmas from a microscopic point of view. On the other hand, the fluid models describe phenomena at macroscopic scales.

The major complication in the study of magnetohydrodynamic turbulence (and hydrodynamic) is that it is a multi-scale problem. The scale ranges that are at the extremes (macro and micro) are clearly domains of one theory or the other, however, scales between MHD scale and Kolmogorov (or dissipation) scales are controversial. In this thesis we introduce the first kinetic effects into the continuous media magnetohydrodynamic description, considering a two-fluid model, which takes into account the separation between ions and electrons.

In particular, we develop an approximate model of two fluids for plasmas with a strong magnetic fields, where variations along the direction of the magnetic field are smoother than transverse variations. This approximate model shows important computational advantages against the fully general tridimensional Hall MHD model. The interest in the effect of the Hall term in a strong magnetic field is in turn motivated by geophysical and astrophysical observations, and technological implementation of confinement through magnetic guides.

The first step was to test the approximate model with the full general Hall-MHD model. We then developed a detailed study which included multiple points of view. We showed that the Hall effect affects the values global quantities and their characteristic times. It also modifies the distribution of energy among scales, increasing the range of dissipative scales. It affects flow structures changing its shape and size between the ion skin depth (Hall scale) and Kolmogorov scale. The intermittency is reduced and self-similarity of the flow increases approaching monofractality. We analyzed the effects on the formation and structure of current sheets (important for the energy dissipation). We studied the statistical properties of the flow, particularly the fractality and the effect on the dimensionality of the structures responsible for the dissipation.

Finally, we extend the first kinetic effects beyond the Hall effect, considering electron inertia and introduce preliminary results showing that the electronic mass affects the dynamics beyond the effects of the Hall term.

Keywords: Hall Effect, turbulence, magnetohydrodynamics, MHD, Hall-MHD.

---

## Agradecimientos

En primer lugar agradezco a mi madre y mi padre; por darme la mejor y mas divertida etapa de mi vida, mi niñez. Por enseñarme que el mejor contexto para desarrollarse es el de la libertad y que la técnica para generarlo es el respeto.

A Leonardo y Liliana Winograd, por abrirme las puertas de su casa y su familia. Por ayudarme en toda mi carrera de grado.

Agradezco a los argentinos que con sus impuestos pagaron mi educación y la de miles de académicos y profesionales. A la universidad de Buenos Aires y en particular al departamento de Física de la Facultad de ciencias exactas y naturales. Al Conicet y a la Agencia Nacional de Promoción Científica y Tecnológica.

A Pablo Dmitruk, un director magistral. Me dejo equivocarme en cada empecinamiento que tuve y estuvo siempre presente para darle solución sin reprocharme nada. Responsabilidad y excelencia académica son sus principales virtudes. A Pablo Mininni, por discutir conmigo de manera incansable. Por enseñarme física y ciencia en todo los niveles. Por estar siempre dispuesto a colaborar. A Danil Gomez, por ser un ejemplo, de ética, trabajo y esfuerzo. Por ser un líder ejemplar que siempre se preocupa por los jóvenes del grupo. Considero importante mencionar que Daniel ha sido un importante formador de recursos humanos. Al grupo de flujos astrofísicos, por darme el ambiente para poder desarrollarme, el apoyo científico, moral y económico. A mi compañeros de trabajo, Tomas, Paola, y Nahuel. Cada uno de ellos siempre dispuestos a darme una mano con mis problemas académicos/laborales.

A Juan, el mas viejo de mis amigos. Por estar siempre en todo, por darme trabajo cuando lo necesite, por bancarme en mis delirios, y por la mudanza de la semana pasada. A Emilio, por ser lo mas parecido a un hermano mayor (teniendo un año menos que yo). Por ser comprensivo pero nunca obsecuente. A Fabricio por ver lo peor de mi persona y aun así seguir siendo mi amigo. Y también porque me dio las llaves de su departamento (mas que nada por eso).

A Veronica, mi prima, mi compañera de apartamento, la hermana mayor que no tuve. Ella fue de las personas que mas me han ayudado en mis años de estudio. A Jeremias y a mis hermanos, Lucas y Federico, las personas que mas me conocen.

A la mujer que amo, Brooke May. Quien siempre esta apoyandome con optimismo y paciencia. Por reírse de mis chiste, por enseñarme a ver las cosas desde otro lugar. Por cuidarme. Con ella todo es mas divertido.



# Contents

<b>Introduction</b>	<b>1</b>
<b>1 The background</b>	<b>9</b>
1.1 Models	10
1.1.1 The Hall-MHD equations	10
1.1.2 Hall-MHD in a strong magnetic field: RHMHD	13
1.1.2.1 RHMHD	13
1.1.2.2 Weak compressible RHMHD	15
1.2 Applications	16
1.2.1 Application of RHMHD to solar wind turbulence	16
1.2.2 Application of RMHD to coronal heating	20
1.3 Numerical simulations	23
1.3.1 Equations	23
1.3.2 Numerical codes	25
<b>2 Testing the model</b>	<b>31</b>
2.1 Simulations	32
2.1.1 Set up	32
2.1.2 Initial Conditions	32
2.2 Incompressible RHMHD Vs Compressible RHMHD	33
2.3 Anisotropic initial conditions	37
2.4 Isotropic initial conditions	42
2.5 Conclusions	46
<b>3 Hall-magnetohydrodynamic with a strong guide magnetic field</b>	<b>51</b>
3.1 Set up	51

## CONTENTS

---

3.2	Global magnitudes . . . . .	52
3.3	Energy spectrum . . . . .	55
3.4	Current sheets . . . . .	57
3.5	Conclusions . . . . .	62
<b>4</b>	<b>Intermittency</b> . . . . .	<b>65</b>
4.1	Hall effect and intermittency . . . . .	65
4.2	Set up . . . . .	67
4.3	Measures of intermittency . . . . .	67
4.4	Energy spectrum: Inertial range . . . . .	69
4.5	Structure functions and scaling exponents . . . . .	71
4.6	Probability density functions . . . . .	77
4.7	Effect of resolution . . . . .	78
4.8	Conclusions . . . . .	82
<b>5</b>	<b>Statistical properties</b> . . . . .	<b>87</b>
5.1	A brief review . . . . .	87
5.2	Set up . . . . .	89
5.3	Qualitative approach . . . . .	89
5.4	The signed Measure and the cancellation exponent . . . . .	89
5.5	Cancellation analysis in turbulent plasmas . . . . .	93
5.6	Conclusions . . . . .	101
<b>6</b>	<b>Beyond the Hall effect: electron inertia</b> . . . . .	<b>107</b>
6.1	Electron Inertia Hall-MHD model (EIHMHD) . . . . .	107
6.2	2.5D Setup . . . . .	109
6.2.1	Linear modes . . . . .	110
6.2.2	Ideal invariants in 2.5D . . . . .	111
6.3	Preliminary results for turbulence . . . . .	112
<b>7</b>	<b>Concluding remarks and perspectives</b> . . . . .	<b>113</b>

# Introduction

The MHD models (one-fluid models) [1, 2] are important frameworks for the understanding of the large scale dynamics of a plasma. However, these models fail to describe plasma phenomena with characteristic length scales smaller than the ion skin depth  $\rho_{ii} = c/\omega_{pi}$  (with  $\omega_{pi}$  the ion plasma frequency and  $c$  speed of light). At this level, the Hall effect, which takes into account the separation between electrons and ions, becomes relevant. To describe this regime is common to use the Hall MHD approximation, which considers two-fluid effects through a generalized Ohm's law which includes the Hall current. In an ideal plasma, the Hall current causes the magnetic field to become frozen in the electron flow instead of being carried along with the bulk velocity field (as in MHD). Another relevant feature of the ideal Hall MHD description is the self-consistent presence of parallel (to the magnetic field) electric fields, which can therefore accelerate particles.

Among various kinetic corrections to magnetohydrodynamics models (MHD), the Hall effect [3, 4] has been considered of particular importance in numerous studies: magnetic reconnection [5, 6, 7, 8, 9], dynamo mechanisms [10], accretion disks [11, 12] and physics of turbulent regimes [13, 14, 15, 16] are some of the main examples. The Hall parameter in this regime is  $\epsilon = \rho_{ii}/L$ , the ratio of the ion skin depth  $\rho_{ii}$  to the characteristic (large) scale of the turbulence  $L$ . Through this parameter we can vary the intensity of Hall effect and/or modify their spatial action range.

There are a number of applications for which it is reasonable to consider that the plasma is embedded in a strong and uniform magnetic field, such as in fusion devices or geophysical and astrophysical plasmas. Therefore, it is important to find new tools and methods to characterize systems where both the Hall effect and a strong mean magnetic field are relevant. One of such tools are the direct numerical simulations. The full MHD models are computationally demanding and this demand is increased when the Hall effect is considered. This is because to see the influence of the Hall effect a larger range of scales is needed (thus more spatial resolution is required). Also, the Hall effect introduces high frequency waves (whistler waves, with

a dispersion relation going as the square of the wavenumber) changing the CFL [17] stability condition to a more restrictive one, requiring a smaller time step in the numerical simulations.

The presence of a strong mean magnetic field may simplify part of the dynamics. For one-fluid MHD, the existence of a strong magnetic field is often exploited to yield a simpler model: the so-called reduced MHD approximation (RMHD; see refs. [18] and [19]). In this approximation, the fast compressional Alfvén mode is eliminated, while the shear Alfvén and the slow magnetosonic modes are retained [20]. The RMHD equations have been used to investigate a variety of problem such as current sheet formation [21, 22], nonstationary reconnection [23, 24], the dynamics of coronal loops [25, 26], and the development of turbulence [27]. The self-consistency of the RMHD approximation has been analyzed in ref. [28]. Moreover, it has been studied the validity of the RMHD equations by directly comparing its predictions with the compressible MHD equations in a turbulent regime [29]. More recently, it has extended the “reduced” approximation to include two-fluid effects [30], giving rise to the reduced Hall-MHD description (RHMHD, see also [31]). A comparative study of numerical simulations of the compressible three-dimensional Hall-MHD equations and the reduced approximation, has recently confirmed the validity of the RHMHD description in the asymptotic limit of strong external magnetic fields [32].

The properties of small scales structures in magnetohydrodynamic (MHD) and Hall-MHD (HMHD) turbulence have been the subject of conflicting results and of several debates. In particular, much attention has been paid in the literature to the geometrical properties of current sheets in HMHD, as these structures are associated with magnetic flux reconnection and magnetic energy dissipation, processes of uttermost importance in astrophysics and space physics [33, 34, 35, 36]. Therefore the debate on the effect of the Hall term on the generation of turbulent structures is still open. For example, some recent numerical simulations have indicated that current sheets in presence of Hall effect become wider than in MHD (see, e.g., [37]), while, on the contrary, other studies have observed formation of thinner structures when Hall effect increases, suggesting that HMHD is more intermittent than MHD [38]. This was also observed in solar wind turbulence, *e.g.* using the Cluster spacecraft magnetic data [39, 40]. Incidentally, other instances of solar wind observations of high-frequency magnetic field fluctuations from the same spacecraft indicated that while large scales are compatible with multifractal intermittent turbulence, small scales show non-Gaussian self-similarity [41].

The quantitative measure of the intermittency is crucial to understand the topological distribution of dissipation in magneto-fluids and plasmas, and it can also provide constraints for theoretical study of phenomena such as magnetic energy dissipation and reconnection. It is thus not clear whether HMHD small scale structures are thinner than in MHD, making HMHD more intermittent than MHD, or, on the contrary, they are more space filling, causing intermit-

tency to decrease because of the Hall effect.

In this work we want to study the general effect of the Hall term in magnetohydrodynamic turbulence in plasmas embedded on strong uniform magnetic field, through numerical simulations. We studied the effect of this term on the dynamics of global magnitudes, energy cascade, the characteristic scales and the intermittency of the flow. Also we carried out a study about the topology of the fields, characterizing the dimensionality of the structures that are formed within the flow.

The thesis is organized as follows:

**Chapter 1** is dedicated to contextualize this thesis, by developing the models and numerical codes. We will review the basic features of both two-fluid and one-fluid magnetohydrodynamics, and focus on two particular applications: the turbulent heating of coronal active regions and the dynamics of the solar wind.

**Chapter 2** is devoted to test a new model derived in a recent work by Gomez et al. [30]. This model consists of a system of reduced Hall-MHD (RHMHD) equations derived from the incompressible Hall MHD following the same asymptotic procedure, which is employed to obtain the conventional RMHD from MHD. The resulting set will describe the slow dynamics of a plasma (with Hall currents) embedded in a strong external magnetic field and will naturally include new features such as the presence of a parallel electric field. Also we have made minor modifications to the model to describe the compressibility effects [31] and we tested its performance. Our goal here is to test the RHMHD model [30], which is aimed at reducing the computational cost.

In **Chapter 3** we study the general effect of the Hall term in magnetohydrodynamic turbulence in plasmas embedded in a strong uniform magnetic field. We studied the effect of this term on the dynamics of global magnitudes, the cascade of energy, the characteristic scales of the flow and the typical structures (current sheet).

In **Chapter 4** we present a detailed study of intermittency in the velocity and magnetic field fluctuations. Considering the solar wind as a motivation, the data for the analysis stem from numerical simulations of MHD and HMHD turbulence with a guide field. We use the reduced MHD and reduced HMHD models to generate data under the approximation of a strong guide field. Then, structure functions and PDFs of the fields are computed, for increments in the direction perpendicular to the guide field. To reduce errors, an average of the structure functions for

several directions perpendicular to the guide field is computed using the  $SO(2)$  decomposition.

In **Chapter 5** we carried out a qualitative analysis of the characteristics structures and their features with respect to the magnitude of the Hall effect. In order to gain more insight on the actual effect of the Hall term on flow structures, here we study the geometrical properties of the vorticity and current field, using an explicit and quantitative approach, the cancellation exponents.

In **Chapter 6** we go beyond the Hall-MHD model by developing a two-fluid model for a fully ionized hydrogen plasma not neglecting the electron mass.

In **Chapter 7** we list our conclusions.

# Bibliography

- [1] P. A. Davidson, *An Introduction to Magnetohydrodynamics*, (Cambridge University Press, 2001). [1](#)
- [2] H. Goedbloed, S. Poedts, *Principles of Magnetohydrodynamics*, (Cambridge University Press, 2004). [1](#)
- [3] N. A. Krall and A. W. Trivelpiece, in *Principles of Plasma Physics* (McGraw-Hill, New York, 1973), p. 89. [1](#)
- [4] L. Turner, *IEEE Trans. Plasma Sci.* **PS14**, 849 (1986). [1](#)
- [5] J. Birn, J. F. Drake, M. A. Shay et al., *J. Geophys. Res.* **106**, 3715 (2001). [1](#)
- [6] X. Wang, A. Bhattacharjee, and Z. W. Ma, *Phys. Rev. Lett.* **87**, 265003 (2001). [1](#)
- [7] F. Mozer, S. Bale, and T. D. Phan, *Phys. Rev. Letter.* **89**, 015002 (2002). [1](#)
- [8] D. Smith, S. Ghosh, P. Dmitruk, and W. H. Matthaeus. *Geophys. Res Lett.* **31**, L02805 (2004). [1](#)
- [9] L. F. Morales, S. Dasso, and D. O. Gomez, *J. Geophys. Res.* **110**, A04204 (2005). [1](#)
- [10] P. D. Mininni, D. O. Gomez, and S. M. Mahajan, *Astrophys. J.* **584**, 1120 (2003). [1](#)
- [11] M. Wardle, *Mon. Not. R. Astron. Soc.* **303**, 239 (1999). [1](#)
- [12] S. A. Balbus and C. Terquem, *Astrophys. J.* **552**, 235 (2001). [1](#)
- [13] W. H. Matthaeus, P. Dmitruk, D. Smith, S. Ghosh, and S. Oughton, *Geophys. Res. Lett.* **30**, 2104 (2003). [1](#)
- [14] P. D. Mininni, D. O. Gomez, and S. M. Mahajan, *Astrophys. J.* **619**, 1019 (2005). [1](#)

- [15] S. Galtier, *J. Plasma Phys.* **72**, 721 (2006). [1](#)
- [16] P. Dmitruk and W. H. Matthaeus, *Phys. Plasmas* **13**, 042307 (2006). [1](#)
- [17] C Canuto, A Quarteroni , Approximation results for orthogonal polynomials in Sobolev spaces, *Math. Comp.* **38**, 67, (1982). [2](#)
- [18] H. R. Strauss, *Phys. Fluids* **19**, 134 (1976) [2](#)
- [19] D. C. Montgomery, *Phys. Scr.*, T **T2/1**, 83 (1982) [2](#)
- [20] G. P. Zank and W. H. Matthaeus, *J. Plasma Phys.* **48**, 85 (1992). [2](#)
- [21] A. A. van Ballegooijen, *Astrophys. J.* **311**, 1001 (1986). [2](#)
- [22] D. W. Longcope, and R. N. Sudan, *Astrophys. J.* **437**, 491 (1994). [2](#)
- [23] D. L. Hendrix and G. van Hoven, *Astrophys. J.* **467**, 887 (1996). [2](#)
- [24] L. Milano, P. Dmitruk, C. H. Mandrini, D. O. Gómez, and P. Demoulin, *Astrophys. J.* **521**, 889 (1999). [2](#)
- [25] D. O. Gómez, and C. Ferro Fontán, *Astrophys. J.* **394**, 662 (1992). [2](#)
- [26] P. Dmitruk and D. O. Gómez, *Astrophys. J. Lett.* **527**, L63 (1999). [2](#)
- [27] P. Dmitruk, D. O. Gómez, and W. H. Matthaeus, *Phys. Plasmas* **10**, 3584 (2003). [2](#)
- [28] S. Oughton, P. Dmitruk, and W. H. Matthaeus, *Phys. Plasmas* **11**, 2214 (2004). [2](#)
- [29] P. Dmitruk, W. H. Matthaeus, and S. Oughton, *Phys. Plasmas* **12**, 112304 (2005). [2](#)
- [30] D. O. Gómez, S. M. Mahajan, and P. Dmitruk, *Phys. Plasma* **15**, 102303 (2008). [2](#), [3](#)
- [31] N. H. Bian and D. Tsiklauri, *Phys. Plasma* **16**, 064503 (2009). [2](#), [3](#)
- [32] L. N. Martin, P. Dmitruk, *Phys. Plasma* **17**, 112304 (2010). [2](#)
- [33] J. Birn and M. Hesse, *J. Geophys. Res.* **106**, 3737 (2001). [2](#)
- [34] Y. Ren, M. Yamada, S. Gerhardt, H. Ji, R. Kulsrud, and A. Kuritsyn, *Phys. Rev. Lett.* **95**, 55003 (2005). [2](#)
- [35] M. Shay, J. F. Drake, B. N. Rogers, and R. E. Denton, *J. Geophys. Res.* **106**, 3759 (2001). [2](#)
- [36] P. Dmitruk and W. H. Matthaeus, *Phys. Plasmas* **13**, 2307 (2006). [2](#)
- [37] L. N. Martin, P. Dmitruk, and D. O. Gómez, *Phys. Plasmas*, **19**, 052305 (2012). [2](#)

- [38] S. Donato, S. Servidio, P. Dmitruk, V. Carbone, M. A. Shay, and P. A. Cassak, *Phys. Plasmas*, **19**, 092307 (2012). [2](#)
- [39] O. Alexandrova, V. Carbone, P. Veltri, and L. Sorriso-Valvo, *Pl. and Space Sc.* **55**, 2224 (2007). [2](#)
- [40] O. Alexandrova, V. Carbone, P. Veltri, and L. Sorriso-Valvo, *Astrophys. J.* **674**, 1153 (2008). [2](#)
- [41] K. H. Kiyani, S. C. Chapman, Yu. V. Khotyaintsev, and M. W. Dunlop and F. Sahraoui, *Phys. Rev. Lett.* **103**, 075006 (2010). [2](#)



# Chapter 1

## The background

[1]

### Contents

---

<b>1.1 Models</b>	<b>10</b>
1.1.1 The Hall-MHD equations	10
1.1.2 Hall-MHD in a strong magnetic field: RHMHD	13
<b>1.2 Applications</b>	<b>16</b>
1.2.1 Application of RHMHD to solar wind turbulence	16
1.2.2 Application of RMHD to coronal heating	20
<b>1.3 Numerical simulations</b>	<b>23</b>
1.3.1 Equations	23
1.3.2 Numerical codes	25

---

Magnetohydrodynamics (MHD) is a reasonable theoretical framework to describe the large-scale dynamics of a plasma, which is also known as one-fluid MHD. Two-fluid effects can be considered through a generalized Ohm's law which includes the Hall current, which is required for phenomena with characteristic length scales comparable or smaller than the ion skin depth  $c/\omega_{pi}$  ( $c$ : speed of light,  $\omega_{pi}$ : ion plasma frequency). In an ideal plasma, the Hall current causes the magnetic field to become frozen in the electron flow instead of being carried along with the bulk velocity field.

In astrophysical plasmas, a strong external magnetic field is often present, thus breaking down the isotropy of the problem and eventually causing important changes in the dynamics of these plasmas. For one-fluid MHD, the presence of an external magnetic field gave rise to the so-called reduced MHD approximation (RMHD, see [2, 3]). The RMHD equations have

## 1. The background

---

been used in a variety of astrophysical applications, such as current sheet formation [4, 5], non-stationary reconnection [6, 7], the dynamics of coronal loops [8, 9] or the development of turbulence [10]. It has numerically confirmed the validity of the RMHD equations by directly comparing its predictions with the compressible MHD equations in a turbulent regime [11]. More recently, [12] extended the “reduced” approximation to include two-fluid effects, giving rise to the reduced Hall-MHD description (RHMHD, see also [13]). A comparative study of numerical simulations of the compressible three-dimensional Hall-MHD equations and the reduced approximation, has recently confirmed the validity of the RHMHD description in the asymptotic limit of strong external magnetic fields [14].

We organize the chapter as follows. After introducing the Hall-MHD set of equations in 1.1.1, we perform the asymptotic expansion corresponding to the dynamics of a plasma embedded in a strong external magnetic field in 1.1.2, and derive the set of RHMHD equations. In 1.2.1 we integrate the RHMHD to simulate the development of turbulence in the solar wind. More specifically, we show that the presence of the Hall effect causes non-negligible changes in the energy power spectrum and also discuss the consequences of an electric field component which is parallel to the magnetic field. We also applied the one-fluid version of these equations (i.e. the RMHD equations) to simulate the internal dynamics of loops of the solar corona. The main results from these simulations are summarized in 1.2.2, showing the development of a turbulent regime in these loops, which enhances Joule dissipation to levels consistent with the energy requirements to heat active regions. Finally, in 1.3.2 we describe the codes to numerically integrate the equations.

### 1.1 Models

#### 1.1.1 The Hall-MHD equations

The large-scale dynamics of a multispecies plasma can be described through fluid equations for each species  $s$  (see for instance [15])

$$\partial_t n_s + \nabla \cdot (n_s \mathbf{u}_s) = 0 \quad (1.1)$$

$$m_s n_s \frac{d\mathbf{u}_s}{dt} = n_s q_s (\mathbf{E} + \frac{1}{c} \mathbf{u}_s \times \mathbf{b}) - \nabla p_s + \nabla \cdot \sigma_s + \sum_{s'} R_{ss'} \quad (1.2)$$

where  $m_s, q_s$  are the individual mass and charge of particles of species  $s$ ,  $n_s, \mathbf{u}_s, p_s$  are their particle density, velocity field and scalar pressure respectively, while  $\sigma_s$  is the viscous stress tensor and  $R_{ss'}$  is the rate of momentum (per unit volume) gained by species  $s$  due to collisions with species  $s'$ ;  $\mathbf{E}$  and  $\mathbf{b}$  are respectively the electric and magnetic fields and convective derivative  $\frac{d\mathbf{u}_s}{dt} = \partial_t \mathbf{u}_s + (\mathbf{u}_s \cdot \nabla) \mathbf{u}_s$  was used. In the presence of a strong magnetic field, pressure might

depart from scalar and become anisotropic (i.e.  $p_{\parallel} \neq p_{\perp}$ ), but we are neglecting this effect throughout this paper. The momentum exchange  $R_{ss'}$  rate is proportional to the relative speed between both species and is given by

$$R_{ss'} = -m_s n_s \nu_{ss'} (\mathbf{u}_s - \mathbf{u}_{s'}) \quad (1.3)$$

where  $\nu_{ss'}$  is the collision frequency of an  $s$ -particle against particles of species  $s'$ . Since the total momentum must of course be conserved, the corresponding exchange rates satisfy  $R_{s's} = -R_{ss'}$ , from which it follows that collision frequencies must obey  $m_s n_s \nu_{ss'} = m_{s'} n_{s'} \nu_{s's}$ . The electric current density for a multi-species plasma is defined as

$$\mathbf{J} = \sum_s q_s n_s \mathbf{u}_s \quad (1.4)$$

The equations of motion for a fully ionized hydrogen plasma, made of protons of particle mass  $m_p$  and electrons of negligible mass (since  $m_e \ll m_p$ ) are given by [16]

$$m_p n \frac{d\mathbf{u}}{dt} = en(\mathbf{E} + \frac{1}{c} \mathbf{u} \times \mathbf{b}) - \nabla p_p + \nabla \cdot \boldsymbol{\sigma} + R \quad (1.5)$$

$$0 = -en(\mathbf{E} + \frac{1}{c} \mathbf{u}_e \times \mathbf{b}) - \nabla p_e - R \quad (1.6)$$

where  $\mathbf{u}, \mathbf{u}_e$  are the ion and electron flow velocities. The viscous stress tensor for electrons has been neglected, since it is proportional to the particle mass. The friction force between both species can be written as

$$R = -m_p n \nu_{pe} (\mathbf{u} - \mathbf{u}_e) \quad (1.7)$$

For the fully ionized hydrogen case, the electric current density (see equation (1.4)) reduces to  $\mathbf{J} = en(\mathbf{u} - \mathbf{u}_e)$ . Therefore, the friction force  $R$  can be expressed as

$$R = -\frac{m_p \nu_{pe}}{e} \mathbf{J} \quad (1.8)$$

The electron and ion pressures  $p_e, p_p$  are assumed to satisfy polytropic laws

$$p_p \propto n^\gamma \quad (1.9)$$

$$p_e \propto n^\gamma \quad (1.10)$$

where the particle densities for both species are assumed to be equal because of charge neutrality (i.e.  $n_p = n_e = n$ ). The bulk flow in this two-fluid description is given by the ion flow  $\mathbf{u}$ , which satisfies

$$\partial_t n + \nabla \cdot (n\mathbf{u}) = 0 \quad (1.11)$$

The electric current density relates with the magnetic field through Ampere's law

$$\mathbf{J} = \frac{c}{4\pi} \nabla \times \mathbf{b} = en(\mathbf{u} - \mathbf{u}_e) \quad (1.12)$$

## 1. The background

---

By adding equations (1.5)-(1.6) and adopting a Newtonian prescription for the viscous stress tensor (i.e.  $\sigma_{ij} = \mu(\partial_i U_j + \partial_j U_i + 2/3\delta_{ij}\nabla \cdot \mathbf{u})$ ,  $\mu$ : viscosity) we obtain

$$m_p n \frac{d\mathbf{u}}{dt} = \frac{1}{c} \mathbf{J} \times \mathbf{b} - \nabla p + \mu \nabla^2 \mathbf{u} + \frac{\mu}{3} \nabla(\nabla \cdot \mathbf{u}) \quad (1.13)$$

where  $p = p_p + p_e$ . On the other hand, after replacing  $\mathbf{u}_e = \mathbf{u} - \mathbf{J}/en$  and equation (1.8) into equation (1.6), we obtain the so-called ‘‘generalized Ohm’s law’’

$$\mathbf{E} + \frac{1}{c} \mathbf{u} \times \mathbf{b} = \frac{1}{nec} \mathbf{J} \times \mathbf{b} - \frac{1}{ne} \nabla p_e + \frac{m_p \nu_{pe}}{e^2 n} \mathbf{J} \quad (1.14)$$

which also expresses the force balance satisfied by the massless electrons. In the last term, we can recognize  $e^2 n / (m_p \nu_{pe})$  as the electric conductivity of a fully ionized hydrogen plasma. The electric and magnetic fields can be cast in terms of the electrostatic potential  $\phi$  and the vector potential  $\mathbf{A}$  ( $\mathbf{E} = -\partial_t \mathbf{A} - \nabla^2 \phi$ ,  $\mathbf{b} = \nabla \times \mathbf{A}$ ). In particular, the curl of equation (1.14) yields the induction equation

$$\partial_t \mathbf{b} = \nabla \times \left[ \left( \mathbf{u} - \frac{1}{en} \mathbf{J} \right) \times \mathbf{b} \right] - \nabla \times (\eta \nabla \times \mathbf{b}) \quad (1.15)$$

where

$$\eta = \frac{m c^2 \nu_{pe}}{4\pi e^2 n} \quad (1.16)$$

is the electric resistivity. Equations (1.13)-(1.15) provide the two-fluid description of magneto-hydrodynamics. The set of equations is completed by the continuity equation (equation (1.11)), the adiabatic conditions given by equations (1.9)-(1.10) and Ampere’s law (equation (1.12)).

We now turn to a dimensionless version of the preceding set of equations using a typical longitudinal length scale  $L_0$ , an ambient density  $n = n_0$ , a typical value for the magnetic field  $B_0$ , a typical velocity equal to the Alfvén speed  $v_A = B_0 / \sqrt{4\pi m_p n_0}$ , and a reference pressure  $p_0$ . The equation of motion becomes

$$n \frac{d\mathbf{u}}{dt} = (\nabla \times \mathbf{b}) \times \mathbf{b} - \beta \nabla p + \frac{1}{R} (\nabla^2 \mathbf{u} + \frac{1}{3} \nabla(\nabla \cdot \mathbf{u})) \quad (1.17)$$

while the induction equation can be written as

$$\partial_t \mathbf{b} = \nabla \times \left[ \left( \mathbf{u} - \frac{c}{n} \nabla \times \mathbf{b} \right) \times \mathbf{b} \right] + \frac{1}{Rm} \nabla^2 \mathbf{b} \quad (1.18)$$

The various dimensionless coefficients in these equations measure the relative importance of different competing physical effects. The plasma ‘‘beta’’

$$\beta = \frac{p_0}{m_p n_0 v_A^2} \quad (1.19)$$

is the approximate ratio of gas to magnetic pressure, while the kinetic ( $R = v_A L_0 / (\mu / m_p n_0)$ ) and magnetic ( $Rm = v_A L_0 / \eta$ ) Reynolds numbers express the ratio of convective to dissipative

effects in each equation. The Hall parameter

$$\epsilon = \frac{c}{\omega_{pi} L_0} = \sqrt{\frac{m_p c^2}{4\pi e^2 n_0 L_0^2}} \quad (1.20)$$

expresses the relative importance of the Hall effect. For  $\epsilon \rightarrow 0$ , the induction equation (1.18) reduces to the one for one-fluid magnetohydrodynamics (MHD).

Equations (1.17)-(1.18) are also known as the Hall-MHD (HMHD) equations. The HMHD system has been extensively studied in recent years, both analytically and numerically. For instance, Hall-MHD has been applied to advance our understanding of dynamo mechanisms [17], magnetic reconnection [18, 19, 20], accretion disk [21, 22] or the physics of turbulent regimes [23, 24, 25, 26]. Potential limitations in the validity of Hall-MHD from the more comprehensive framework of Vlasov-Maxwell kinetic theory have been recently pointed out by [27] and also by [28]. In particular, [27] shows that Hall-MHD is a valid limit of kinetic theory whenever the electron temperature is larger than the ion temperature.

## 1.1.2 Hall-MHD in a strong magnetic field: RHMHD

### 1.1.2.1 RHMHD

In the presence of a strong external magnetic field, velocity and magnetic field fluctuations tend to develop fine scale spatial structures across it, while parallel gradients remain comparatively smoother [29, 30, 31, 32]. Assuming the external field to point along  $\hat{e}_z$  and its magnitude is  $B_0$ , the total (dimensionless) magnetic field is

$$\mathbf{B} = B_0 \hat{e}_z + \mathbf{b}, \quad \left| \frac{\mathbf{b}}{B_0} \right| \approx \alpha \ll 1 \quad (1.21)$$

where  $\alpha = L_\perp / L_\parallel$  represents the typical tilt of magnetic field lines with respect to the  $\hat{e}_z$ -direction. Therefore, one expects (assuming  $L_0 = L_\perp$  to be the typical lengthscale of the problem) that  $\partial_z / \nabla_\perp \approx \alpha \ll 1$  ( $\nabla_\perp \approx 1/L_\perp$ ,  $\partial_z / \approx 1/L_\parallel$ ). In particular if we normalize using the typical scale  $L_\perp = L_0$

$$\nabla_\perp \approx 1, \quad \partial_z \approx \alpha \ll 1 \quad (1.22)$$

To guarantee that the vector fields  $\mathbf{b}$  and  $\mathbf{u}$  remain solenoidal (incompressible flow), we decompose them as

$$\mathbf{B} = B_0 \hat{e}_z + \nabla \times (a \hat{e}_z + g \hat{e}_x) \quad (1.23)$$

and

$$\mathbf{u} = \nabla \times (\varphi \hat{e}_z + f \hat{e}_x) \quad (1.24)$$

## 1. The background

---

where the potentials  $a(\mathbf{r}, t)$ ,  $g(\mathbf{r}, t)$ ,  $\varphi(\mathbf{r}, t)$  and  $f(\mathbf{r}, t)$  are all assumed of order  $\alpha \ll 1$  (see details in [12]).

The standard RMHD approximation [2] only considers the potentials  $a$  and  $\varphi$ , which restrict the dynamics to velocity and magnetic field components perpendicular to the external magnetic field. When the Hall effect becomes relevant (i.e. the term proportional to  $\epsilon$  in equation (1.18)), potentials  $f$  and  $g$  should be added to allow nonzero dynamical field components along  $\hat{\mathbf{e}}_z$  and therefore capture the helical behavior introduced by this effect.

Assuming also  $\partial_t \approx 1$  (which corresponds to the fast timescale  $L_\perp/v_A$ ), we obtain, to first order in  $\alpha$  in equations (1.17)-(1.18)

$$b + \beta p = \text{constant} \quad (1.25)$$

$$\phi + \varphi - \epsilon(b + \beta_e p_e) = \text{constant} \quad (1.26)$$

which are Bernoulli conditions constraining the pressures and the electrostatic potential, and correspond to pressure equilibria established over typical timescales of the fast magnetosonic mode. The coefficient  $\beta_e$  in Equation (1.26) is  $\beta_e = p_{0e}/m_p n_0 v_A^2$ .

To follow the evolution of the system on the much slower timescale  $L_\parallel/v_A$  (i.e. assuming  $\partial_t \approx \alpha \ll 1$ ), eqs. (1.17)-(1.18) to order  $\alpha^2$  describe the dynamical evolution of the potentials (i.e.  $a$ ,  $\varphi$ ,  $g$  and  $f$ )

$$\partial_t a = B_0 \partial_z (\varphi - \epsilon b) + [\varphi - \epsilon b, a] + \frac{1}{Rm} \nabla^2 a \quad (1.27)$$

$$\partial_t \omega = B_0 \partial_z j + [\varphi, \omega] - [a, j] + \frac{1}{Re} \nabla^2 \omega \quad (1.28)$$

$$\partial_t b = B_0 \partial_z (u - \epsilon j) + [\varphi, b] + [u - \epsilon j, a] + \frac{1}{Rm} \nabla^2 b \quad (1.29)$$

$$\partial_t u = B_0 \partial_z b + [\varphi, u] - [a, b] + \frac{1}{Re} \nabla^2 u \quad (1.30)$$

where  $j = -\nabla_\perp^2 a$  and  $\omega = -\nabla_\perp^2 \varphi$  are, respectively, the parallel current and vorticity components, and  $[a, b] = \partial_x a \partial_y b - \partial_y a \partial_x b$  indicate the standard Poisson brackets. The parallel component of the dynamical magnetic field is  $b = -\partial_y g$ , and that of the velocity field is  $u = -\partial_y f$ .

In summary, the set of equations (1.27)-(1.30) describe the dynamical evolution of a Hall plasma embedded in a strong external magnetic field.

Just as for three-dimensional Hall-MHD, this set of equations display three ideal invariants: the energy

$$E = \frac{1}{2} \int d^3 r (|\mathbf{u}|^2 + |\mathbf{b}|^2) = \frac{1}{2} \int d^3 r (|\nabla_\perp \varphi|^2 + |\nabla_\perp a|^2 + u^2 + b^2), \quad (1.31)$$

the magnetic helicity

$$H_m = \frac{1}{2} \int d^3 r (\mathbf{A} \cdot \mathbf{b}) = \int d^3 r a b, \quad (1.32)$$

and the hybrid helicity [33, 34]

$$H_h = \frac{1}{2} \int d^3r (\mathbf{A} + \epsilon \mathbf{u}) \cdot (\mathbf{b} + \epsilon \mathbf{\Omega}) = \int d^3r [ab + \epsilon(a\omega + ub) + \epsilon^2 u\omega] \quad (1.33)$$

where  $\mathbf{\Omega} = \nabla \times \mathbf{u}$  is the vorticity vector field.

### 1.1.2.2 Weak compressible RHMHD

In a similar fashion, a weakly compressible model can be obtained as well. To this end, a slight modification must be introduced to the hypothesis recently described [35]. The velocity field, in the more general case, can be decomposed as a superposition of a solenoidal part (incompressible flow) plus the gradient of a scalar field (irrotational flow), i.e.

$$\mathbf{u} = \nabla \times (\varphi \hat{\mathbf{e}}_z + f \hat{\mathbf{e}}_x) + \nabla \psi, \quad (1.34)$$

Using the same assumptions as in 1.1.2.1, but in addition assuming that  $\psi(\mathbf{r}, t)$  is of order  $\alpha^2$  the weak compressible RHMHD equations can be obtained

$$\partial_t a = B_0 \partial_z (\varphi - \epsilon b) + [\varphi - \epsilon b, a] + \frac{1}{Rm} \nabla^2 a \quad (1.35)$$

$$\partial_t \omega = B_0 \partial_z j + [\varphi, \omega] - [a, j] + \frac{1}{Re} \nabla^2 \omega \quad (1.36)$$

$$\partial_t b = B_0 \beta_p \partial_z (u - \epsilon j) + [\varphi, b] + \beta_p [u - \epsilon j, a] + \beta_p \frac{1}{Rm} \nabla^2 b \quad (1.37)$$

$$\partial_t u = B_0 \partial_z b + [\varphi, u] - [a, b] + \frac{1}{Re} \nabla^2 u \quad (1.38)$$

The only difference between the weakly compressible RHMHD and the original RHMHD is in equation (1.37). In the original RHMHD equations  $\beta_p = 1$ , whereas here  $\beta_p = \beta\gamma/(1 + \beta\gamma)$ , with the plasma  $\beta = 4\pi p/B_0^2$ . Therefore the compressibility effect here depends on the external magnetic field which embeds the plasma. Note that the entire flow compressibility is introduced through this parameter, which is a constant of the model. Therefore the computational cost is exactly the same as in the original RHMHD model. Just as in RHMHD the bernoulli equations and the invariants are still valid.

In general we will refer to this model simply as RHMHD, and in our studies (except in section A) we will use this system of equations.

## 1. The background

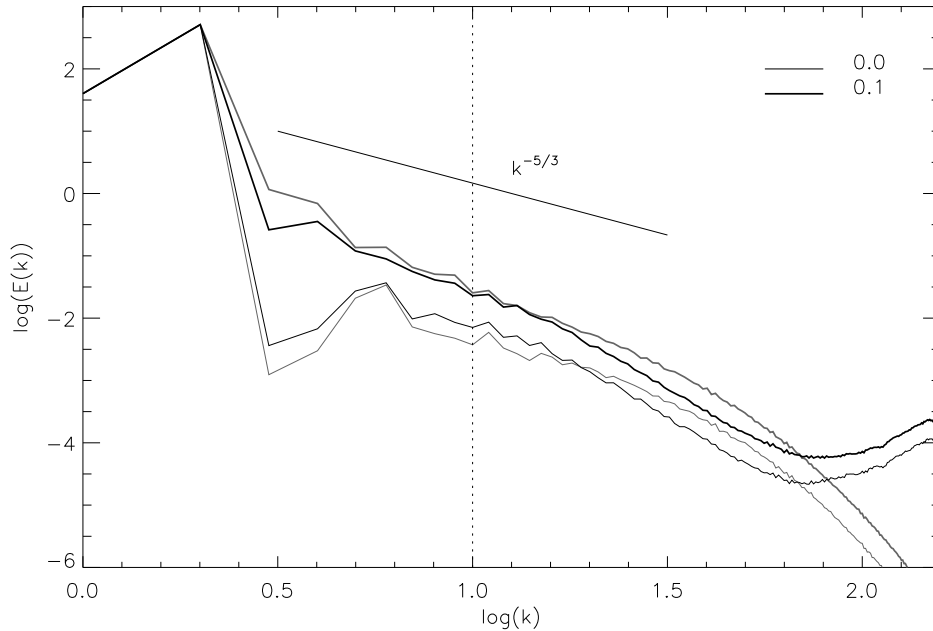


Figure 1.1: Energy power spectra for  $\epsilon = 0.0$  (thick gray trace) and  $\epsilon = 0.1$  (thick black trace) for a  $512 \times 512 \times 32$  run at  $t = 20$ . The Kolmogorov slope is displayed for reference, and the vertical dashed line indicates the location of  $k_\epsilon = 1/\epsilon$  for  $\epsilon = 0.1$ . The thin lines show the power spectra for the corresponding kinetic energies.

## 1.2 Applications

### 1.2.1 Application of RHMHD to solar wind turbulence

The relative importance of the Hall effect in the Hall-MHD equations (i.e. equations (1.17)-(1.18)) is determined by the coefficient  $\epsilon$ , which is only present in equation (1.18). From the expression of  $\epsilon$  in equation (1.20), we find that the Hall effect must become non-negligible in sufficiently low density plasmas. One of the many low-density astrophysical plasmas for which the Hall effect is known to be relevant is the solar wind, and it becomes progressively more important as we move away from the Sun. Also, the solar wind plasma is permeated by an external magnetic field (although the magnetic fluctuations can be a non-negligible fraction of the external field).

To study the role of the Hall effect on the energy power spectrum, we integrate equations (1.35)-(1.38) numerically. We assume periodic boundary conditions, and specify the velocity fields at the boundaries  $z = 0$  and  $z = L$  (for a detailed description, see [10]). These boundary motions pump energy into the system and drives it into a turbulent regime. We use a pseudo-spectral technique with dealiasing for the perpendicular spatial derivatives and finite

differences for the (much smoother)  $\hat{e}_z$ -derivatives. We start all our simulations with trivial initial conditions (i.e.  $a = \varphi = u = b = 0$ ).

We performed a set of simulations with different values of the Hall parameter (see details in [12]). Among the results arising from these simulations, we find that the fraction of kinetic to total energy increases monotonically with the Hall coefficient  $\epsilon$ .

In the MHD limit ( $\epsilon = 0$ ), the total energy reduces to (Eq.(1.31))

$$E_{perp} = \frac{1}{2} \int d^3r (|\nabla_{\perp}\varphi|^2 + |\nabla_{\perp}a|^2) \quad (1.39)$$

while for the general case ( $\epsilon \neq 0$ ) there is a fraction of the total energy directly associated to the parallel degrees of freedom

$$E_{par} = \frac{1}{2} \int d^3r (u^2 + b^2) \quad (1.40)$$

The fraction  $E_{par}/E_{tot}$  is also observed to increase monotonically with  $\epsilon$ , even though we are not pumping parallel energy from the boundaries. Parallel fluctuations are generated by the perpendicular part of the dynamics (i.e. by  $a$  and  $\varphi$ ) via terms proportional to  $\epsilon$  in equation (1.37).

We expect the Hall current to affect the dynamics of spatial patterns whose sizes are of the order of the ion skin depth (i.e.  $c/w_{pi}$ ) or smaller. According to Equation (1.20), this typical size corresponds to a  $k_{\epsilon} = 1/\epsilon$ . In Figure 1.1 we compare the spectral distributions of energy for  $\epsilon = 0.0$  and  $\epsilon = 0.1$ , once a stationary turbulent regime is reached for each of these simulations. Even though these numerical simulations have only a moderate spatial resolution of  $512 \times 512 \times 32$ , the energy spectra are consistent with the slope predicted by Kolmogorov (i.e.  $E_k \propto k^{-5/3}$ ) at intermediate and large scales (i.e. intermediate and small values of  $k$ ). We also find that both the total and kinetic energy spectra for the simulation corresponding to  $\epsilon = 0.1$ , strongly depart from the purely MHD run (i.e.  $\epsilon = 0.0$ ) for  $k \geq k_{\epsilon}$ .

The spectral distribution of energy dissipation is given by  $2\eta k^2 E(k)$ . Figure 1.2 shows energy dissipation spectra for different simulations corresponding to  $\epsilon = 0, 1/32, 1/16, 1/8$ . We find that the spectral distribution of energy dissipation shifts to larger wavelengths as  $\epsilon$  rises, which is quantitatively confirmed by the corresponding values of the mean scale defined as

$$k_{mean}^2 = \frac{\int dk k^2 E(k)}{\int dk E(k)} \quad (1.41)$$

listed in the Table.

The scale  $k_{mean}$ , also known as the Taylor scale, can be regarded as the average curvature of magnetic fieldlines. Its gradual shift with the Hall effect is consistent with a reduction of the energy transfer rate associated to the direct energy cascade for  $k > k_{\epsilon}$ , which in turn leads to smaller total dissipation rates ([36], see also [37]).

## 1. The background

---

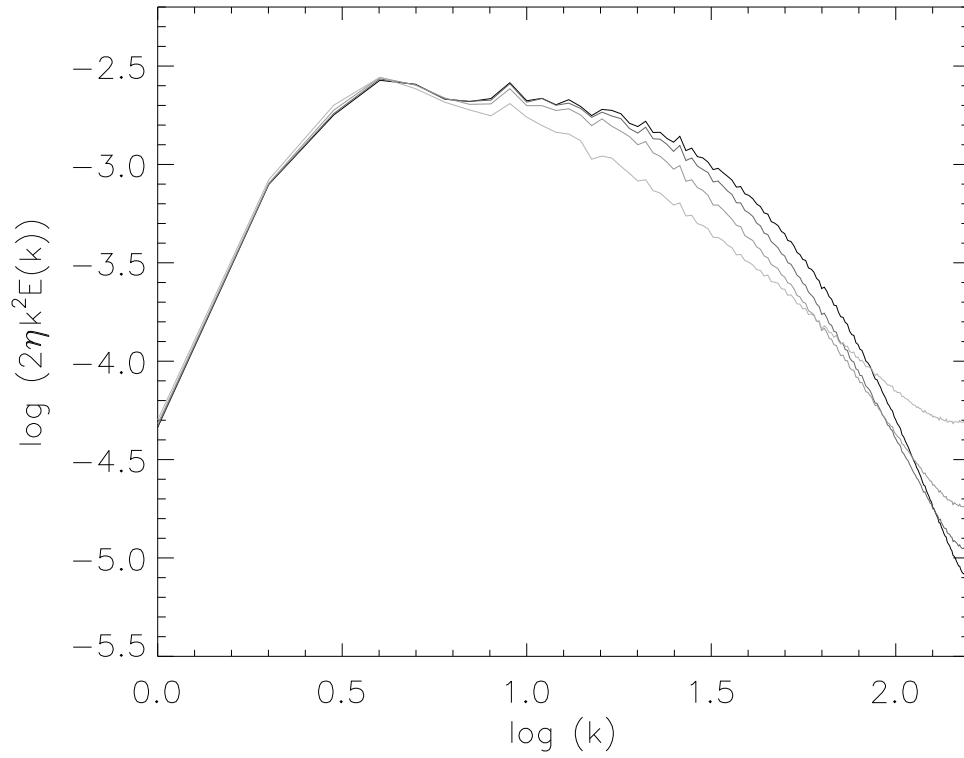


Figure 1.2: Spectral distribution of energy dissipation for simulations corresponding to  $\epsilon = 0, 1/32, 1/16, 1/8$ , displayed in gradually lighter shades of gray.

Table 1.1: Hall and mean scales

Run	$\epsilon$	$k_{Hall}$	$k_{mean}$
1	0	$\infty$	8.5
2	1/32	32	8.2
3	1/16	16	7.7
4	1/8	8	7.2

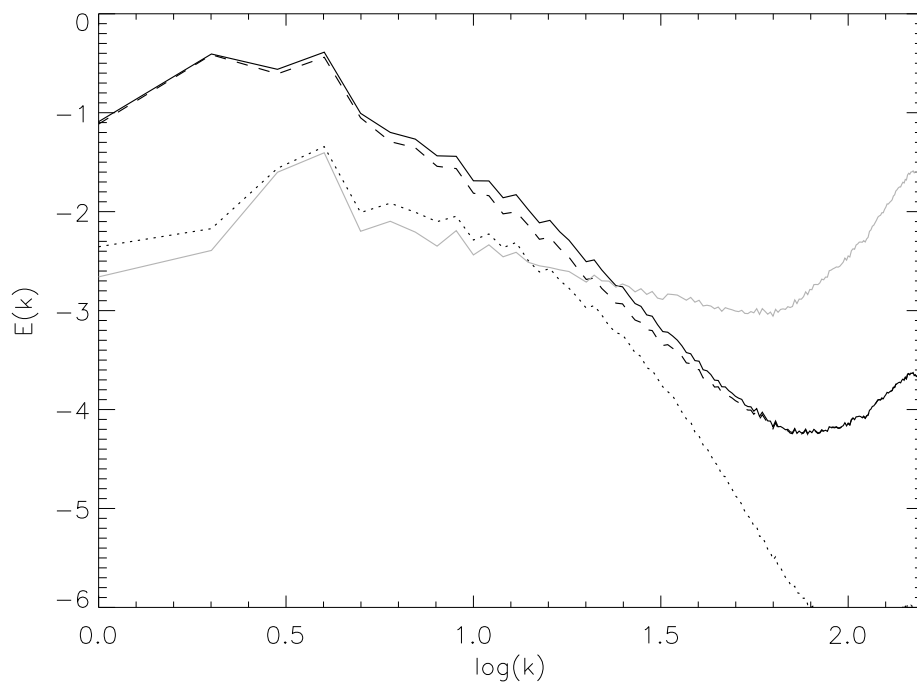


Figure 1.3: Energy power spectra for a  $512 \times 512 \times 32$  run with  $\epsilon = 0.1$  at  $t = 20$ . Black full trace corresponds to total energy, dotted (dot-dashed) trace to kinetic (magnetic) energy, and the gray full trace shows the power spectrum of the electric field.

## 1. The background

---

Another important feature of Hall-MHD in its ideal limit (i.e. for  $\eta \rightarrow 0$ ) is the self-consistent presence of a component of the electric field parallel to the total magnetic field, which is able to accelerate charged particles (see also [38] and [39]). Figure 1.3 shows the power spectrum of the total electric field, superimposed to the corresponding spectra of kinetic and magnetic energy, for  $\epsilon = 0.1$ . We can clearly observe an excess of power in the electric field compared to the magnetic field at large wavenumbers (i.e.  $k > k_\epsilon$ ).

The dimensionless version of the electric field (see Eqn (1.14)) is

$$\mathbf{E} = -\left(\mathbf{u} - \frac{\epsilon}{n} \nabla \times \mathbf{b}\right) \times \mathbf{b} - \frac{\epsilon \beta_e}{n} \nabla p_e + \eta \nabla \times \mathbf{b} \quad (1.42)$$

When computing the component of the electric field which is parallel to the magnetic field (i.e.  $E_{\parallel} = \frac{\mathbf{E} \cdot \mathbf{b}}{|\mathbf{b}|^2}$ ) only two terms contribute, the one proportional to the electron pressure gradient and the one corresponding to electric resistivity. To second order in the expansion coefficient  $\alpha$  (see Eqn (1.21)) and using that  $\beta_e p_e = -\frac{\beta_e}{\beta} b$ , we obtain

$$E_{\parallel} = \epsilon \frac{T_e}{T_e + T_p} (\partial_z b + [b, a]) + \eta j \quad (1.43)$$

In Figure 1.4 we show two histograms corresponding to the terms proportional to  $\epsilon$  (black) and  $\eta$  (gray) in Equation (1.43), assuming  $T_e \gg T_p$ . We can clearly see that the contribution of the Hall effect to  $E_{\parallel}$ , which is actually caused by the  $\nabla_{\parallel} p_e$  term in Equation (1.42), is markedly larger than the contribution of the plasma resistivity. Note that the electron pressure is cast in terms of the parallel magnetic field component  $b$  as a result of Equation (1.25).

We need simulations at much higher spatial resolution to make quantitative assessments about power spectra or energy dissipation, but these simulations at moderate resolution show that the behavior at small scales (i.e.  $k > k_\epsilon$ ) is clearly affected by the presence of the Hall term. The RHMHD framework has been numerically tested against the more general compressible Hall-MHD description [14]. The results show that the degree of agreement between both sets of simulations is very high when the various assumptions for RHMHD are satisfied, thus rendering RHMHD as a valid approximation of Hall-MHD in the presence of strong external magnetic fields.

### 1.2.2 Application of RMHD to coronal heating

Another application of the reduced approximation to an astrophysical problem, is the simulation of magnetic loops of the solar corona, to study the heating of the plasma confined in coronal magnetic structures. To model the internal dynamics of coronal loops in solar (or stellar) active regions, we assume these loops to be relatively homogeneous bundles of fieldlines, with their footpoints deeply rooted into the photosphere. Individual fieldlines are moved around by

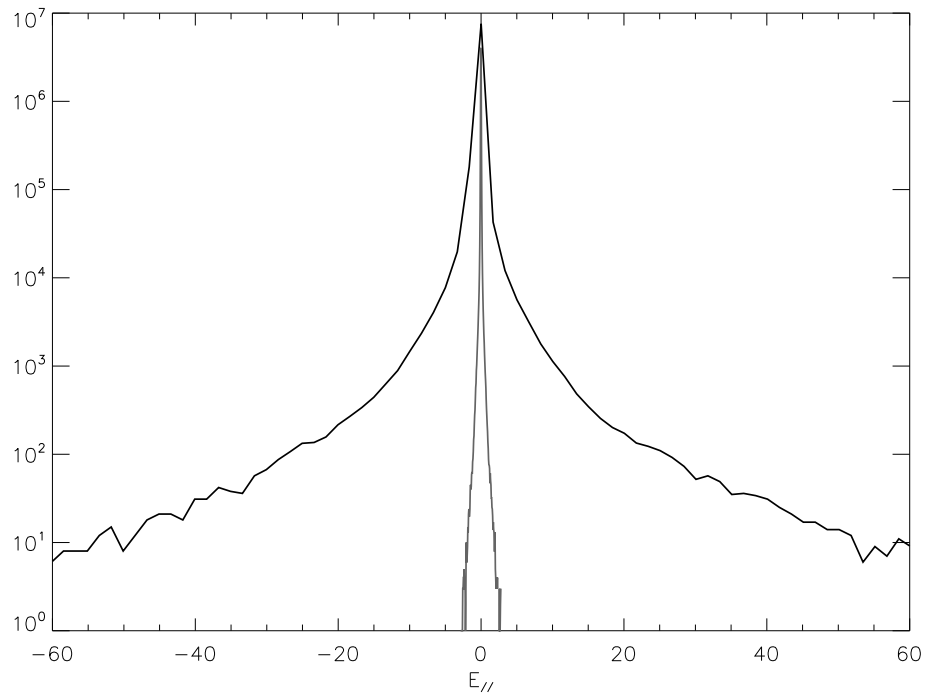


Figure 1.4: Histograms of the terms proportional to  $\epsilon$  (black) and  $\eta$  (gray) for  $E_{\parallel}$  (see Eqn (1.43)) for a  $512 \times 512 \times 32$  run with  $\epsilon = 0.1$  and  $t = 20$ .

## 1. The background

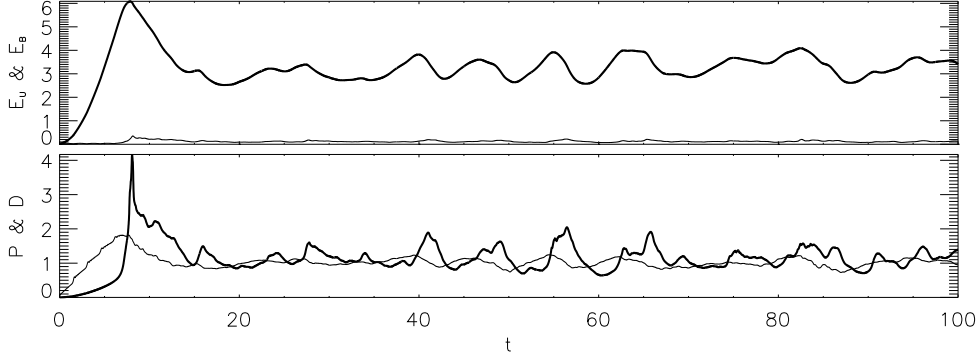


Figure 1.5: Energy and dissipation rate time series. **Upper panel:** Kinetic energy (thin), and total energy (thick). **Lower panel:** Energy dissipation rate (thick) and Poynting flux (thin).

subphotospheric convective motions, which in turn generate magnetic stresses in the coronal portion of the loop. We therefore consider a magnetic loop with length  $L$  and cross section  $2\pi l_{ph} \times 2\pi l_{ph}$ , where  $l_{ph}$  is the lengthscale of typical subphotospheric motions. For elongated loops, *i.e.* such that  $2\pi l_{ph} \ll L$ , we neglect toroidal effects. The main magnetic field  $\mathbf{B}_0$  is assumed to be uniform and parallel to the axis of the loop (the  $z$  axis) and the perpendicular planes at  $z = 0$  and  $z = L$  correspond to the photospheric footpoints. For the coronal plasma, the Hall effect is actually negligible, so we simply integrate the RMHD equations (*i.e.*  $\epsilon = 0.000$ ).

As boundary conditions, we assume  $\psi(z = 0) = 0$  and  $\psi(z = L) = \Psi(x, y)$  where the stream function  $\Psi(x, y)$  describes stationary and incompressible footpoint motions on the photospheric plane (see [10]). We specify the Fourier components of  $\Psi(x, y)$  as  $\Psi_{\mathbf{k}} = \Psi_0$  inside the ring  $3 < l_{ph}|k| < 4$  on the Fourier plane, and  $\Psi_{\mathbf{k}} = 0$  elsewhere, to simulate a stationary and isotropic pattern of photospheric granular motions of diameters between  $2\pi l_{ph}/4$  and  $2\pi l_{ph}/3$ . The strength  $\Psi_0$  is proportional to a typical photospheric velocity  $V_{ph} \approx 1 \text{ km.s}^{-1}$ . The typical timescale associated to these driving motions, is the eddy turnover time, which is defined as  $t_{ph} = l_{ph}/V_{ph} \approx 10^3 \text{ sec}$ . We choose a narrowband and non-random forcing to make sure that the broadband energy spectra and the signatures of intermittency that we obtain are exclusively determined by the nonlinear nature of the MHD equations.

In Figure 1.5 we show the results obtained from a simulation extending from  $t = 0$  to  $t = 100 t_A$ , where  $t_A = L/v_A$  is the Alfvén time of the loop. The upper panel shows the kinetic ( $E_U$ , thin trace) and total energy ( $E = E_U + E_B$ , thick trace). We can see that after about ten Alfvén times, the energy reaches a stationary regime, since the work done by footpoint motions statistically (*i.e.* in time average) reaches an equilibrium with the dissipative processes (electric resistivity and fluid viscosity). In this stationary regime most of the energy is magnetic, while

kinetic energy is only about 5% of the total. In the lower panel, we show the dissipation rate ( $D$ , thick trace) and the incoming Poynting flux ( $P$ , thin trace), showing that their time averages are approximately equal.

The observed stationary equilibrium has been shown to correspond to a turbulent regime [40, 8], and therefore the associated energy cascade bridges the gap between the large spatial scales where energy is injected by footpoint motions, to the much smaller scales where it dissipates (see [41]). The dependence of the stationary dissipation rate  $\langle D \rangle = \langle P \rangle$  ( $\langle \dots \rangle$ : time average) with the physical parameters of the loop is ([9])

$$\langle D \rangle \propto \frac{\rho l_{ph}^2}{t_A^3} \left( \frac{t_A}{t_{ph}} \right)^{\frac{3}{2}} \quad (1.44)$$

In Figure 1.5 we can clearly observe the spiky nature of these time series, which is the result of the intermittency arising in turbulent regimes. These spikes of energy dissipation can be associated with Parker's *nanoflares* (see [42, 43]) and the statistical distribution of these dissipation events can be obtained. A detailed description of that statistical study is beyond the scope of this presentation, but the main result (see also [44]) is that the number of nanoflares (or spikes) as a function of their energies  $N(E)$  follows a power law  $N(E) \approx E^{-3/2}$ , which is remarkably comparable to the result obtained for larger dissipation events. The statistics of large energy dissipation events such as microflares and flares, has been reported by [45], gathering a large number of observational studies.

## 1.3 Numerical simulations

In this section we introduce the version of the equation systems that were used to carry out the respective numerical simulations. Also we give the characteristics of the codes used to carrying them out.

### 1.3.1 Equations

The dimensionless version of compressible Hall MHD equations that are considered to write the code are

$$\begin{aligned} \partial_t \mathbf{u} = \mathbf{u} \times \boldsymbol{\omega} + \frac{1}{M_A^2} \frac{\mathbf{J} \times \mathbf{b}}{\rho} - \nabla \left( \frac{\mathbf{u}^2}{2} + \frac{\rho^{\gamma-1}}{M_S^2(\gamma-1)} \right) \\ + \nu \left( \frac{\nabla^2 \mathbf{u}}{\rho} + \frac{1}{3} \frac{\nabla(\nabla \cdot \mathbf{u})}{\rho} \right), \end{aligned} \quad (1.45)$$

$$\partial_t \rho = -\nabla \cdot (\rho \mathbf{u}), \quad (1.46)$$

## 1. The background

---

$$\partial_t \mathbf{A} = \mathbf{u} \times \mathbf{b} - \epsilon \frac{\mathbf{J} \times \mathbf{b}}{\rho} - \nabla \phi + \eta \nabla^2 \mathbf{A}, \quad (1.47)$$

$$\nabla \cdot \mathbf{A} = 0 \quad (1.48)$$

In these equations,  $\mathbf{u}$  is the velocity field,  $\boldsymbol{\omega}$  is the vorticity field,  $\mathbf{J}$  is the current,  $\mathbf{b}$  is the magnetic field,  $\rho$  is the density of the plasma, and  $\mathbf{A}$  and  $\phi$  are respectively the magnetic and electric potentials. A barotropic law is assumed for the plasma, with the pressure given by  $p = C\rho^\gamma$ , where  $C$  is a constant and  $\gamma = 5/3$ . Equation (1.48) is the Coulomb gauge, which acts as a constraint that fixes the electric potential in Eq. (1.47). Control parameters of the system are the sonic Mach number  $M_S$ , the Alfvén Mach number  $M_A$ , the viscosity  $\nu$  and, and the resistivity  $\eta$ . All these numbers are control parameters in the numerical simulations. In our study, the most important control parameter is the Hall coefficient  $\epsilon = \rho_{ii}/L$ , where  $\rho_{ii}$  is the ion skin depth and  $L$  is the characteristic scale of turbulence. When  $\epsilon = 0$ , the equations above result in the well known compressible MHD equations. We refer to this set of equations as the CMHD equations (Hall compressible MHD).

The other system that we will use are the RHMHD equations. The version used to make the corresponding code is

$$\partial_t \boldsymbol{\omega} = B_0 \partial_z j + [j, a] - [\boldsymbol{\omega}, \boldsymbol{\varphi}] + \nu \nabla^2 \boldsymbol{\omega}, \quad (1.49)$$

$$\partial_t a = B_0 \partial_z (\boldsymbol{\varphi} - \epsilon b) + [\boldsymbol{\varphi}, a] + [b, a] + \eta \nabla^2 a, \quad (1.50)$$

$$\begin{aligned} \partial_t b = B_0 \beta_p \partial_z (u - \epsilon j) + [\boldsymbol{\varphi}, b] + \beta_p [u, a] + \\ - \epsilon \beta_p [j, a] + \beta_p \eta \nabla^2 b, \end{aligned} \quad (1.51)$$

$$\partial_t u = B_0 \partial_z b + [\boldsymbol{\varphi}, u] - [a, b] + \nu \nabla^2 u, \quad (1.52)$$

where

$$\boldsymbol{\omega} = -\nabla_{\perp}^2 \boldsymbol{\varphi}, \quad (1.53)$$

$$j = -\nabla_{\perp}^2 a, \quad (1.54)$$

$$b = -\partial_y g, \quad (1.55)$$

$$u = -\partial_y f, \quad (1.56)$$

and the notation  $[A, B] = \partial_x A \partial_y B - \partial_x B \partial_y A$  is employed for the Poisson bracket. The potential  $\psi$  was eliminated from these equations using the equation for the pressure. Finally,  $\beta_p = \beta\gamma/(1 + \beta\gamma)$  is a function of the plasma “beta” ( $\beta = 4\pi p/B_0^2$ ). As in the previous set of equations, these equations become the compressible RMHD equations when  $\epsilon = 0$ . This model will be tested in the next chapter through a direct comparison with the CMHD equations and use it for the rest of the thesis to study how the Hall effect modifies the dynamics of magnetohydrodynamic turbulence under a strong magnetic field.

#### 1.3.2 Numerical codes

We use a standard parallel pseudospectral code to evaluate the nonlinear terms and solve numerically the equations [46]. A second-order Runge-Kutta time integration scheme is used. Periodic boundary conditions are assumed in all directions of a cube of side  $2\pi L$  (where  $L \sim 1$  is the initial correlation length of the fluctuations, defined as the length unit). The runs performed throughout in this study do not contain any magnetic or velocity external stirring terms, so the RHMHD system is let to evolve freely.

In the next chapter we will specify the initial conditions. In general terms, we excite initially Fourier modes (for both magnetic and velocity field fluctuations) in a shell in  $k$ -space, with the same amplitude for all modes and random phases. The runs are freely evolved until the turbulence is fully developed. Time units (the initial eddy turnover time) is defined in terms of the initial rms velocity fluctuation and unit length.

The kinetic and magnetic Reynolds numbers are defined respectively as  $R = 1/\nu$ ,  $R_m = 1/\eta$ , based on unit initial r.m.s. velocity fluctuation, unit length, and dimensionless values for the viscosity and diffusivity.

The control parameters will be specified in each section.



# Bibliography

- [1] Daniel Gómez, **Luis N. Martín**, Pablo Dmitruk, *Advances in Space Research*, **51**, 1916, (2013) [9](#)
- [2] H. Phys. Fluids, **19**, 134, (1976). [9](#), [14](#)
- [3] D.C. Montgomery, *Phys. Scr.*, T2/1, 83, (1982). [9](#)
- [4] A.A. van Ballegooijen, *Astrophys. J.*, **311**, 1001, (1986). [10](#)
- [5] D.W. Longcope, R.N. Sudan, *Astrophys. J.*, **437**, 491, 1994. [10](#)
- [6] D.L. Hendrix, G. Van Hoven, *Astrophys. J.*, **467**, 887, 1996. [10](#)
- [7] L. Milano, P. Dmitruk, C.H. Mandrini, D.O. Gómez, P. Demoulin, *Astrophys. J.*, **521**, 889, (1999). [10](#)
- [8] D.O. Gómez, C. Ferro Fontán, C., *Astrophys. J.* **394**, 662 (1992). [10](#), [23](#)
- [9] P. Dmitruk, D.O. Gómez, *Astrophys. J.* **527**, L63 (1999). [10](#), [23](#)
- [10] P. Dmitruk, D.O. Gómez, W.H. Matthaeus, *Phys. Plasmas* **10**, 3584 (2003). [10](#), [16](#), [22](#)
- [11] P. Dmitruk, W.H. Matthaeus, S. Oughton, *Phys. Plasmas* **12**, 112304 (2005). [10](#)
- [12] D. O. Gómez, S. M. Mahajan, and P. Dmitruk, *Phys. Plasma* **15**, 102303 (2008). [10](#), [14](#), [17](#)
- [13] N.H. Bian, D. Tsiklauri, *Phys. Plasmas* **16**, 064503 (2009). [10](#)
- [14] L.N. Martín, P. Dmitruk, D.O. Gómez, *Phys. Plasma* **17**, 112304, 2010. [10](#), [20](#)
- [15] M.J. Aschwanden, *Introduction to Plasma Physics*, IOP Publ. (Bristol & Philadelphia), 1995. [10](#)

## BIBLIOGRAPHY

---

- [16] N.A. Krall, A.W. Trivelpiece, Principles of Plasma Physics (McGraw-Hill, New York, 1973), p. 89. [11](#)
- [17] P.D. Mininni, D.O. Gómez, S.M. Mahajan, *Astrophys. J.*, **584**, 1120, (2003). [13](#)
- [18] F. Mozer, S. Bale, T.D. Phan, *Phys. Rev. Lett.*, **89**, 015002, (2002). [13](#)
- [19] D. Smith, S. Ghosh, P. Dmitruk, W.H. Matthaeus, *Geophys. Res. Lett.*, **31**, 02805, (2004). [13](#)
- [20] L.F. Morales, S. Dasso, D.O. Gómez, *J. Geophys. Res.*, **110**, A04204, (2005). [13](#)
- [21] M. Wardle, *Mon. Not. R.A.S.*, **303**, 239, (1999). [13](#)
- [22] S.A. Balbus, C. Terquem, *Astrophys. J.* **552**, 235 (2001). [13](#)
- [23] W.H. Matthaeus, P. Dmitruk, D. Smith, S. Ghosh, S. O., *Geophys. Res. Lett.*, **30**, 2104, 2003. [13](#)
- [24] P.D. Mininni, D.O. Gómez, S.M. Mahajan, *Astrophys. J.*, **619**, 1019, (2005). [13](#)
- [25] S. Galtier, *J. Plasma Phys.*, **72**, 721, 2006. [13](#)
- [26] P. Dmitruk, W.H. Matthaeus, *Phys. Plasmas* **13**, 042306 (2006). [13](#)
- [27] G.G. Howes, *Nonlin. Proc. Geophys.*, **16**, 219, 2009. [13](#)
- [28] A.A. Schekochihin, S.C. Cowley, W. Dorland, G.W. Hammett, G.G. Howes, E. Quataert, T. Tatsuno, *Astrophys. J. Suppl.*, **182**, 310, (2009). [13](#)
- [29] J.V. Shebalin, W.H. Matthaeus, D. Montgomery, *J. Plasma Phys.*, **29**, 525, (1983). [13](#)
- [30] S. Oughton, E.R. Priest, W.H. Matthaeus, *J. Fluid Mech.*, **280**, 95, (1994). [13](#)
- [31] W.H. Matthaeus, S. Oughton, S. Ghosh, M. Hossain, *Phys. Rev. Lett.*, **81**, 2056, (1998). [13](#)
- [32] S. Oughton, W.H. Matthaeus, S. Ghosh, *Astrophys. J.*, **5**, 4235, (1998). [13](#)
- [33] L. Turner, *IEEE Trans. Plasma Sci.*, **PS14**, 849, (1983). [15](#)
- [34] S.M. Mahajan, Z. Yoshida, *Phys. Plasma* **7**, 635, 2000. [15](#)
- [35] N. H. Bian and D. Tsiklauri, *Phys. Plasma* **16**, 064503 (2009). [15](#)
- [36] D. O. Gómez, P. D. Mininni, and P. Dmitruk, *Phys. Rev. E* **82**, 036406 (2010). [17](#)
- [37] P.D. Mininni, A. Alexakis, A. Pouquet, *J. Plasma Phys.*, **73**, 377, (2007). [17](#)
- [38] N.H. Bian, E.P. Kontar, *Phys. Plasmas* **17**, 062308 (2010). [20](#)

- [39] N.H. Bian, E.P. Kontar, *Astron. Astrophys.* **519**, A114 (2010). [20](#)
- [40] D.O. Gómez, C. Ferro Fontán, *Solar Phys.*, **116**, 33, 1988. [23](#)
- [41] P. Dmitruk, D.O. Gómez, *Astrophys. J.* **484**, L83 (1997). [23](#)
- [42] P. Dmitruk, D.O. Gómez, E. DeLuca, *Astrophys. J.* **505**, 974 (1998). [23](#)
- [43] E.N. Parker, *Astrophys. J.*, **330**, 474-479, (1988). [23](#)
- [44] D.O. Gómez, P. Dmitruk, Turbulent heating of coronal active regions, in "Proc. IAU Symp. 247: Waves and Oscillations in the Solar Atmosphere", (Eds. R. Erdelyi & C.A. Mendoza-Briceño), 269-278, 2008. [23](#)
- [45] M.J. Aschwanden, *Physics of the Solar Corona. An Introduction*, Springer-Verlag (Berlin), 2004. [23](#)
- [46] S. Ghosh, M. Hossain, and W. H. Matthaeus, *Phys. Commun.* **74**, 18 (1993). [25](#)



# Testing the model: Direct comparisons of compressible magnetohydrodynamics and the RHMHD model

[1]

## Contents

---

<b>2.1 Simulations</b> . . . . .	<b>32</b>
2.1.1 Set up . . . . .	32
2.1.2 Initial Conditions . . . . .	32
<b>2.2 Incompressible RHMHD Vs Compressible RHMHD</b> . . . . .	<b>33</b>
<b>2.3 Anisotropic initial conditions</b> . . . . .	<b>37</b>
<b>2.4 Isotropic initial conditions</b> . . . . .	<b>42</b>
<b>2.5 Conclusions</b> . . . . .	<b>46</b>

---

In this chapter we test the RHMHD model. The main advantage of this model lies in the reduction of computational cost. We showed in the first chapter (1.1.2.2) that we can make minor modifications to the model to describe the compressibility effects [2]. We will start studying the improvements obtained by considering compressibility effects (2.2), then we analyze the effect of the initial conditions and of the external magnetic field on the RHMHD solutions (2.3, 2.4).

## 2. Testing the model

---

### 2.1 Simulations

In this chapter we will study the solutions for different types of initial conditions, and perform a direct comparison between the solutions from CMHD model and the RHMHD model. Both equation systems will start from exactly the same initial fluctuation fields (velocity and magnetic field).

#### 2.1.1 Set up

The same resolution is used in both codes in all three directions in most of the runs presented here, which have a moderate resolution of  $128^3$  Fourier modes, allowing many different runs to be done with different initial conditions and/or mean magnetic field.

We considered kinetic and magnetic Reynolds numbers  $R = R_m = 400$  in all of the runs. We also considered a Mach number  $M_S = 1/4$ , Alfvén number  $M_A = 1$ , and Hall coefficient  $\epsilon = 1/16$  in all runs.

Two different values of the magnetic field  $B_0 = 1, 8$  (weak and strong) are considered (in units of the initial rms magnetic fluctuation value).

To study the performance of the RHMHD solutions in contrast with the CMHD solutions, we performed simulations with two different initial conditions, one of them maintains the anisotropy imposed by the external field while the other does not assume any preferential direction.

#### 2.1.2 Initial Conditions

The first set of initial conditions, anisotropic initial condition (A.I.C.), complied with the anisotropy imposed by the external magnetic field. This initial condition was generated using a two-step process. First, a set of Fourier modes for both magnetic and velocity field fluctuations is produced, with amplitudes such that the (omnidirectional) energy spectrum is a Kolmogorov spectrum proportional to  $k^{-5/3}$  for  $1 \leq k \leq 16$  and gaussian random phases. Modes outside this range in k-space are set to 0. Second, an anisotropic filter is applied, so that excited modes for which  $\tau_{nl}(\mathbf{k}) > \tau_A(\mathbf{k})$  are initially set to 0 (Here  $\tau_{nl}(\mathbf{k}) = 1/(kv_k)$  is the non-linear time associated with the speed  $v_k$  at wavenumber  $k$  and  $\tau_A(\mathbf{k}) = 1/(k_{\parallel}V_{A_0})$  is the Alfvén time, where  $V_{A_0} = B_0/\sqrt{4\pi\rho_0}$  is the Alfvén speed). This is to ensure that only modes which satisfy the RHMHD requirement are excited initially [3, 4, 5, 6]. Taking the Kolmogorov inertial range form  $v_k \sim k^{-1/3}$  into account, this condition becomes

$$k_{\parallel} \leq C \frac{k^{2/3}}{V_{A_0}} \quad (2.1)$$

---

## 2.2. Incompressible RHMHD Vs Compressible RHMHD

where  $C$  is a  $O(1)$  constant. Here we view this inequality as one of the conditions for validity of the RMHD approximation. For marginal attainment of the time scale inequality, we consider runs with  $C = 1$ . The condition means that only large parallel wavelength modes (low  $k_{\parallel}$ ) are allowed in the initial fluctuations, and becomes increasingly restrictive as the value of the mean magnetic field (i.e.  $V_{A_0}$ ) is increased.

To complete the specification of the initial conditions, the fluctuations are normalized so that the initial mean square values of the magnetic and velocity field are both equal to 1 (unit value). Cross helicity and magnetic helicity are initialized at very small values (remind that if the normalized cross helicity is unity there is no turbulent dynamics). Only plane-polarized fluctuations are considered in this case, that is, fluctuations are perpendicular to the mean magnetic field, e.g.,  $\mathbf{u}(\mathbf{x}, t = 0) = \mathbf{u}_{\perp}(\mathbf{x}, 0)$ .

The runs performed throughout this paper do not contain any magnetic or velocity stirring terms, so that the CMHD and RHMHD systems evolve freely.

In the second case, isotropic initial condition (I.I.C.), we consider initial Fourier modes in a shell in  $k$ -space  $1 \leq k \leq 2$  at low wavenumbers, with constant amplitudes and random phases. Unlike the previous case, no initial anisotropic filter is applied here, so the initial conditions are spectrally isotropic. As in the anisotropic case, only plane-polarized fluctuations (transverse to the mean magnetic field) are included, so these are (low- to high-frequency) Alfvén mode fluctuations and not magnetosonic modes.

This set of initial conditions represent a more general situation that may arise in an application, where no initial spectral anisotropy is imposed (for instance, they could represent better the effect of isotropic driving). Therefore, in the next chapters we will use this initial conditions to understand the effect of the Hall term

The organization of this section is as follows. Subsection 2.2 provides a brief comparison of the RHMHD model and its compressible version. In subsection 2.3 we present the numerical results for anisotropic initial conditions. Subsection 2.4 shows the numerical results for isotropic initial conditions. Therefore

## 2.2 Incompressible RHMHD Vs Compressible RHMHD

The RHMHD model [7] is a description of the two-fluid plasma dynamics in a strong external magnetic field. The model assumes that the normalized magnetic field is of the form (the external field is along  $\hat{e}_z$ )

$$\mathbf{B} = B_0 \hat{e}_z + \mathbf{b} , \quad \left| \frac{\mathbf{b}}{B_0} \right| \approx \alpha \ll 1, \quad (2.2)$$

where  $\alpha$  represents the typical tilt of magnetic field lines with respect to the  $\hat{e}_z$  direction.

## 2. Testing the model

---

If we consider that the flow is incompressible we can express the magnetic and velocity fields as  $\mathbf{B} = B_0\hat{\mathbf{e}}_z + \nabla \times (a\hat{\mathbf{e}}_z + g\hat{\mathbf{e}}_x)$  and  $\mathbf{u} = \nabla \times (\varphi\hat{\mathbf{e}}_z + f\hat{\mathbf{e}}_x)$ . Assuming all potential fields are small compared with the external field and parallel spatial variations are small than perpendicular variations, it follows that the slow dynamics of the system is described by the RHMHD model. In a similar fashion, a weakly compressible model can be obtained as well with a slight modification [2]. The velocity field, in the more general case, can be decomposed as a superposition of a solenoidal part (incompressible flow) plus the gradient of a scalar field (irrotational flow), i.e.  $\mathbf{u} = \nabla \times (\varphi\hat{\mathbf{e}}_z + f\hat{\mathbf{e}}_x) + \nabla\psi$ . Using the same procedure [7], but in addition assuming that  $\psi$  is of order  $\alpha^2$ , the weak compressible RHMHD equations can be obtained (1.1.2.2)

The compressibility effect in the compressible RHMHD depends on the external magnetic field which embeds the plasma and it is introduced through a constant parameter. Therefore the computational cost is exactly the same in both the original and compressible RHMHD model.

In this section we compare the RHMHD model with compressibility effects and without it, to see how important is the role of compressibility in these systems and if the compressible RHMHD model is able to describe these effects.

The analysis performed on the results arising from the different simulations (both anisotropic and isotropic initial conditions) show a better fit with the full CMHD model when the compressible version of RHMHD is used. Figures (2.1) and (2.2) show different global parameters from the RHMHD simulations and its compressible version compared with the same parameters from the CMHD simulation. Here  $B_0 = 8$ , and the initial condition has the anisotropy introduced from the external magnetic field. It can be seen that there are slight differences for the incompressible RHMHD model whereas a near-perfect fit is observed for the weak compressible RHMHD version. The spectra also show noticeable improvements when the compressible version was used. When the external magnetic field is changed or using isotropic initial conditions, the weakly compressible RHMHD model still performs better. This result indicates on one hand that the relevant parameters of the MHD turbulence in strong magnetic fields are affected by slight compressibility effects, and on the other hand that the weakly compressible RHMHD seems to fit correctly the above mentioned compressibility effects.

It is necessary to emphasize that between the RHMHD set of equations and its compressible version, there is no difference in the computational cost. Therefore, hereafter we adopt the compressible version, and refer to it simply with the initials RHMHD. Below we compare this (weakly compressible) RHMHD model vs the CMHD model for different initial conditions and external magnetic fields.

## 2.2. Incompressible RHMHD Vs Compressible RHMHD

---

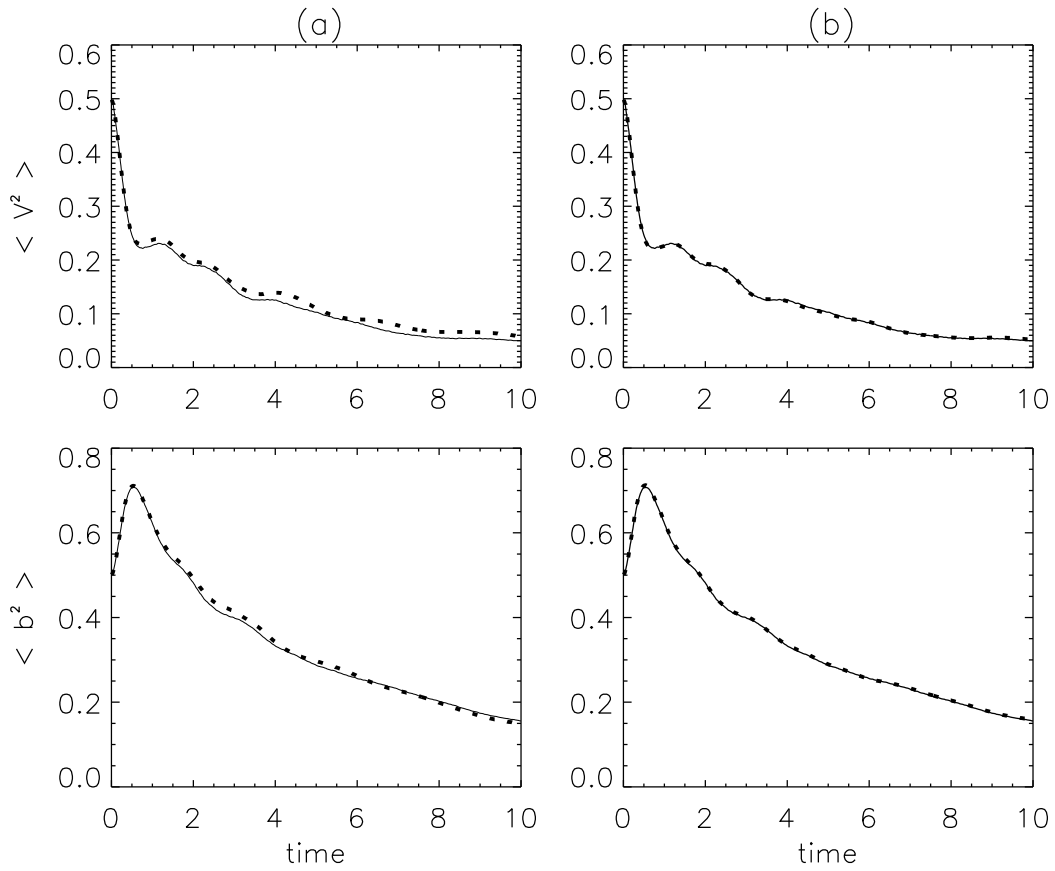


Figure 2.1: Kinetic energy (above) and magnetic energy (below) as function of time for the case  $B_0 = 8$  for anisotropic initial conditions. Column (a) shows the RHMHD model and Column (b) the weak compressible RHMHD model. The solid lines corresponds to the CMHD model and the dotted lines to RHMHD models.

## 2. Testing the model

---

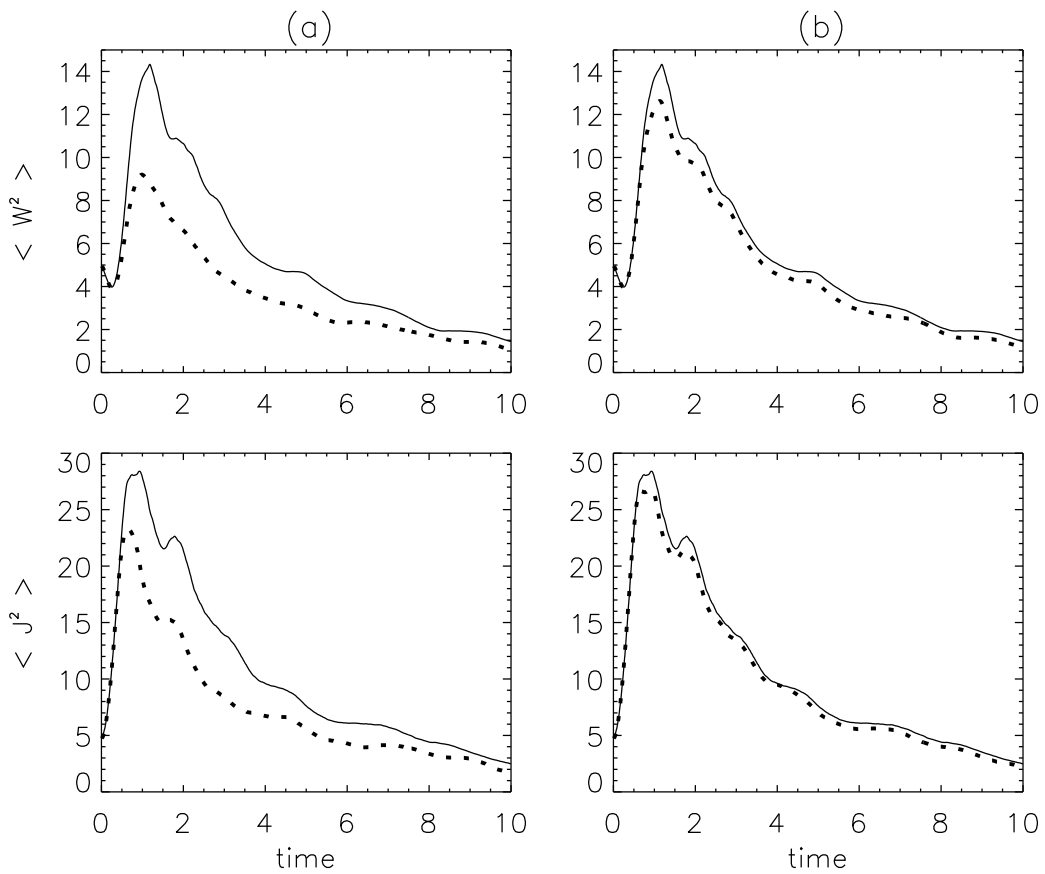


Figure 2.2: Vorticity (above) and current density (below) as function of time for the case  $B_0 = 8$  for anisotropic initial conditions. Column (a) shows the RHMHD model and Column (b) the weak compressible RHMHD model. The solid lines correspond to the CMHD model and the dotted lines to RHMHD models.

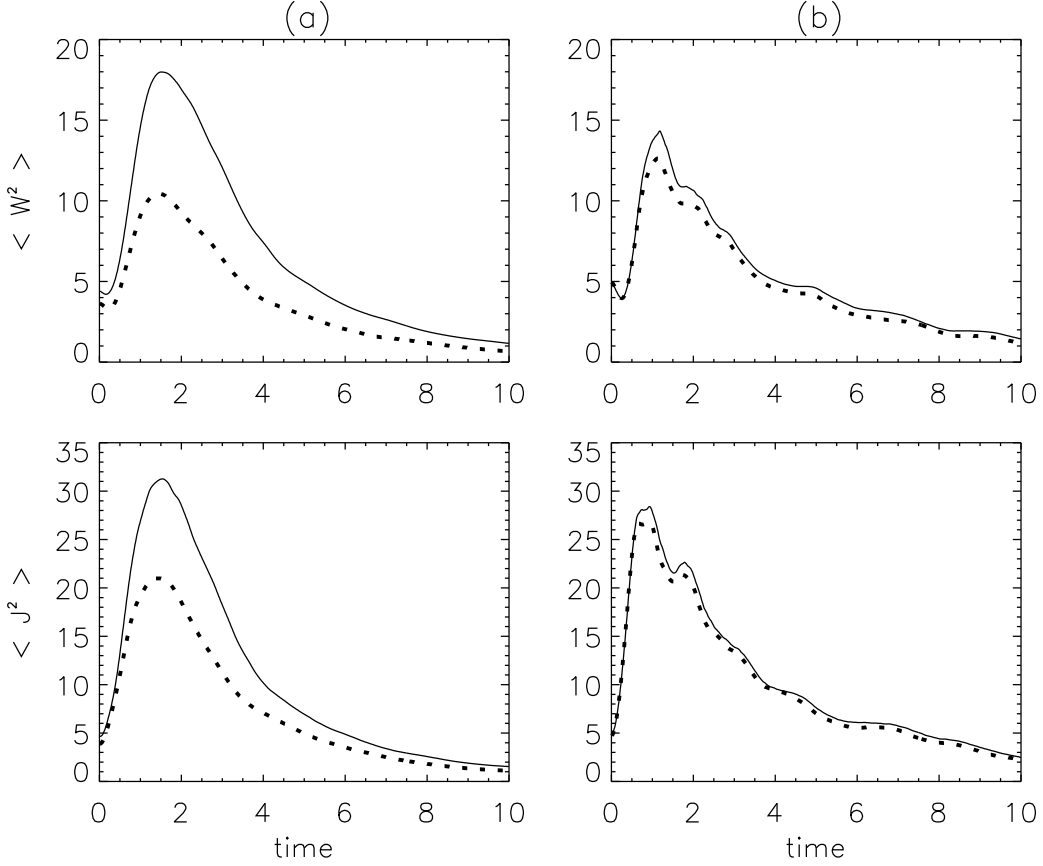


Figure 2.3: Vorticity (above) and current density (below) as function of time for anisotropic case. Column (a): the results for  $B_0 = 1$ , the solid lines correspond to the CMHD model and the dotted lines to RHMHD model. Column (b): same for the results with  $B_0 = 8$ .

## 2.3 Anisotropic initial conditions

In this section we show the testing of the RHMHD model in the context of anisotropic initial conditions (A.I.C.). We carry out runs for two different external magnetic field intensities,  $B_0 = 1$  and  $B_0 = 8$  (weak and strong magnetic field).

As expected, the global magnitudes studied show that the RHMHD equations fit better when the external field is sufficiently intense. Four of these magnitudes (enstrophy, current density, kinetic energy and magnetic energy) can be seen in figures 2.3 and 2.4.

To obtain a more quantitative measure of the distance between the two solutions (RHMHD and CMHD), we calculate the average distance for the magnitudes shown in the figures 2.3 and 2.4. We define this parameter, for a given magnitude  $a$ , as

$$\mathcal{E}_a = \frac{\int (a^{RHMHD} - a^{CMHD})^2 d^3t}{\int (a^{CMHD})^2 d^3t} \quad (2.3)$$

This is a less demanding measure of the correspondence between the RMHD approximation and the full MHD system, as compared to the distance used in Dmitruk et al 2005 which is

## 2. Testing the model

---

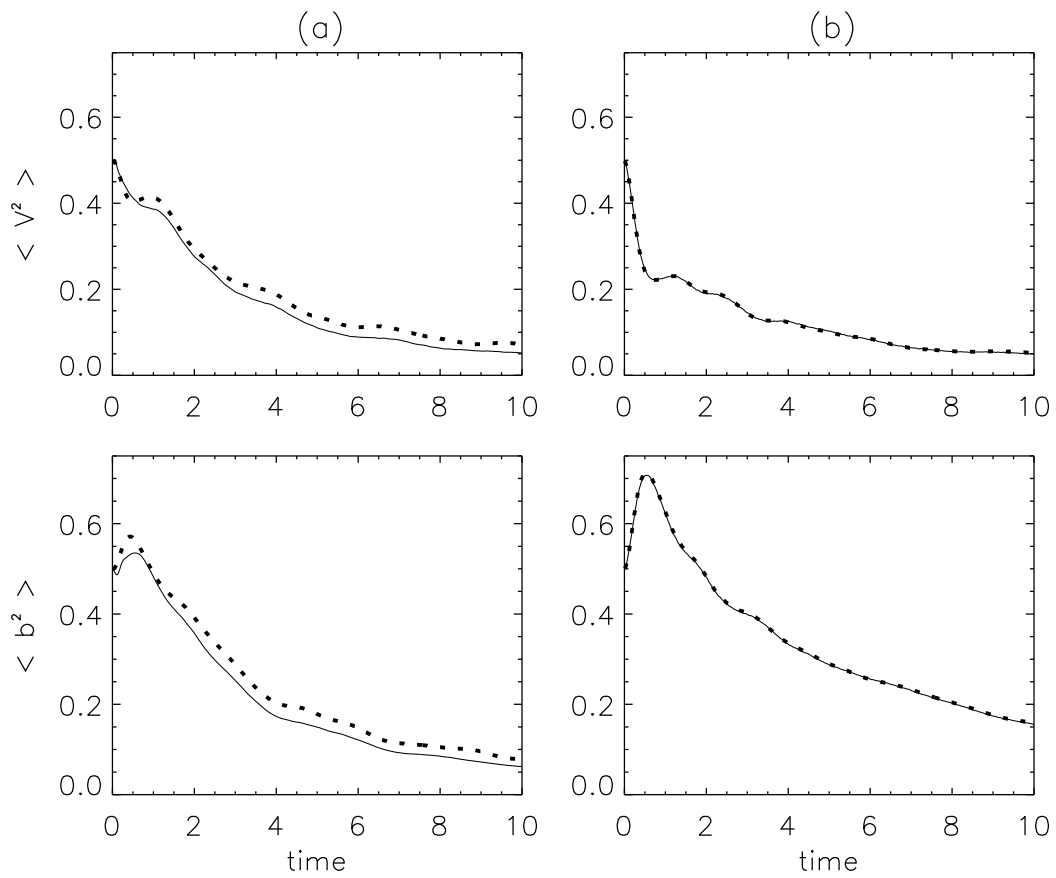


Figure 2.4: Kinetic energy (above) and magnetic energy (below) as function of time for anisotropic case. Column (a): the results for  $B_0 = 1$ , the solid lines correspond to the CMHD model and the dotted lines to RHMHD model. Column (b): same for the results with  $B_0 = 8$ .

Table 2.1: Anisotropic initial conditions

Magnitude	$B_0 = 1$	$B_0 = 8$
$\mathcal{E}_{\langle \mathbf{v}^2 \rangle}$	0.0100301	0.000299110
$\mathcal{E}_{\langle \mathbf{B}^2 \rangle}$	0.0244613	$3.74040 \times 10^{-5}$
$\mathcal{E}_{\langle \mathbf{w}^2 \rangle}$	0.189858	0.0112310
$\mathcal{E}_{\langle \mathbf{j}^2 \rangle}$	0.110552	0.00426486

based on a point-to-point distance average. However this simpler estimation is good enough for quantifying the differences between the two systems in a global sense. Table 2.1 shows this parameter for the magnitudes shown in Fig. 2.3 and 2.4. Here we can see that when increasing the external field the average distance decrease three orders of magnitude for the magnetic energy, and two for the kinetic energy. The current density decreases two orders of magnitude and the enstrophy one order. There is more than 99,9 % of agreement for kinetic and magnetic energy when  $B_0 = 8$ , and approximately 98 % for enstrophy and 99,95 % for current density. We can conclude that the RHMHD model is an optimal tool to characterize the global magnitudes and energy spectra when the initial condition satisfies the anisotropy imposed by the external field.

In standard RMHD, the parallel components to the external magnetic field do not affect the dynamics of the perpendicular fields, since they do not appear in the dynamic equations for these fields and in fact act as passive scalars. If the parallel components are initially zero, they will remain zero. This situation is, in principle, different in RHMHD, because the Hall effect couples the dynamics of the perpendicular components with the parallel components. This is evident in equations (1.49) - (1.52). If the parallel components are initially zero, they may not remain zero at subsequent times, because the Hall term act as a source in the evolution equations for those components. Therefore, it is relevant to analyze the behavior of the parallel components when starting from initial conditions such that only perpendicular fields are not zero. Figure 2.5 shows the parallel velocity and magnetic field rms (root mean square) values.

The ratio of parallel vs perpendicular components decrease with increasing external field, as shown in Fig. 2.6. In both cases the flow of energy between perpendicular components and the parallel component is stabilized. From the  $B_0 = 1$  up to  $B_0 = 8$  we can see that the parallel component goes from about 50 % to less than 6 % for the kinetic energy and 30 % to 1.5 % for the magnetic energy.

Energy spectra for both  $B_0 = 1$  and  $B_0 = 8$  are shown in Fig. 2.7 at a time  $t = 3$ . We can see that when the external field is small, there are slight differences between CMHD and

## 2. Testing the model

---

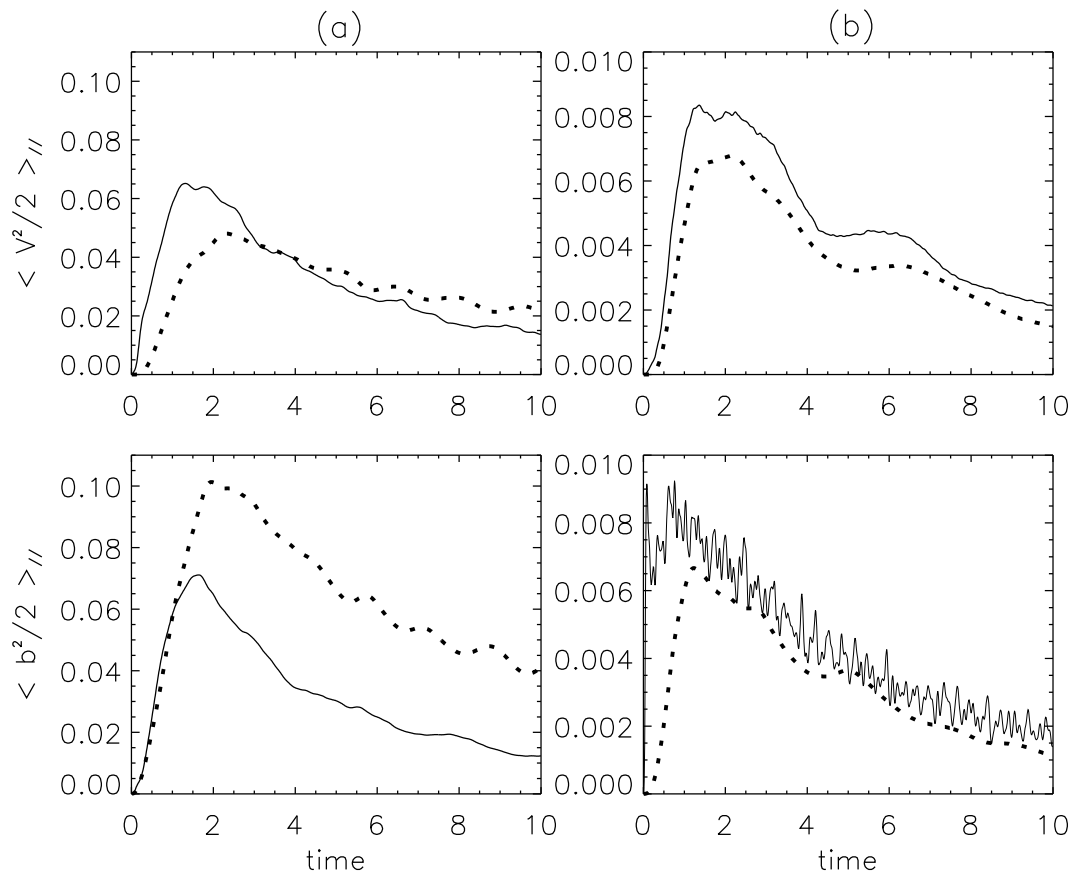


Figure 2.5: Parallel component of the kinetic energy (above) and magnetic energy (below) as functions of time for anisotropic case. Column (a) the case  $B_0 = 1$  and column (b) the case  $B_0 = 8$ . The solid lines correspond to the CMHD model and the dotted lines to RHMHD model.

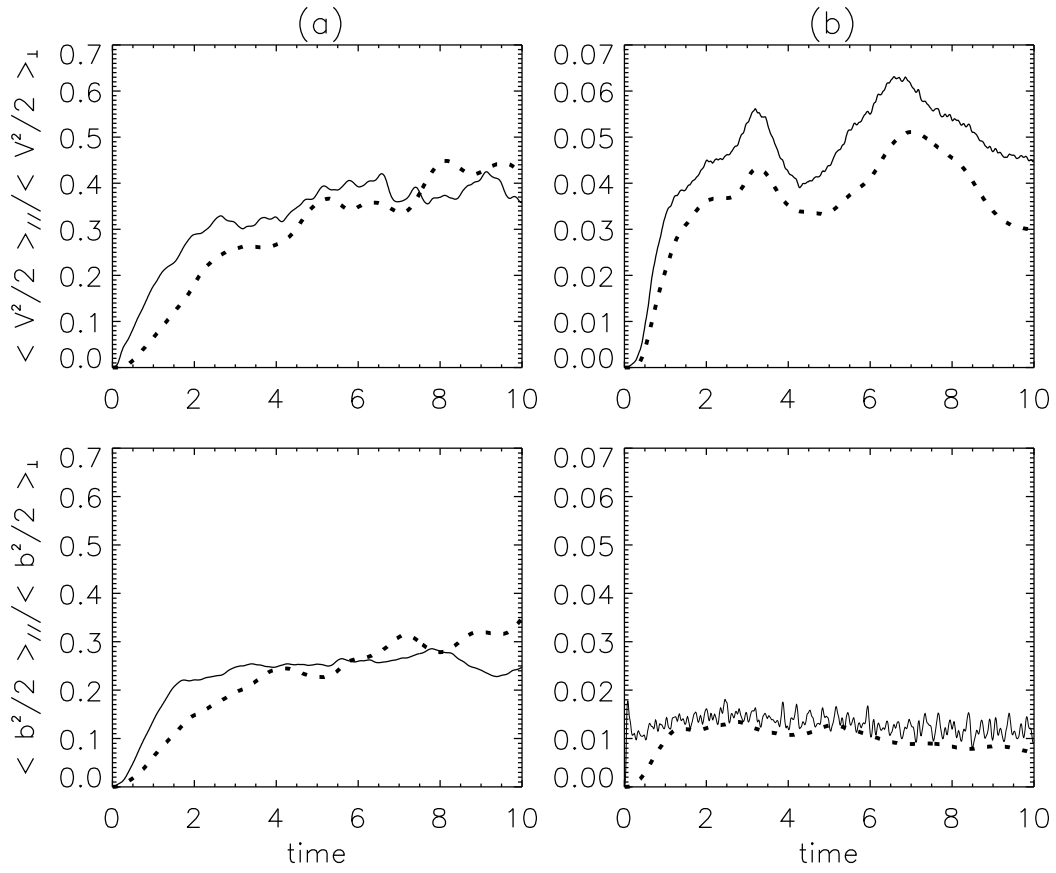


Figure 2.6: Ratio between the parallel component and perpendicular component for kinetic (above) and magnetic energy (below). Column (a) the case  $B_0 = 1$  and column b the case  $B_0 = 8$ . The solid lines correspond to the CMHD model and the dotted lines to RHMHD model.

## 2. Testing the model

---

the RHMHD model, but these differences disappear when the field increases. For the case  $B_0 = 8$ , the energy spectra of CMHD and RHMHD are identical. This shows that, when the external field is large enough and it maintains the anisotropy imposed by the initial conditions, the model reproduces the energy spectrum correctly. Therefore we can say that this is a robust model for spectral analysis in a anisotropic case.

### 2.4 Isotropic initial conditions

In the last subsection we analyze the behavior of the solutions of the RHMHD equations whenever the initial condition satisfies the anisotropy imposed by the external field. We showed that the parallel fluctuations hardly contributed to the evolution of the system and therefore that its evolution is restricted only to the perpendicular plane to the magnetic external field. When we consider isotropic initial conditions (and therefore fluctuations along the parallel direction) new effects will appear, the most obvious of which are the Alfvén waves. In this section we aim at quantifying these new effects into the RHMHD model and see if this model continues to reproduce correctly the dynamics of the system. Besides, since only low- $k$  modes are excited initially, we expect an energy cascade to develop and populate the large wavenumber modes after a few turnover times. We also expect the nonlinear activity to be considerably stronger than in the anisotropic case.

As in the anisotropic case we perform simulations with weak and strong magnetic field ( $B_0 = 1$  and  $B_0 = 8$ ), now considering isotropic initial conditions (I.I.C.). Figure 2.8 shows the vorticity and current density as a function of time. Here we can see, again, a substantial improvement of the fit of the RHMHD curve to the CMHD curve when the external field becomes more intense. For  $B_0 = 8$  both the overall performance as well as the small-scale fluctuations are correctly reproduced, the only difference that appears is a slight decrease in the amplitude of the RHMHD curve. However we again emphasize that the dynamics is well captured for these global quantities.

Figure 2.9 shows the kinetic and magnetic energy as a function of time. Here we see that the perfect agreement obtained in the anisotropic case (when  $B_0 = 8$ ) now gets lost. However the difference, as with the vorticity and current, is in an amplitude factor (now, a little bit more noticeable). Ignoring the differences due to the amplitude factor, we can see that the overall behavior is well described by the RHMHD model, in particular we can see that the fluctuations due to Alfvén waves are correctly described.

Table 2.2 shows the average distance for global parameters for isotropic initial conditions. Here we can see that, although the average distance has increased in comparison to anisotropic initial conditions, these are maintained below 3 %. Therefore the RHMHD model is still very

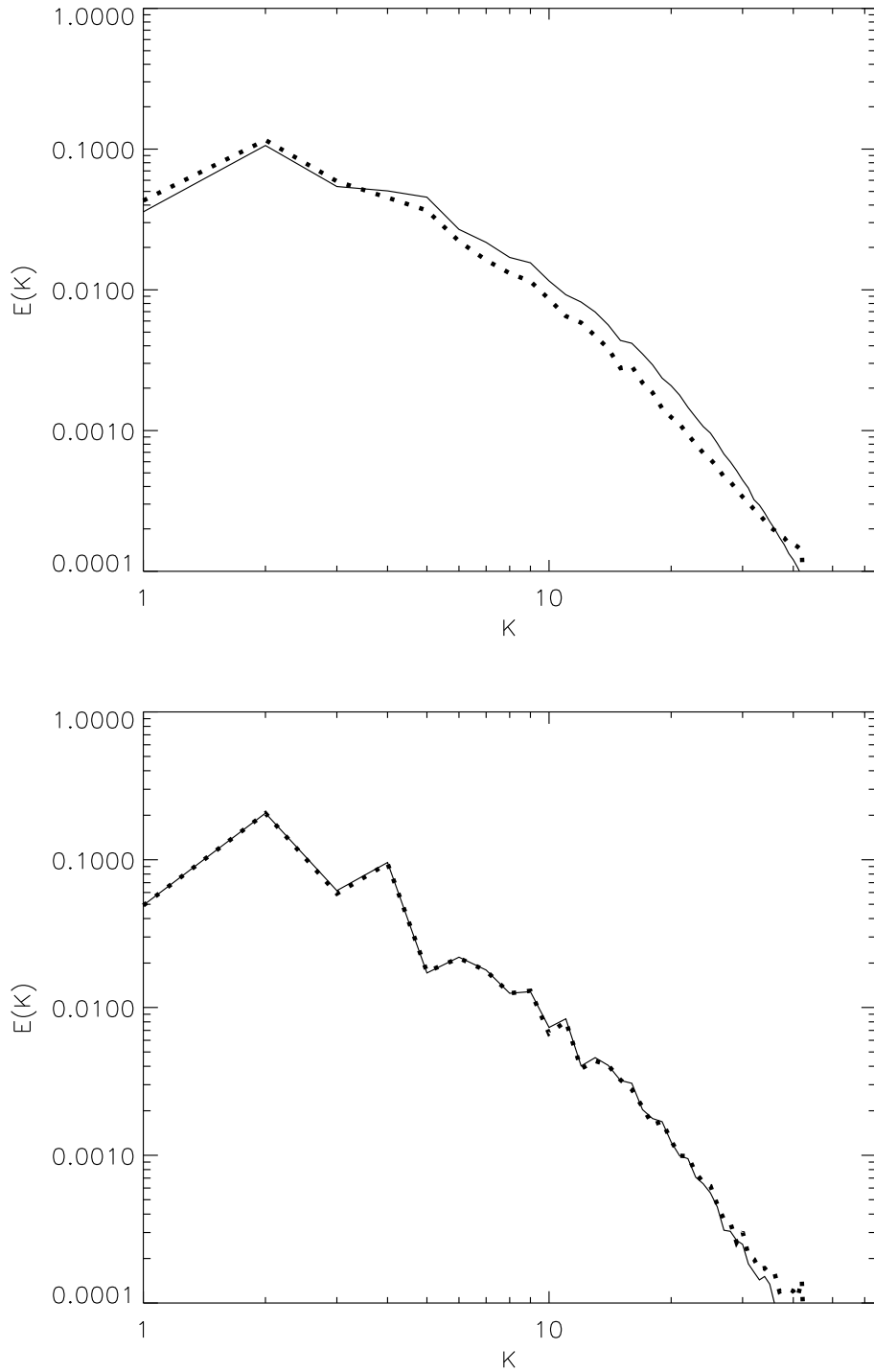


Figure 2.7: Energy spectrum (kinetic plus magnetic)  $E(k)$  for the cases  $B_0 = 1$  (above) and  $B_0 = 8$  (below), anisotropic initial conditions, and at  $t = 3$ . The solid lines correspond to the CMHD model and the dotted lines to the RHMHD model.

## 2. Testing the model

---

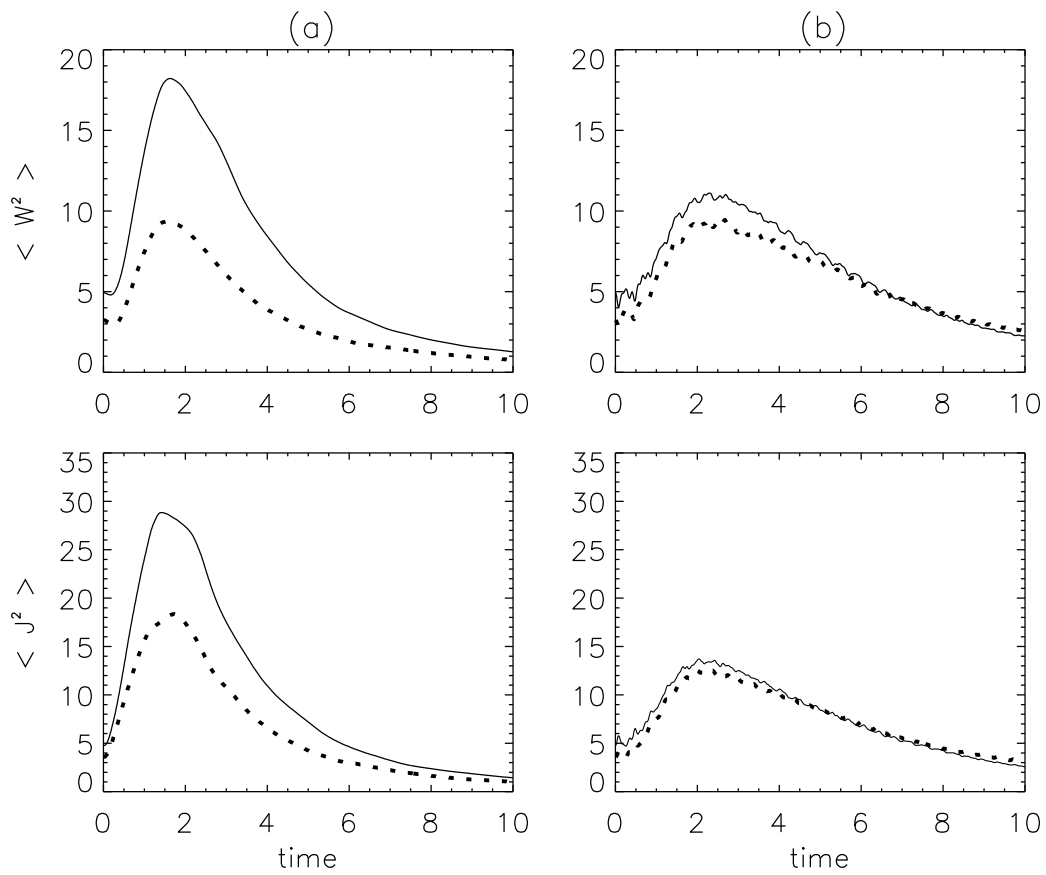


Figure 2.8: Vorticity (above) and current density (below) as function of time for isotropic case. Column (a): the results for  $B_0 = 1$ , the solid lines correspond to the CMHD model and the dotted lines to RHMHD model. Column (b): same for the results with  $B_0 = 8$ .

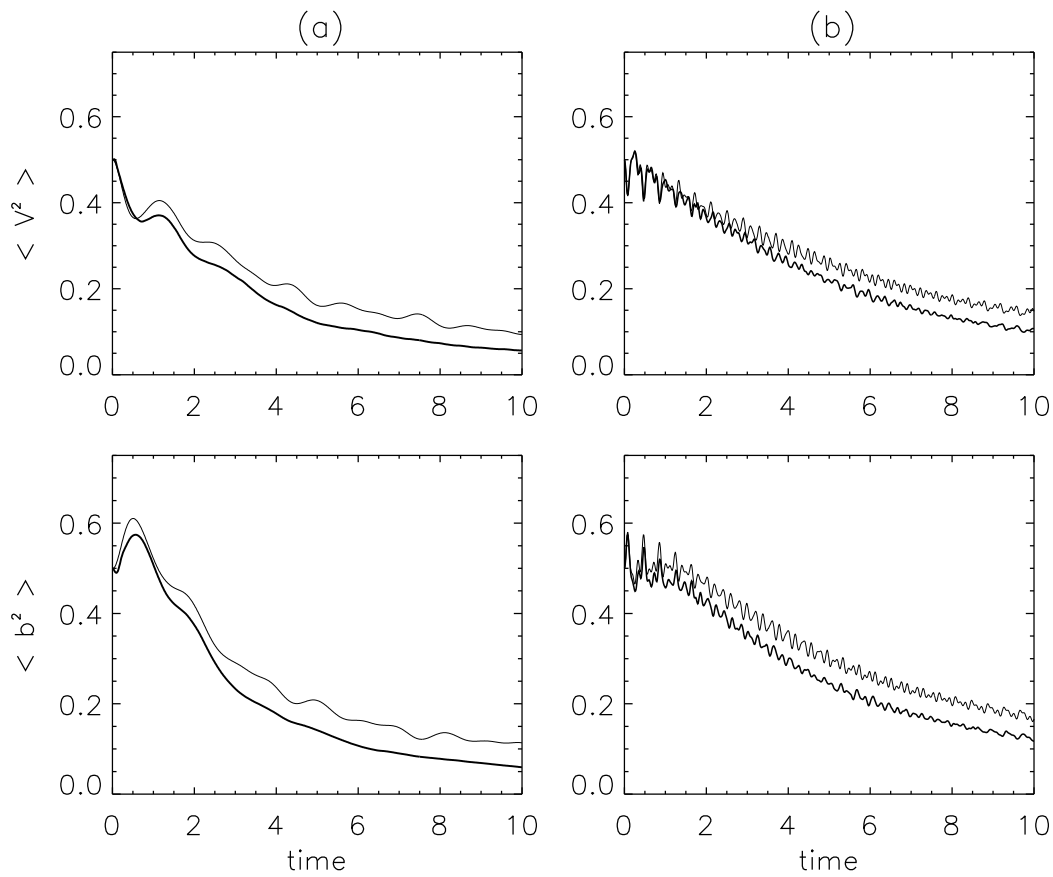


Figure 2.9: Kinetic energy (above) and magnetic energy (below) as function of time for isotropic case. Column (a): the results for  $B_0 = 1$ , the dark lines correspond to the CMHD model and the light lines to RHMHD model. Column (b): same for the results for  $B_0 = 8$ . Observe that we can see clearly Alfvén waves.

## 2. Testing the model

---

Table 2.2: Isotropic initial conditions

Magnitude	$B_0 = 1$	$B_0 = 8$
$\mathcal{E}_{\langle v^2 \rangle}$	0.0409073	0.0163489
$\mathcal{E}_{\langle B^2 \rangle}$	0.0335319	0.0244613
$\mathcal{E}_{\langle w^2 \rangle}$	0.249530	0.0193390
$\mathcal{E}_{\langle j^2 \rangle}$	0.142143	0.00701709

suitable for the description of the system, when the external magnetic field is large.

In figure 2.10, we show the energy spectra (for  $B_0 = 8$ ) at a time in which all the scales have been developed. Beside, we show the perpendicular energy spectra. Both spectra show a very good agreement of the RHMHD model with the full CMHD model.

The energy spectra for the RHMHD model shows a very good fit to the CMHD model, validating this model as a useful tool for spectral analysis of plasma embedded in strong magnetic fields even if the initial conditions do not maintain the anisotropy of the system. The reproducibility of the spectrum is a fundamental feature, because one of the open questions is whether the Hall effect might affect the energy inertial range. Given that we can reproduce correctly the spectra, the RHMHD model allows us to characterize the energy accumulated in each spatial scale in the flow; this indicates that we may use this model in the spatial characterization of the structures developed in the flow. With this new model, which offers significant computational advantages, we expect to be able to address unsolved questions like these.

## 2.5 Conclusions

We have numerically studied the validity of the RHMHD approximation doing a comparison between this model and the compressible 3D Hall-MHD equations. As originally proposed in [2], we took into account weak compressibility effects.

The results show that the of agreement is very high when the different assumptions of RHMHD, like spectral anisotropy, are satisfied. Nevertheless, when the initial conditions are isotropic but the mean magnetic field is maintained strong, the results differ at the beginning but asymptotically reach a good agreement at relatively short times. We also found evidence that the compressibility still plays a role in the dynamics of these systems, and the weak compressible RHMHD model is able to capture these effects.

The weakly compressible RHMHD model quantitatively reproduces all the global quantities when a large external magnetic field is present. The quality of the fit with the 3D results

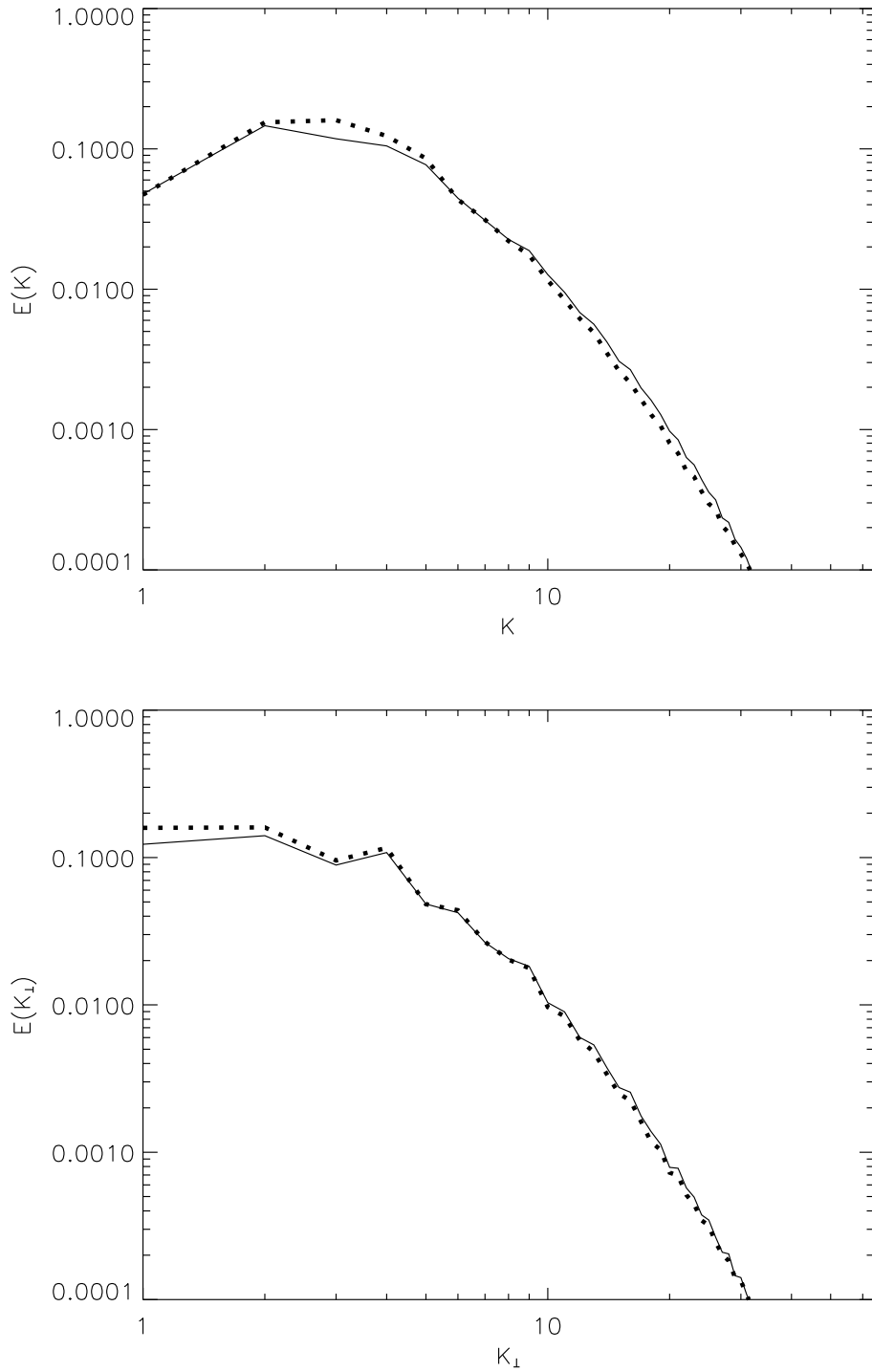


Figure 2.10: Energy spectrum (kinetic plus magnetic)  $E(k)$  (above) and perpendicular energy spectrum  $E(k_{\perp})$  (below) for the cases  $B_0 = 8$  for isotropic initial conditions at  $t = 3$ . The solid lines correspond to the CMHD model and the dotted lines to the RHMHD model.

## 2. Testing the model

---

show a slight decrease when the initial conditions do not comply with the anisotropy imposed by the external magnetic field. However, this decrease manifests itself in an amplitude factor, which does not alter significantly the dynamic evolution of the model. We have also observed that parallel component fluctuations to the external magnetic field remain small and do not grow with time.

The energy spectra are always well reproduced, regardless of whether the conditions are consistent with the symmetry of the system or not. Since important computational savings are offered by the RHMHD model, we can conclude that it can be an excellent tool to study the spectral properties of the system, in particular the characterization of the inertial range and the dissipation range.

In conclusion the weak compressible RHMHD model is a valid approximation of the Hall MHD turbulence in the relevant physical context.

# Bibliography

- [1] **L. N. Martin**, P. Dmitruk, Phys. Plasma **17**, 112304 (2010). [31](#)
- [2] N. H. Bian and D. Tsiklauri, Phys. Plasma **16**, 064503 (2009). [31](#), [34](#), [46](#)
- [3] H. R. Strauss, Phys. Fluids **19**, 134 (1976). [32](#)
- [4] D. C. Montgomery, Phys. Scr., T **T2/1**, 83 (1982) [32](#)
- [5] B. B. Kadomtsev and O. P. Pogutse, Sov. Phys. JETP **38**, 283 (1974) [32](#)
- [6] G. P. Zank and W. H. Matthaeus, J, Plasma Phys. **48**, 85 (1992). [32](#)
- [7] D. O. Gómez, S. M. Mahajan, and P. Dmitruk, Phys. Plasma **15**, 102303 (2008). [33](#), [34](#)



# Chapter 3

## Hall-magnetohydrodynamic with a strong guide magnetic field

[1]

### Contents

---

3.1 Set up . . . . .	51
3.2 Global magnitudes . . . . .	52
3.3 Energy spectrum . . . . .	55
3.4 Current sheets . . . . .	57
3.5 Conclusions . . . . .	62

---

In this chapter we study the general effects of the Hall term in magnetohydrodynamic turbulence in plasmas embedded in strong uniform magnetic fields. We will study the effect of this term on the dynamics of global magnitudes, the energy cascade, the characteristic scales and the dissipation range.

Numerical simulations of the RHMHD model are performed for different values of the Hall parameter, we use the isotropic initial conditions (I.I.C.) presented in the chapter 2.

### 3.1 Set up

The same resolution is used in all simulations,  $512^2$  in the perpendicular directions to the external magnetic field and 32 in the parallel direction (this is possible because the structures that require high resolution only take place in the directions perpendicular to the field). We performed simulations for four different Hall coefficients,  $\epsilon=0, 1/32, 1/16,$  and  $1/8$ .  $R = R_m = 1600$

### 3. Hall-magnetohydrodynamic with a strong guide magnetic field

---

( $\nu = 1/1600$ ,  $\eta = 1/1600$ ) in all runs. We also considered a Mach number  $M_S = 1/4$  and Alfvén number  $M_A = 1$ .

We use a strong enough magnetic field ( $B_0 = 8$ , in units of the initial rms magnetic fluctuation value). The magnetic field fluctuations were less than ten percent of the external magnetic field value, so we are in the range of validity of the RHMHD model.

We used the isotropic initial conditions described in chapter 2.

Remember that the simulations performed throughout this work do not contain any magnetic or velocity stirring terms, so the RHMHD system evolves freely.

## 3.2 Global magnitudes

We study the influence of the Hall term in global quantities associated with the dissipation. Figures 3.1 and 3.2 show the mean square current density  $\langle J^2 \rangle$  and mean square vorticity  $\langle \omega^2 \rangle$  as function of time for  $\epsilon=0, 1/32, 1/16, 1/8$ .

Both  $\langle J^2 \rangle$  and  $\langle \omega^2 \rangle$  show that as the Hall parameter is increased the dissipation decreases (in the case of mean square vorticity this effect is considerably larger). Another remarkable effect is the shift in the peaks of these functions:  $\langle J^2 \rangle$  and  $\langle \omega^2 \rangle$  take longer to reach its maximum with increasing  $\epsilon$ . The time of the peak indicates the time where all spatial scales were developed (and therefore turbulence is fully developed).

Figure 3.3 shows  $\langle J^2 + \omega^2 \rangle$  as function of time, the difference between the peaks is more clear in this case. Here we see two effects that occur simultaneously as the Hall coefficient is increased: The decrease in the dissipation and the delay in reaching the maximum point (and hence the time that it takes to develop all the scales). The first effect will have a direct impact on the dissipation scale of the respective flows while the second shows how the Hall term modifies its characteristic times.

It is relevant to note that the dissipation scale ( $1/K_{diss}$ ) is related to the number of scales that develop in the flow. It is common to consider that the decrease in the dissipation scale increases the range of developed scales in the flow (usually increases the size of the inertial range). However, this is not always the case. The results that we will show below indicate that the Hall term affects the total width of the dissipation range decreasing mildly the  $K_{diss}$  (and therefore mildly increasing the dissipation scale) with the increase of the  $\epsilon$ , at the same time the delay suffered by the dissipation peak is due to the development of a greater number of scales in the dissipative range due to a major accumulation of energy in these scales.

To quantify the dissipation scale (in Fourier space) of the different flows we use the conventional criteria [2] given by the equation (3.1).

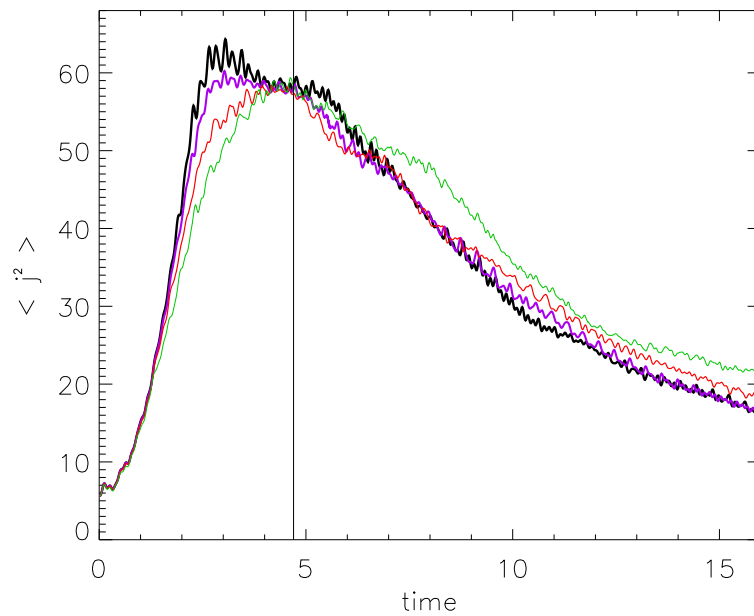


Figure 3.1: Current density,  $\langle J^2 \rangle$ , as function of time for  $\epsilon = 0$  (black line),  $\epsilon = 1/32$  (violet line),  $\epsilon = 1/16$  (red line) and  $\epsilon = 1/8$  (green line). The vertical straight line indicates a particular time where all the scales have been developed in all runs. Besides, in this time the value of  $\langle J^2 \rangle$  is approximately the same for all runs. This particular time will be used to study the different structures in the flows.

### 3. Hall-magnetohydrodynamic with a strong guide magnetic field

---

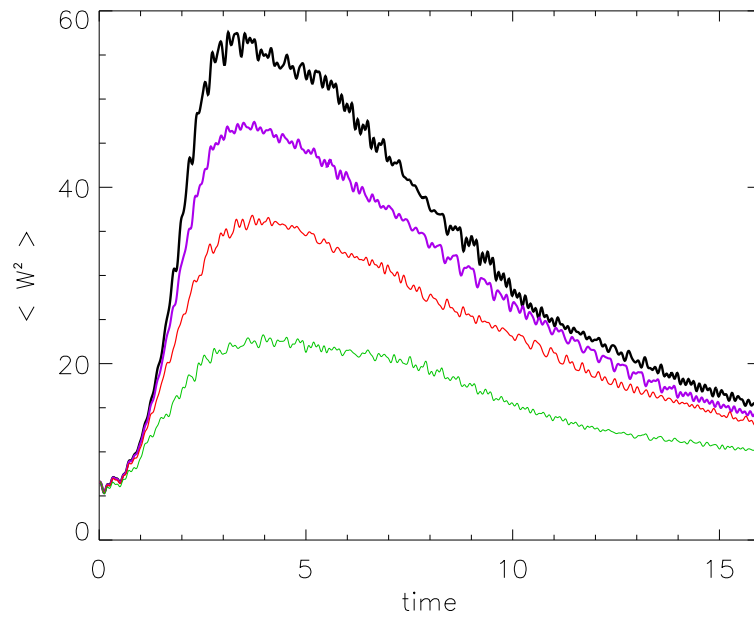


Figure 3.2: Vorticity,  $\langle \omega^2 \rangle$ , as function of time for  $\epsilon = 0, 1/32, 1/16$  and  $1/8$ . We are using the same convention of color as in figure 3.1

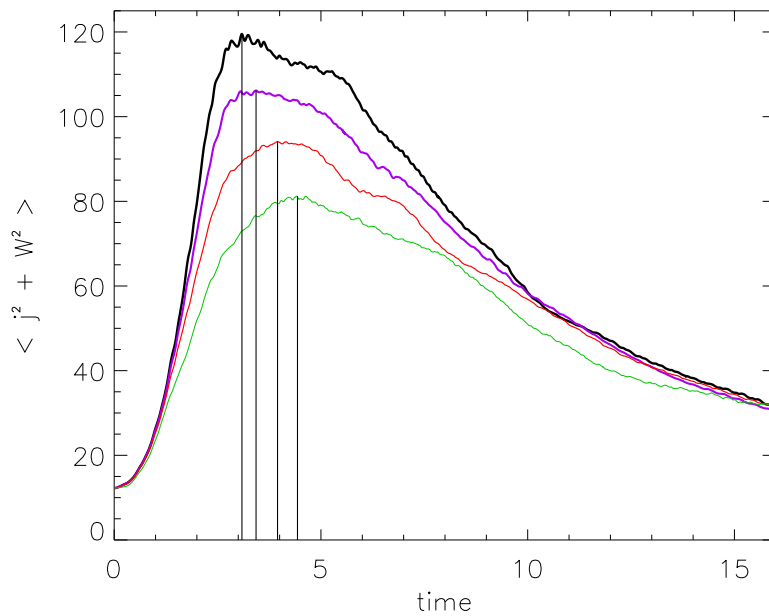


Figure 3.3:  $\langle J^2 + \omega^2 \rangle$  as function of time for  $\epsilon = 0, 1/32, 1/16$  and  $1/8$ . We are using the same convention of color as in figure 3.1. The vertical straight lines indicate the maximum value for each curve.

Table 3.1: Hall and dissipation scales for the different runs.

Run	$\epsilon$	$K_{Hall}$	$K_{diss}$
1	0		132.25
2	1/32	32	125.40
3	1/16	16	124.58
4	1/8	8	120.08

$$K_{diss} = \left( \frac{\langle \omega^2 \rangle + \langle J^2 \rangle}{\nu^2} \right)^{1/4} \quad (3.1)$$

In Table 3.1 the Hall scale is shown along with the dissipation scale for each one of the flows. Here we see the decrease of the  $K_{diss}$  in quantitative form with the increase of the Hall coefficient. Note that  $K_{diss} < K_{max} = N/3 = 170$  means that the runs are marginally resolved [3] (in the next chapter we show that our simulations satisfy the highest requirements if higher order statistic is performed[4])

The decrease of the global dissipation with the Hall parameter and the increase in the time of the peak development can not be understood by looking only at the temporal evolution of the global magnitudes. These effects could be due to a change in the characteristic time of the energy flow or to the development of small scale structures.

### 3.3 Energy spectrum

To better understand the question of the dissipation, we study in this section and the next one the energy spectra and the size and shape of the structures generated in the four runs. This can help us to see whether or not the Hall effect produces the development of small scales and also to understand this dynamic in terms of the energy distribution.

Looking at the spectra we can see the distribution of the energy through different scales. Figure 3.4 compares the energy spectra for all runs and Figure 3.5 shows a zoom around the Hall scales used. Since it is a reduced model, we used the perpendicular spectra  $E(K_{\perp})$  with  $K_{\perp} = \sqrt{K_x^2 + K_y^2}$ .

As the Hall parameter is increased the energy spectrum is steeper at intermediate scales preceding the dissipation range. At the same time there is an increase in the energy on scales smaller (larger  $K$ ) than the dissipation scale (see Figs. 3.4 and 3.5). The effect of the Hall term is then twofold: first there is a slow down of the energy transfer up to the Hall scale, resulting in a steeper spectrum, and then there seems to be a driving of energy from the Hall scale up

### 3. Hall-magnetohydrodynamic with a strong guide magnetic field

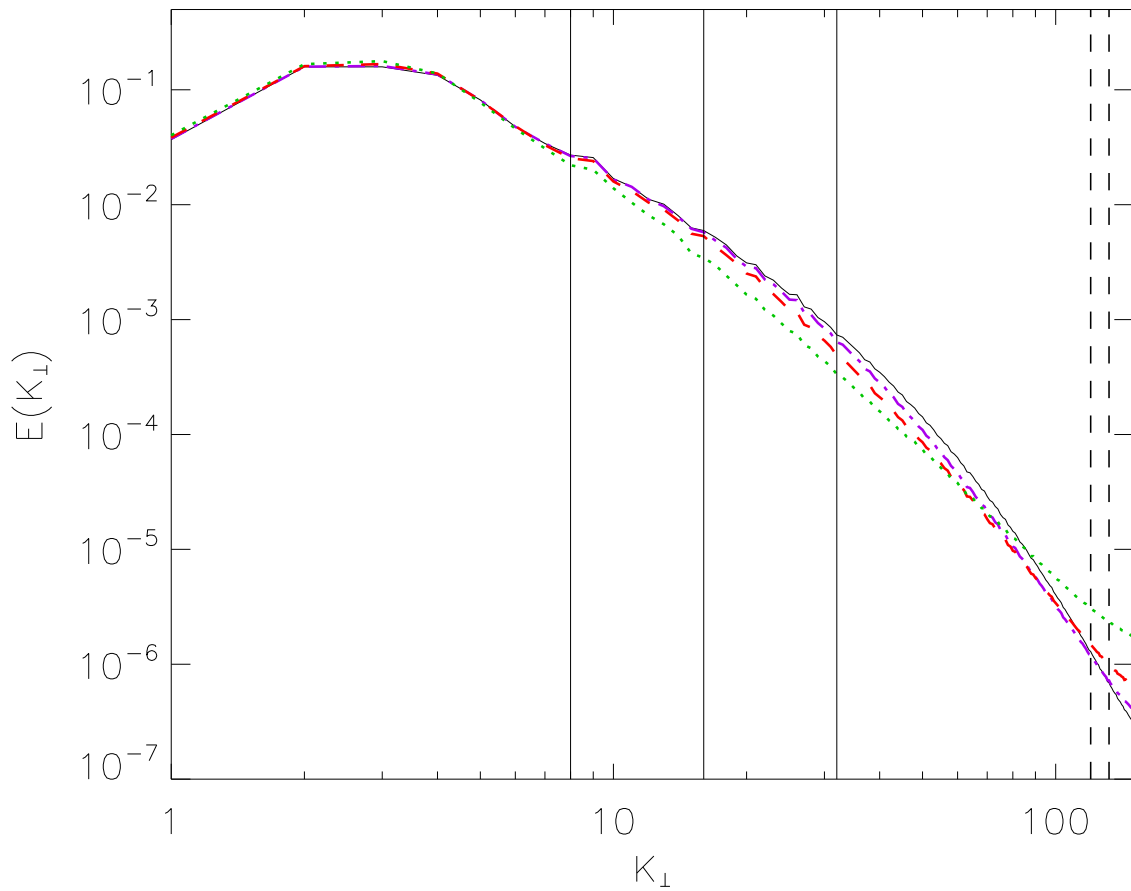


Figure 3.4: Energy perpendicular spectra for  $\epsilon = 0$  (solid line),  $\epsilon = 1/32$  (dash-dotted),  $\epsilon = 1/16$  (dash) and  $\epsilon = 1/8$  (dotted). Beside we are using the same convention of color as in figure 3.1. The vertical straight lines indicate the different values of  $K_{Hall} = 1/\epsilon$  for  $\epsilon = 1/32, 1/16, 1/8$ . The vertical straight dashed lines show the minimum and the maximum values of the  $K_{diss}$  ( $\epsilon = 1/8$  and  $\epsilon = 0$ ).

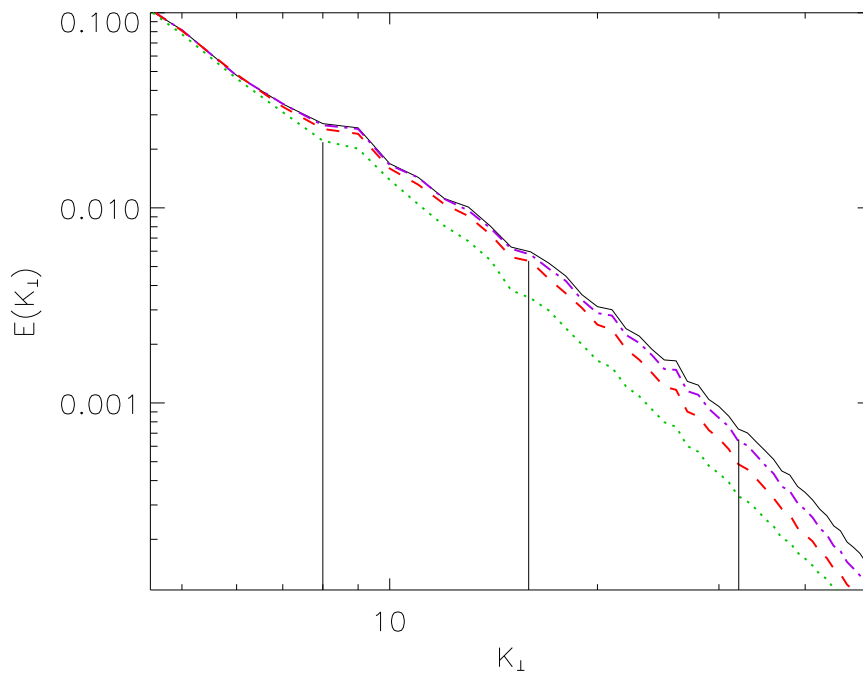


Figure 3.5: Enlarged view of a section of the energy spectra (limited  $K$ ). The vertical straight lines indicate the different values of  $K_{Hall} = 1/\epsilon$  for  $\epsilon = 1/32, 1/16, 1/8$ , these lines intersect each of the corresponding curves. Same convention as figure 3.4

to the small scales (see [5] for a study of how the Hall term affects the transfer of energy at different scales). A shift of the effective dissipation scale to larger scales is then to be expected (as indicated by the values of  $K_{diss}$  given before) as well as a decrease in the global dissipation values. At the same time, since the Hall term increases the number of effective scales on which the dynamics occurs (as evidenced by the extended spectra at small scales) a longer time to reach the peak of dissipation is expected, as previously shown.

### 3.4 Current sheets

Finally, we study the characteristic structures of the flow and the effect of the Hall term by looking at the current density field. This is a qualitative study, which however can help us to get intuition and guide future analysis. Chapter 5 is devoted to the quantification of this.

Figures 3.6-3.9 show the parallel component of the current density in a perpendicular plane to the external magnetic field at a given time for the different runs. The time was chosen in which all scales have been developed for all the flows (this time is indicated in Figure 3.4). Also, for this particular time, the value of  $\langle J^2 \rangle$  is approximately the same for all the runs.

### 3. Hall-magnetohydrodynamic with a strong guide magnetic field

---

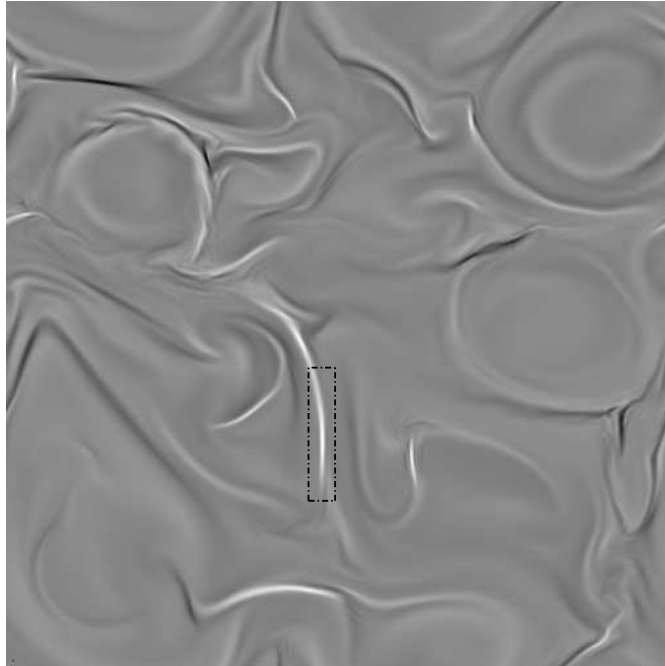


Figure 3.6: Parallel component of the current density in a perpendicular plane to the external magnetic field in the case with  $\epsilon = 0$ . Tones indicate out of plane current, with light tones=positive and dark tones=negative.

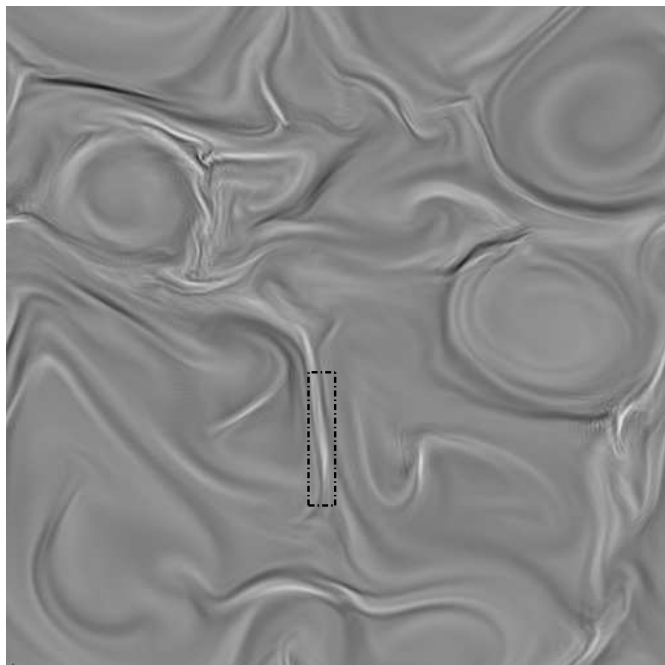


Figure 3.7: Parallel component of the current density in a perpendicular plane to the external magnetic field in the case with  $\epsilon = 1/32$ . Tones indicate out of plane current, with light tones=positive and dark tones=negative.

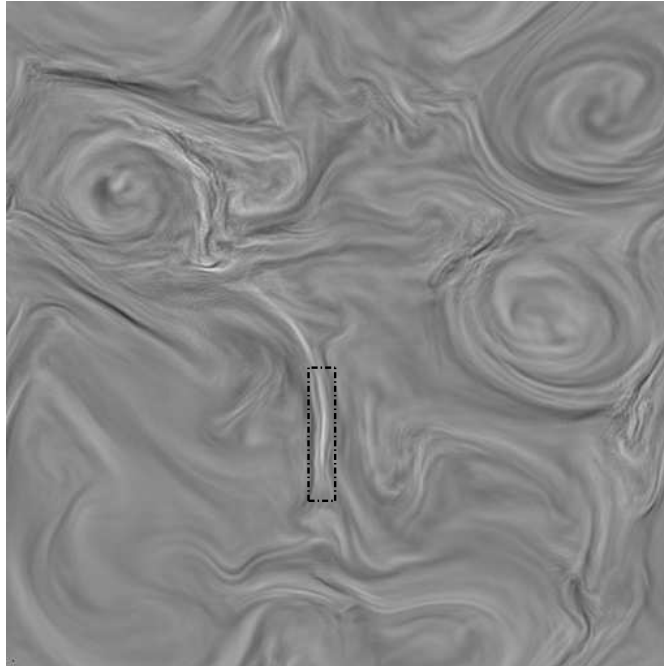


Figure 3.8: Parallel component of the current density in a perpendicular plane to the external magnetic field in the case with  $\epsilon = 1/16$ . Tones indicate out of plane current, with light tones=positive and dark tones=negative.

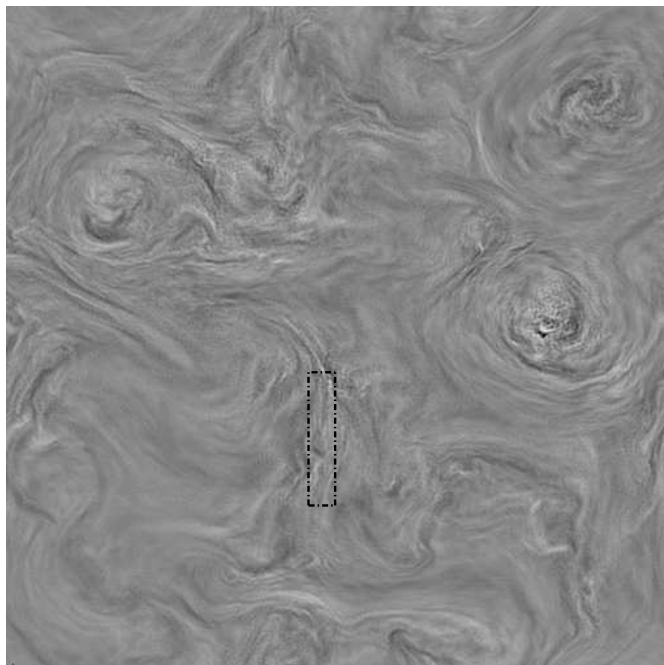


Figure 3.9: Parallel component of the current density in a perpendicular plane to the external magnetic field in the case with  $\epsilon = 1/8$ . Tones indicate out of plane current, with light tones=positive and dark tones=negative.

### 3. Hall-magnetohydrodynamic with a strong guide magnetic field

---

In Figure 3.6 ( $\epsilon = 0$ ) we can clearly distinguish the current sheets that form in the flow. We have highlighted one of the current sheets with a rectangle with dashed lines. This structure is localized and well defined. Looking at the change of this structure with the value of Hall parameter we can see two effects: first, a widening of the sheet and secondly an internal filamentation. The widening is very clear from Figure 3.6 with  $\epsilon = 0$  to Figure 3.7 with  $\epsilon = 1/32$  and the internal filamentation starts to be seen in the Figure 3.8, with  $\epsilon = 1/16$ , where also the thickness has increased. In the case with higher  $\epsilon = 1/8$  the current sheet is completely filamentated, and is hard to distinguish a clear structure at all.

These results are complementary to the results observed in the spectra and global magnitudes and corroborate the idea that the Hall effect results in an effective shift of the dissipation scale (current sheet thickness getting larger) but also an increase in the dynamical scale range (increase of filamentation).

To better quantify the effect we have just observed, we plot the profile of the current density in the direction perpendicular to the current sheet seen in the figures 3.6-3.9. These profiles are shown in Figure 3.10.

The net flow of current (the absolute value) is the same within the clear lines (vertical outside lines). When  $\epsilon = 0$  the current sheet is perfectly defined (the dark lines mark the original position of the current sheet when  $\epsilon = 0$ ) and it is homogeneous (in the sense that we have a single well defined peak). When  $\epsilon = 1/32$  the original sheet expands and two sheets or filaments appear in their place (there are now two peaks). For  $\epsilon = 1/16$  the width of the main sheet is greater and there is now a clear internal structure. In this case the ambiguity that arises is whether we have one or more current sheets (compare Figure 3.10 with 3.8) and hence the ambiguity of whether we have a wider sheet or two thin sheets. When  $\epsilon = 1/8$  there is no trace of the current sheet.

At this point we should make an important observation about the evolution of current sheets as a function of the Hall parameter. As we saw there are two effects acting simultaneously, the widening of what could be considered the overall structure of the sheet and the internal filamentation that this suffers. In this way it could be interpreted that the Hall effect widens the current sheets (if we see the entire structure like the sheet) or on the other hand the Hall effect produces finer sheets (considering that the small filaments are the sheets). To remove the ambiguity (in semantics), we propose to speak in terms of dissipation, so if the global structure dissipates less energy as we increase the Hall parameter we will say that the sheet is being widened, otherwise, if more energy is dissipated we will say that the relation between size and intensity of internal filaments allow us to identify new current sheets. Our results agree with the first frame of mind: as a function of dissipation the current sheets are widening and even more when  $\epsilon = 1/8$  there is no trace of any structure that could be identified as a

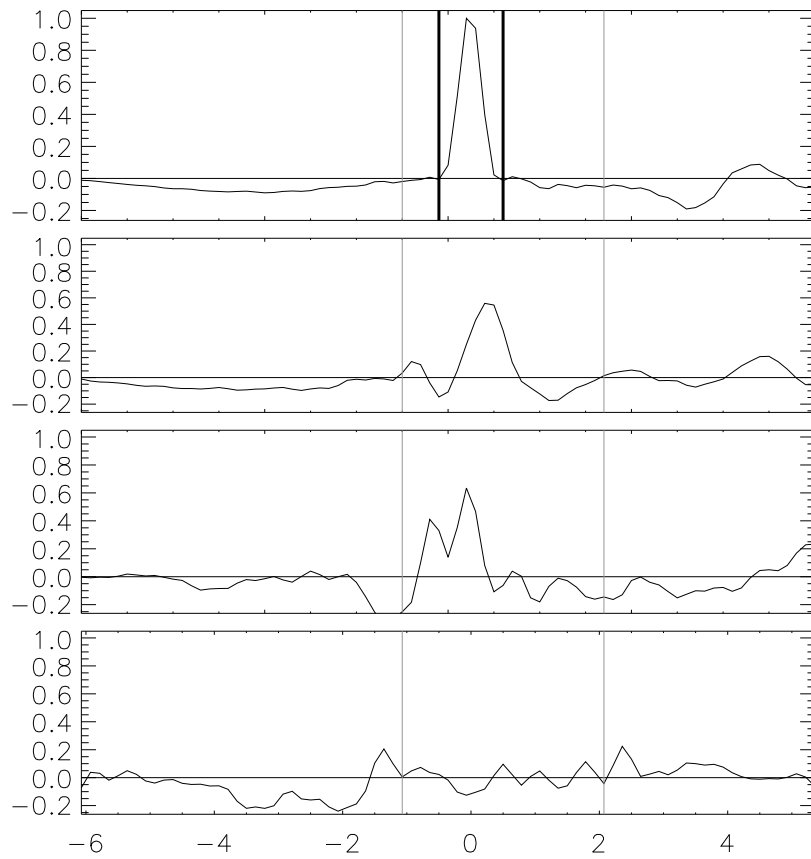


Figure 3.10: Current density profile of the current sheets studied. From top to bottom are the cases with  $\epsilon = 0$ ,  $\epsilon = 1/32$ ,  $\epsilon = 1/16$ , and  $\epsilon = 1/8$ . The net flow of current (the absolute value) is the same within the clear lines (vertical outside lines), and the dark lines mark the original position of the current sheet when  $\epsilon = 0$ .

### 3. Hall-magnetohydrodynamic with a strong guide magnetic field

---

current sheet.

## 3.5 Conclusions

We performed numerical simulations of magnetohydrodynamic turbulence in strong magnetic fields, including the Hall effect, and varying the Hall parameter.

We found that the Hall term affects the scales that are situated between the Hall scale and the dissipation scale, resulting in a decrease in the accumulation of energy in this scale range. The result is an effective shift of the dissipation scale but also a transfer of energy to smaller scales. When the separation between the Hall scale and the dissipation scale is larger an increasingly sharp steepening of the energy spectrum occurs at this range of scales. The final outcome is the generation of smaller scales when the Hall scale increases.

Localized structures are destroyed by this effect, suffering a gradual filamentation with the increase of the Hall scale. The latter effect is manifested, for example, in the widening of the current sheets and the formation of internal structures within the sheets. At the same time a decrease of the total energy dissipated is observed.

The results presented here suggest that the Hall effect reduces the intermittency, however a more detailed study of this property should be performed. We will discuss this issue in the next chapter.

# Bibliography

- [1] **L. N. Martin**, P. Dmitruk, and D. O. Gómez, *Phys. Plasmas*, **19**, 052305 (2012). [51](#)
- [2] D. Biskamp, *Magnetohydrodynamic Turbulence* (Cambridge University Press, Cambridge, England, 2003). [52](#)
- [3] C Canuto, A Quarteroni , Approximation results for orthogonal polynomials in Sobolev spaces, *Math. Comp.* **38**, 67, (1982). [55](#)
- [4] M. Wan, S. Oughton, S. Servidio, and W. H. Matthaeus, *Phys. Plasma* **17**, 082308 (2010). [55](#)
- [5] P. D. Mininni, A. Alexakis, and A. Pouquet, *J. Plasma Phys.* **73**, 377 (2007). [57](#)



# Intermittency

[1]

## Contents

---

<a href="#">4.1 Hall effect and intermittency</a>	65
<a href="#">4.2 Set up</a>	67
<a href="#">4.3 Measures of intermittency</a>	67
<a href="#">4.4 Energy spectrum: Inertial range</a>	69
<a href="#">4.5 Structure functions and scaling exponents</a>	71
<a href="#">4.6 Probability density functions</a>	77
<a href="#">4.7 Effect of resolution</a>	78
<a href="#">4.8 Conclusions</a>	82

---

In the present chapter we show a detailed study of intermittency of compressible Hall-magnetohydrodynamic turbulence with an external guide field. The resulting data is analyzed computing field increments in several directions perpendicular to the guide field, and building structure functions and probability density functions. Also, we study the effect of resolution and study whether or not the simulations are properly resolved

## 4.1 Hall effect and intermittency

The properties of small scale structures in magnetohydrodynamic (MHD) and Hall magnetohydrodynamic (HMHD) turbulence have been the subject of conflicting results and of several debates. In particular, much attention has been paid in the literature to the geometrical properties of current sheets in HMHD, as these structures are associated with magnetic flux recon-

#### 4. Intermittency

---

tion and magnetic energy dissipation, processes of uttermost importance in astrophysics and space physics [2, 3, 4, 5].

While some numerical simulations indicate that current sheets affected by the Hall effect are wider than in MHD (see, e.g., [6]), others observe thinner structures [7]. In all cases, the geometry of the currents sheets is changed, displaying the so-called X-type structure and reminiscent of the Sweet-Parker configuration in the MHD case [8], and changing to a double wedge shape reminiscent of the Petschek configuration when the Hall effect is relevant [9]. In simulations of turbulent HMHD, it was observed that the peak of the spectrum of the current density was located at a wavenumber corresponding to the inverse of the ion skin depth [10, 11, 12, 13]. Since this peak can be associated with an average thickness of the current sheets, the effect was interpreted as a thickening of the current sheets as the Hall effect was increased [14]. The result is in good agreements with experiments that indicate that the thickness of the current sheet in the presence of the Hall effect is given by the ion skin depth [9].

The case in which thinner structures were observed [7] suggests that HMHD is more intermittent than MHD. This is also the case in some observations in the solar wind turbulence using the Cluster magnetic data [15, 16]. However, other observations in the solar wind of high-frequency magnetic field fluctuations from the same spacecraft indicate that while large scales are compatible with multifractal intermittent turbulence, small scales show non-Gaussian monoscaling [17].

A quantification of the level of intermittency is important to understand the geometrical distribution of dissipation in a magnetofluid and a plasma, and it also can provide constraints for theories of magnetic energy dissipation and reconnection. While previous analysis of intermittency in HMHD were mostly based on the differences observed in the geometry and size of current sheets, or in the study of probability density functions (PDFs) of field increments at different scales, a precise quantification requires computation of both PDFs and of structure functions.

The study of intermittency based solely on observations of individual structures has several shortcomings. Although the formation of small scale structures can point out to an increase in the level of intermittency, there is more information that is needed to make such claim. If there are thinner structures, are these structures spatially localized? Or do they occupy more space than in the MHD case, thus being space filling? In the former case, HMHD would be more intermittent, while in the latter case intermittency would be decreased by the Hall effect.

We use the reduced MHD (RMHD, [18, 19]) and reduced HMHD (RHMHD, [20, 21]) models to generate data under the approximation of a strong guide field (see also [22] for studies of kinetic plasma effects using other reduced models). Then, structure functions and PDFs of the fields are computed, for increments in the direction perpendicular to the guide field. To reduce

errors, an average of the structure functions for several directions perpendicular to the guide field is computed using the SO(2) decomposition [23, 24, 25].

## 4.2 Set up

Simulations analyzed here are exactly the same that in chapter 3. Also we carry out higher resolution simulations to see how this affects the results. This is extremely important because in the study of intermittency (or geometry of the structures in the flow) resolution is often responsible for spurious results.

Below we show the nomenclature used to develop the rest of the chapter.

As before, four values for  $\epsilon$  were considered, namely  $\epsilon = 0$  (run A, MHD),  $1/32$  (run B),  $1/16$  (run C), and  $1/8$  (run D). As the numerical domain used has size  $2\pi$  (see above in the thesis), these values correspond respectively to ion skin depths with associated wavenumbers  $k_\epsilon = \infty, 32, 16,$  and  $8$ . Data from these simulations is used for the analysis in Sec. 4.4, 4.5 and 4.6.

To quantify the effect of spatial resolution in the level of intermittency, runs A and D were computed also (with the same parameters) using larger grids, first with spatial resolution of  $768^2 \times 32$  grid points, and later with  $512^2 \times 64$  grid points. This second set of simulations (namely runs A2 and A3, with  $\epsilon = 0$ , and D2 and D3, with  $\epsilon = 1/8$ ) are considered in Sec. 4.7.

## 4.3 Measures of intermittency

In this section we develop different tools and techniques for the study of intermittency. In order to characterize velocity and magnetic field anisotropy, scaling laws and intermittency, we present in the following sections power spectra, structure functions, and PDFs of velocity and magnetic field increments.

The perpendicular total energy spectrum  $E(k_\perp)$  is defined as usual, summing the power of all (velocity and magnetic) modes in Fourier space over cylindrical shells with radius  $k_\perp$ , with their axis aligned with the direction of the guide field.

To compute structure functions and PDFs, field increments must be first defined. Given the presence of the external magnetic field, it is natural to consider an axisymmetric decomposition for the increments. In general, the longitudinal increments of the velocity and magnetic fields are defined as:

$$\delta u(\mathbf{x}, \mathbf{l}) = [\mathbf{u}(\mathbf{x} + \mathbf{l}) - \mathbf{u}(\mathbf{x})] \cdot \frac{\mathbf{l}}{|\mathbf{l}|}, \quad (4.1)$$

$$\delta b(\mathbf{x}, \mathbf{l}) = [\mathbf{b}(\mathbf{x} + \mathbf{l}) - \mathbf{b}(\mathbf{x})] \cdot \frac{\mathbf{l}}{|\mathbf{l}|}, \quad (4.2)$$

#### 4. Intermittency

---

where the spatial increment  $\mathbf{l}$  can point in any direction. Structure functions of order  $p$  are then defined as

$$S_p^u(\mathbf{l}) = \langle \delta u^p(\mathbf{x}, \mathbf{l}) \rangle, \quad (4.3)$$

for the velocity field, and as

$$S_p^b(\mathbf{l}) = \langle \delta b^p(\mathbf{x}, \mathbf{l}) \rangle, \quad (4.4)$$

for the magnetic field. Here, brackets denote spacial average over all values of  $\mathbf{x}$ .

These structure functions depend on the direction of the increment. For isotropic and homogeneous turbulence, it is a standard practice to average over several directions, to obtain the isotropic component of the structure functions (see, e.g., [26, 27, 23]). Due to the axisymmetry associated with the external magnetic field, in our case we will be interested instead only in the increments perpendicular to  $\hat{z}$ . We denote increments in this direction as  $\mathbf{l}_\perp$ , and we follow the procedure explained in [24, 25] to average over several directions of  $\mathbf{l}_\perp$ .

The method can be described as follows. Velocity and magnetic field structure functions were computed from Eqs. (4.3) and (4.4) using 24 different directions for the increments  $\mathbf{l}$ , generated by integer multiples of the vectors  $(1, 0, 0)$ ,  $(1, 1, 0)$ ,  $(2, 1, 0)$ ,  $(3, 1, 0)$ ,  $(0, 1, 0)$ ,  $(-1, 1, 0)$ ,  $(1, 2, 0)$ ,  $(-2, 1, 0)$ ,  $(-1, 2, 0)$ ,  $(1, 3, 0)$ ,  $(-3, 1, 0)$ , and  $(-1, 3, 0)$  (all vectors are in units of grid points in the simulations), plus the 12 vectors obtained by multiplying them by  $-1$ . Once these structure functions were calculated, the perpendicular structure functions  $S_p^u(l_\perp)$  and  $S_p^b(l_\perp)$  were obtained by averaging over these 24 directions in the  $xy$  plane.

For all runs, this procedure was applied to 9 snapshots of the velocity and magnetic fields, centered around the time of the peak of maximum dissipation (at  $t \approx 4.5$ ), and separated by intervals  $\Delta t = 0.5$  to improve the statistic.

For large enough Reynolds number, the structure functions are expected to show inertial range scaling, i.e., we expect that for some range of scales  $S_p^u \sim l_\perp^{\xi_p}$  and  $S_p^b \sim l_\perp^{\zeta_p}$ , where  $\xi_p$  and  $\zeta_p$  are respectively the scaling exponents of order  $p$  of the velocity and magnetic field. As sufficient scale separation is needed to determine these exponents, in the following section we show scaling exponents for runs A ( $\epsilon = 0$ ) and D ( $\epsilon = 1/8$ ), as these runs have well defined MHD (run A) or HMHD (run D) inertial ranges. Runs B and C have the ion skin depth in the middle of the inertial range, and each subrange (the MHD subrange and the HMHD subrange) is not sufficiently resolved to compute exponents.

The scaling exponents for each snapshot of the fields are obtained from the structure functions  $S_p^u$  and  $S_p^b$  using the least square method (extended self-similarity [28, 29] is not used to estimate the exponents). The values presented in the following section correspond to the time average over the 9 snapshots of each field. As the errors in the least square calculation are negligible when compared with the variations for each snapshot, the errors in the determination of the scaling exponents are estimated by the statistical mean square error; e.g., for the magnetic

field scaling exponents the error is

$$e_{\zeta_p} = \frac{1}{M} \sqrt{\sum_{i=1}^M (\zeta_{p_i} - \bar{\zeta}_p)^2}, \quad (4.5)$$

where  $M = 9$  is the number of snapshots of the field used in the analysis,  $\zeta_{p_i}$  is the slope obtained from a least square fit for the  $i$ -th snapshot, and  $\bar{\zeta}_p$  is the mean value averaged over all snapshots.

Finally, to complete the analysis, we consider PDFs of longitudinal increments and of derivatives of the perpendicular velocity and magnetic fields. In all cases, the PDFs are normalized by their variance, and will be shown together with a Gaussian with unit variance as a reference.

## 4.4 Energy spectrum: Inertial range

Before proceeding with the analysis of intermittency, we briefly present the total energy spectrum for all the runs with spatial resolution of  $512^2 \times 32$  grid points. This is important as determination of the inertial range based on the spectrum and on the structure functions is needed to compute the scaling exponents of the fields.

Figure 4.1 shows the perpendicular spectrum for the total energy (kinetic plus magnetic) in runs A, B, C, and D. In run A, a range of wavenumbers following an approximate power law can be identified, namely from  $k_{\perp} \approx 4$  to  $k_{\perp} \approx 20$ . This range is used to compute scaling exponents below. As a reference, we also show in Fig. 4.1 a Kolmogorov slope. However, it should be noted that determination of the slope of the MHD energy spectrum is beyond the interest of this work, and readers interested in the topic are referred to detailed recent studies on the subject [30, 31, 32, 33].

It is also interesting to note that the energy spectrum in Fig. 4.1 is shallower than that expected for weak turbulence [34, 35, 36, 37, 38], even though the reduced equations are written for  $|\mathbf{b}'| \ll B_0$ . Indeed, we verified that most of the energy in the simulations is in non-propagating modes (i.e., modes with  $k_{\parallel} = 0$ , see [39]). We also verified explicitly that the condition  $|\mathbf{b}'|/B_0 \ll \Delta k_{\parallel}/k_{\perp}$  is violated, where  $\Delta k_{\parallel}$  is the grid spacing in the parallel direction in Fourier space, and  $k_{\perp}$  is a characteristic perpendicular wavenumber (obtained from the flow perpendicular integral scale). This condition is required in RMHD for weak turbulence to develop [36]), and as a result we will understand the following results in the framework of strong turbulence.

As the value of  $\epsilon$  in the simulations is increased (see runs B, C, and D in Fig. 4.1), the spectrum becomes steeper at wavenumbers larger than  $k_{\epsilon}$ . This trend has been observed before in simulations [40, 41, 14], and it has been argued that it can result in an inertial range in the

## 4. Intermittency

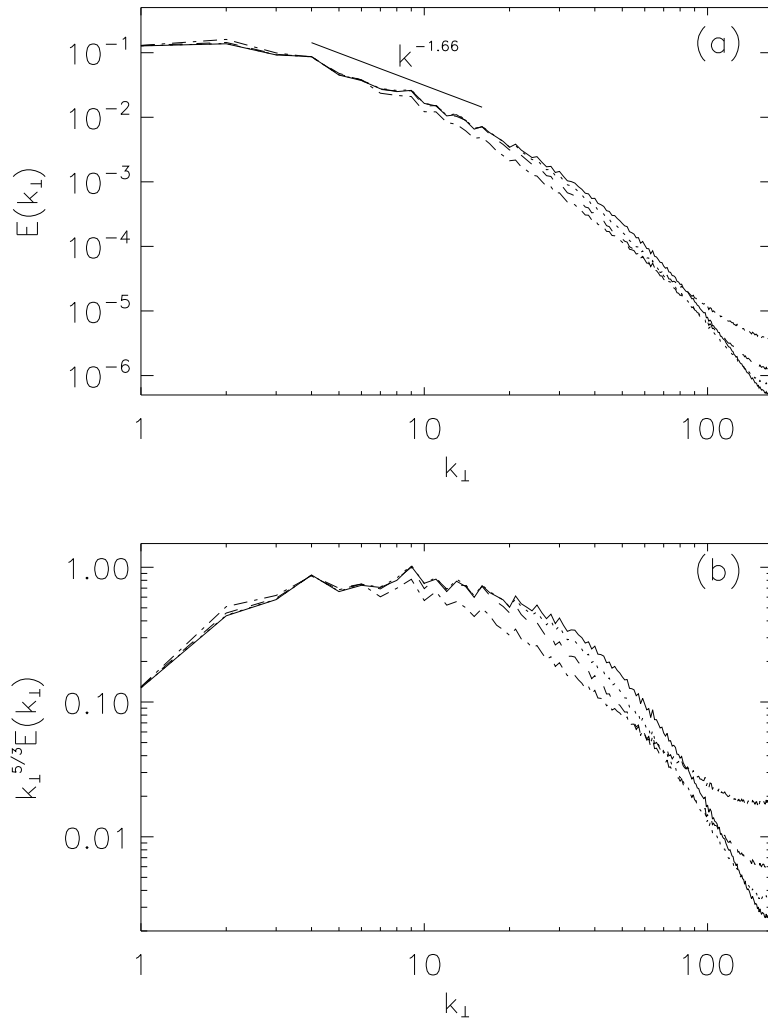


Figure 4.1: (a) Perpendicular energy spectrum for runs A (solid), B (dotted), C (dashed), and D (dash-dotted). Note how the spectrum becomes steeper in the HMHD simulations for wavenumbers larger than the inverse ion skin depth  $k_\epsilon$  (respectively 32, 16, and 8 for runs B, C, and D). The slope indicates Kolmogorov scaling as a reference. (b) Perpendicular energy spectrum compensated by  $k^{-5/3}$  for the same runs.

HMHD subrange of the form  $E(k) \sim k^{-7/3}$  [42, 16, 43] (such a spectrum has also been observed in the solar wind [44, 45, 17]). Run D has a HMHD subrange wide enough to compute structure functions and scaling exponents (from  $k_{\perp} = 1/\epsilon = 8$  to  $k_{\perp} \approx 20$ ), while runs B and C are intermediate between runs A and D and have two barely resolved subranges. However, these two intermediate runs will be useful to study trends in the behavior of the PDFs and of the structure functions as  $\epsilon$  is increased.

## 4.5 Structure functions and scaling exponents

We present here the results for the computation of the axisymmetric structure functions for the longitudinal component of the velocity and magnetic field for runs A, B, C, and D.

Figure 4.2 shows the structure functions for the magnetic field fluctuations up to sixth order for runs A and D. The structure functions show a range of scales with approximately power law scaling at intermediate scales, and at the smallest scales approach the  $\sim l^p$  scaling expected for a smooth field in the dissipative range. The velocity field structure functions (not shown) display a similar behavior, at the same range of scales. The inertial range identified in the energy spectrum  $E(k_{\perp})$  is consistent with the range of scales where  $S_p^u$  and  $S_p^b$  show an approximate power law behavior.

From the structure functions, the scaling exponents can be computed. Exponents for the velocity and the magnetic field up to sixth order in runs A and D are shown in Fig. 4.3. The range of scales used for the calculation corresponds to the subranges indicated before, with  $\lambda_{\perp} = 2\pi/k_{\perp}$ . For  $\epsilon = 0$  (run A) the deviation of the exponents  $\xi_p$  and  $\zeta_p$  from a straight line are an indication of intermittency and of multi-fractality. In the HMHD case ( $\epsilon = 1/8$ , run D), the exponents are closer to a straight line, indicating less intermittency. In fact, within error bars and up to  $p = 3$ , the data is consistent with  $\xi_p = \xi_2 p/2$  and  $\zeta_p = \zeta_2 p/2$ , and therefore with monoscaling as also observed for high-frequency magnetic fluctuations in the solar wind [17].

Run D (with  $\epsilon = 1/8$ ) has second scaling exponents  $\xi_2$  and  $\zeta_2$  which are larger than  $2/3$  (the value expected for Kolmogorov scaling), but which are smaller than  $4/3$  (the value expected if the spectrum is  $\sim k^{-7/3}$  [46, 47, 48]). This can be related to the fact that the total energy spectrum in Fig. 4.1 becomes steeper as the amplitude of the Hall effect is increased, but is still slightly shallower than  $-7/3$  for the run with  $\epsilon = 1/8$ . Also, note that the scaling of the velocity field and of the magnetic field can differ from that of the total energy, as is known to be the case in MHD [49, 50].

The deviation from strict scale invariance (linear scaling) in Fig. 4.3 can be quantified in terms of the intermittency exponents  $\mu^u = 2\xi_3 - \xi_6$  and  $\mu^b = 2\zeta_3 - \zeta_6$ . The larger these exponent, the more intermittent the fields. For run A these exponents are  $\mu^u = 0.57 \pm 0.07$  for the

## 4. Intermittency

---

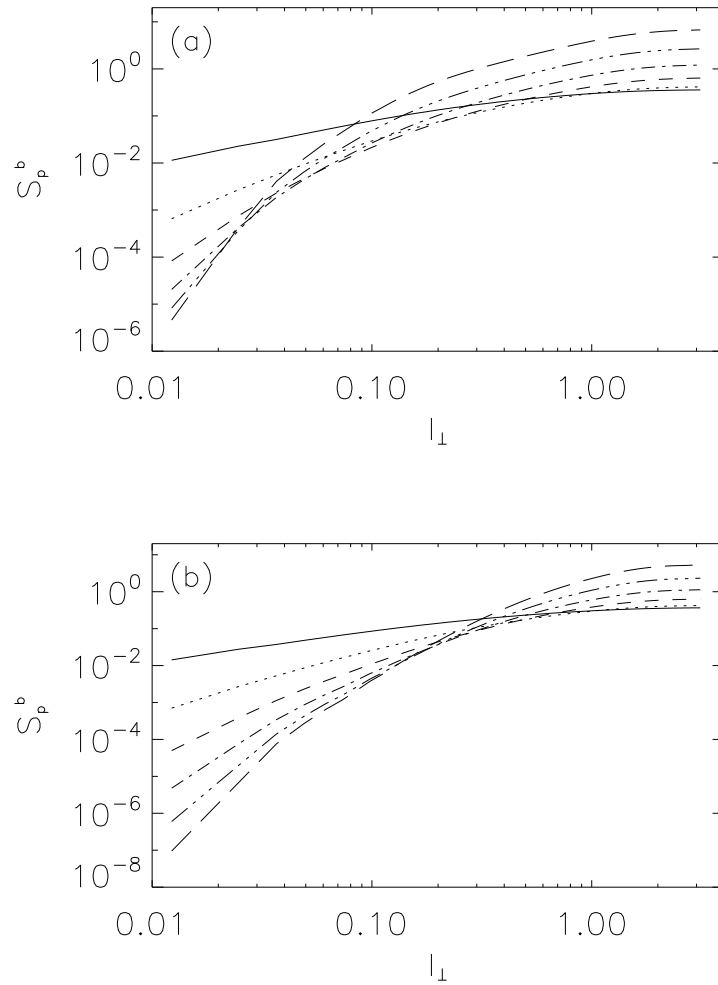


Figure 4.2: Axisymmetric structure functions for the longitudinal magnetic field up to six order for (a) run A ( $\epsilon = 0$ ), and (b) run D ( $\epsilon = 1/8$ ). The order of the structure function is indicated as follows:  $p = 1$  (solid), 2 (dotted), 3 (dashed), 4 (dash-dotted), 5 (dash-triple-dotted), and 6 (long dashes).

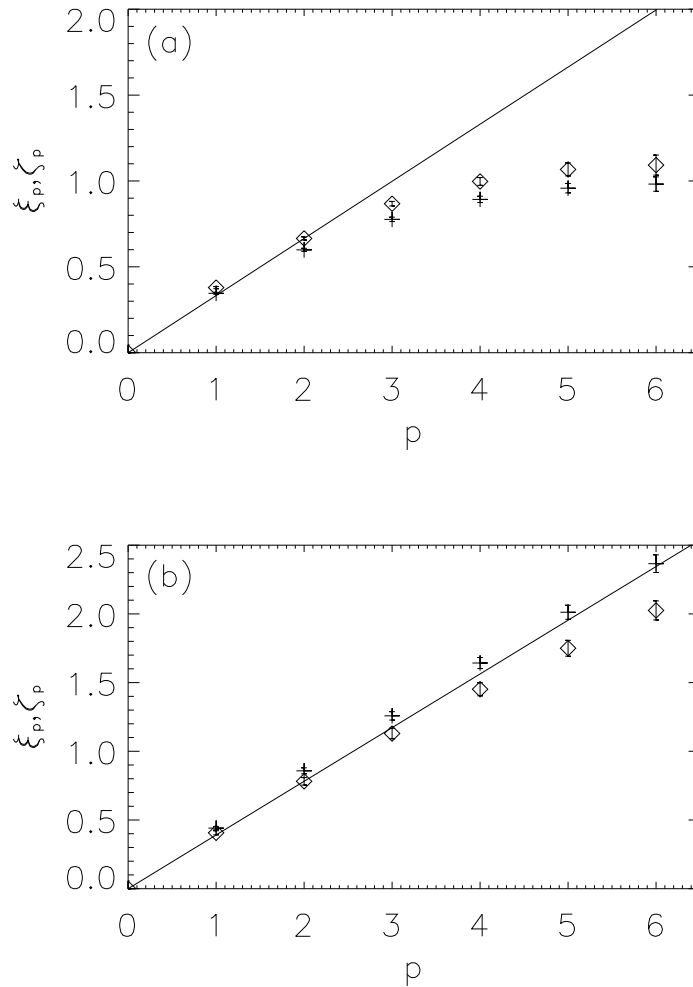


Figure 4.3: Scaling exponents (with error bars) as a function of the order  $p$  up to sixth order, for the velocity (crosses), and for the magnetic field (diamonds), (a) for run A ( $\epsilon = 0$ ), and (b) for run D ( $\epsilon = 1/8$ ). Linear scaling of the exponents with  $\zeta_2 p/2$  (corresponding to non-intermittent scaling with the second order exponent consistent with the scaling of the energy spectrum in Fig. 4.1) is indicated in both cases by the straight line.

## 4. Intermittency

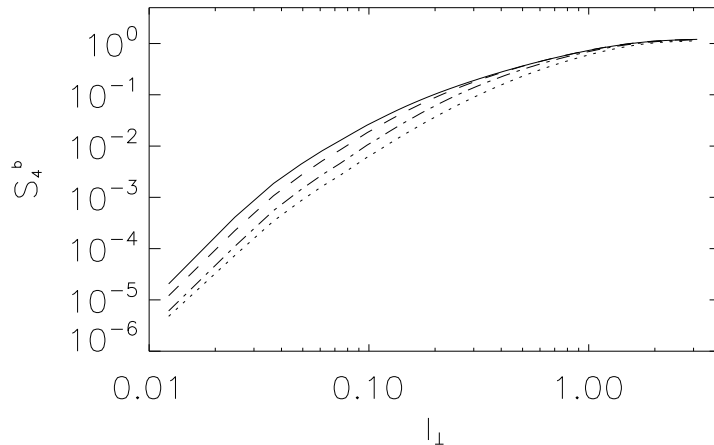


Figure 4.4: Fourth order structure function of longitudinal magnetic field increments for runs A ( $\epsilon = 0$ , solid line), B ( $\epsilon = 1/32$ , dashed), C ( $\epsilon = 1/16$ , dash-dotted), and D ( $\epsilon = 1/8$ , dotted).

velocity field, and  $\mu^b = 0.64 \pm 0.08$  for the magnetic field. It is interesting to point out that these values, that indicate that the magnetic field is more intermittent than the velocity field, are consistent with observations of large-scale fluctuations in the solar wind (see, e.g., [51]), and with numerical simulations of MHD turbulence at higher spatial resolution [50].

The intermittency exponents are substantially reduced for run D, with  $\mu^u = 0.15 \pm 0.12$  for the velocity field and  $\mu^b = 0.23 \pm 0.14$  for the magnetic field. This confirms that intermittency is substantially decreased in the presence of the Hall effect.

At the spatial resolution used in these runs, the lack of sufficient scale separation in the MHD and HMHD subranges for intermediate values of  $\epsilon$  does not allow the calculation of scaling exponents for runs B and C. However, the structure functions for these runs show a behavior intermediate between runs A and D, and consistent with the behavior of the spectrum in Fig. 4.1. In other words, as the Hall coefficient  $\epsilon$  is increased, the structure functions steepen at scales smaller than the ion-skin depth. As an example of this behavior, Fig. 4.4 shows the fourth order structure function for the magnetic field for runs A, B, C, and D. Note that runs B and C show a behavior consistent with the behavior of run A at large scales (scales larger than the ion-skin depth), and display a steeper slope (compatible with that found for run D) at smaller scales.

The results confirm that the presence of the Hall term steepens the scaling of the energy spectrum (and consistently, of the structure functions), and also show that the Hall effect reduces intermittency in the velocity and magnetic fields. The velocity and magnetic field scaling exponents approach a linear behavior characteristic of a self-similar (non-intermittent) flows. In

## 4.5. Structure functions and scaling exponents

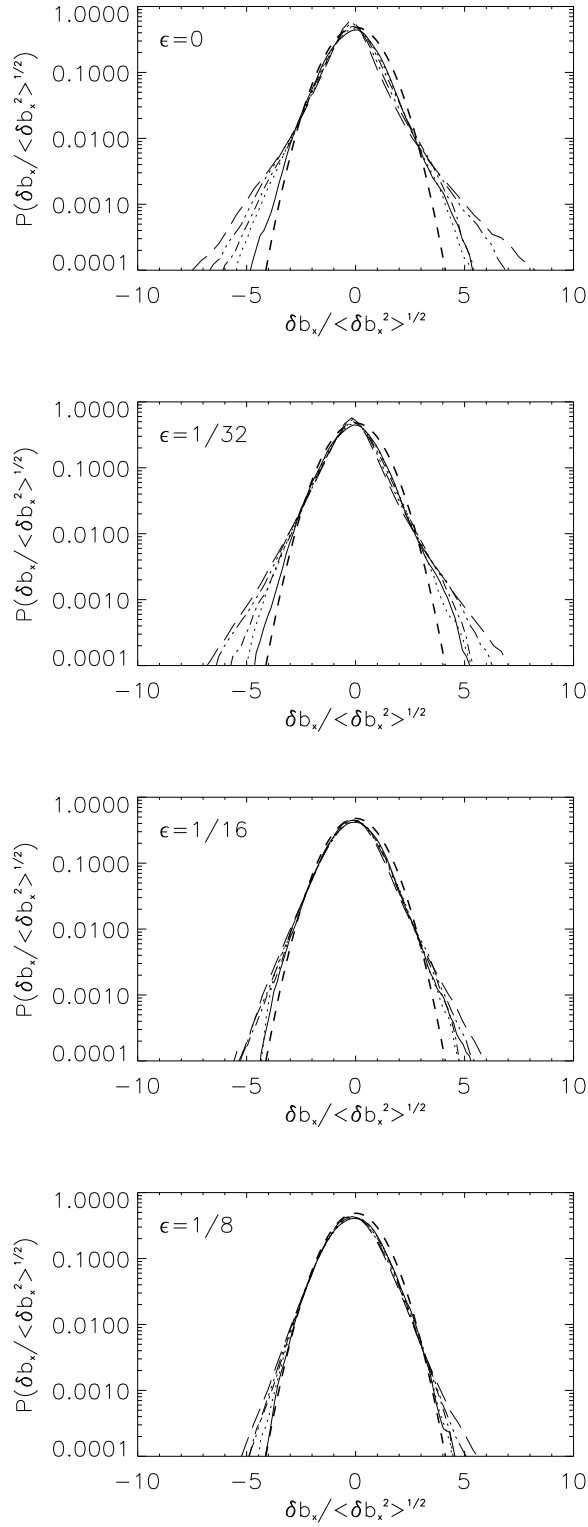


Figure 4.5: PDFs for magnetic field increments, for  $l = 1.6$  (solid),  $0.8$  (dotted),  $0.4$  (dash-dotted),  $0.2$  (dash-triple-dotted), and  $0.1$  (long dashes), and for runs A, B, C, and D from top to bottom, respectively. In all the figures, a dashed curve indicates a Gaussian PDF with unit variance.

## 4. Intermittency

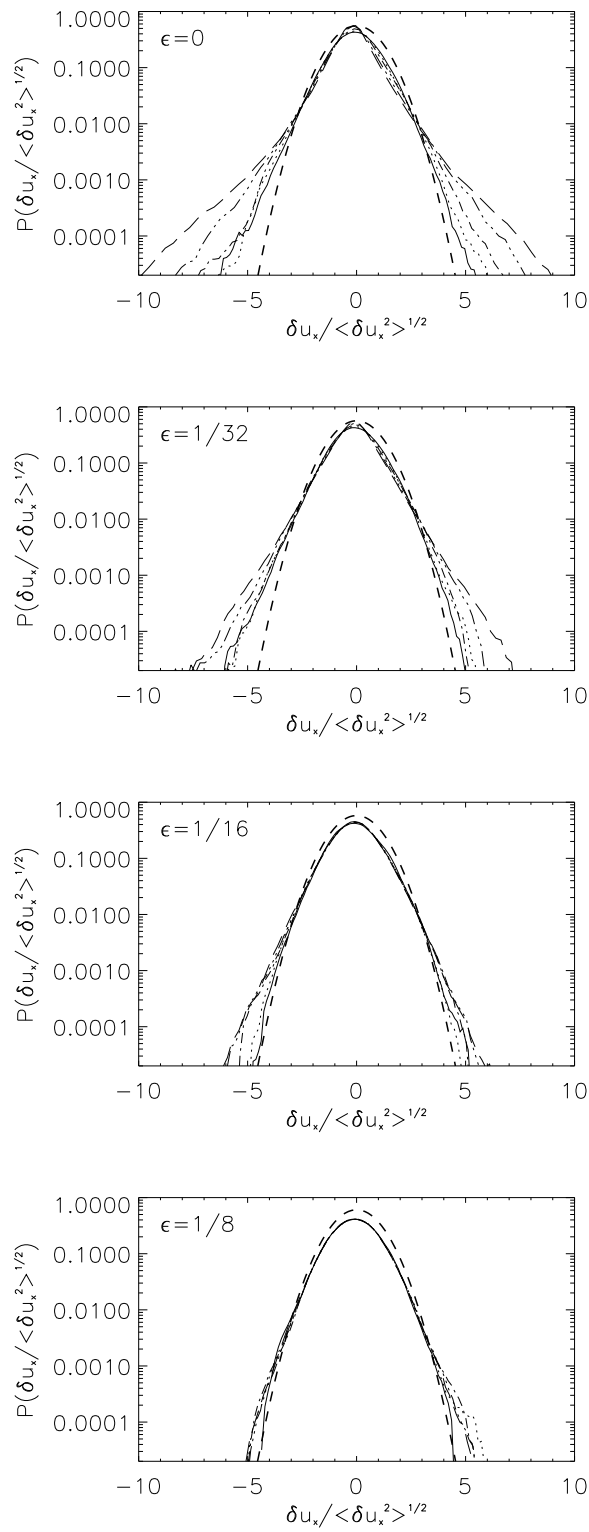


Figure 4.6: PDFs for velocity field increments, for  $l = 1.6$  (solid),  $0.8$  (dotted),  $0.4$  (dash-dotted),  $0.2$  (dash-triple-dotted), and  $0.1$  (long dashes), and for runs A, B, C, and D from top to bottom, respectively. In all the figures, a dashed curve indicates a Gaussian PDF with unit variance.

Table 4.1: Skewness ( $S$ ) and kurtosis ( $K$ ) for the  $x$ -derivatives of  $b_x$  and  $u_x$ , for all runs with spatial resolution  $512^2 \times 32$  and with different amplitudes of the Hall effect  $\epsilon$ .  $S(\partial_x b_x)$  and  $K(\partial_x b_x)$  are, respectively, the skewness and kurtosis of the magnetic field spatial derivatives, while  $S(\partial_x u_x)$  and  $K(\partial_x u_x)$  are the corresponding quantities for the velocity field derivatives.

Quantity	$\epsilon = 0$	$\epsilon = 1/32$	$\epsilon = 1/16$	$\epsilon = 1/8$
$S(\partial_x u_x)$	-0.18	-0.013	-0.01	-0.001
$K(\partial_x u_x)$	19	8.1	5	4.9
$S(\partial_x b_x)$	0.36	0.17	0.11	0.07
$K(\partial_x b_x)$	26	15.7	6.6	5.8

the next section, this result is confirmed by an analysis of PDFs of velocity and magnetic field increments and spatial derivatives.

## 4.6 Probability density functions

We now consider PDFs for longitudinal increments of the  $x$ -component of the velocity and magnetic fields. As already mentioned, the PDFs will be presented normalized by their variance, and together with a Gaussian distribution with unit variance as a reference. Deviations from Gaussianity, or increase of the deviations from Gaussianity as smaller increments are considered, are a signature of intermittency.

Figure 4.5 shows the PDFs of the magnetic field increments for four different spatial increments, namely  $l = 1.6, 0.8, 0.4, 0.2$  and  $0.1$ , for runs A, B, C, and D. For all runs, the PDFs of magnetic field increments are close to Gaussian for  $l = 1.6$ , while for smaller spatial increments non-Gaussian tails and asymmetry develop. This is a common feature for many turbulent flows, with large scales close to Gaussian statistics and smaller scales developing deviations from Gaussianity with strong tails (i.e., with extreme gradients more probable than what can be expected from a normal distribution). As a reference, the integral scale in all runs (the scale with the energy containing eddies) is close to the size of the domain,  $L \approx 2\pi$ , while the dissipative scale is  $L_\eta \approx 0.05$ . Increments with  $l = 1.6$  are close to the flow integral scale, increments with  $l = 0.8$  or  $0.4$  are in the inertial range, while  $l = 0.1$  is close to the dissipation length scale.

Although all runs develop non-Gaussian tails, when comparing the PDFs of the four runs with different values of  $\epsilon$ , it is clear that the amplitude of these tails is drastically reduced as the value of  $\epsilon$  is increased. Moreover, for the largest value of  $\epsilon$  considered, we cannot identify a clear increase in the amplitude of the tails as we look at smaller increments. This tendency (which

## 4. Intermittency

---

is monotonic with increasing  $\epsilon$ ) of the PDFs of different spatial increments to collapse into a single curve, with weaker tails than in the MHD case, is an indication of reduced intermittency and expected for scale-invariant flows.

Figure 4.6 shows the same PDFs for increments of the velocity field. Again, the PDFs are close to Gaussian for the largest increment in the four runs, and non-Gaussian tails develop with increasing amplitude for smaller increments. In this case, for  $\epsilon = 1/8$  all the PDFs seem to collapse into the Gaussian, and the tails are weaker than for the magnetic field. This is consistent with the previous observation, using the intermittency coefficients  $\mu^u$  and  $\mu^b$ , that the magnetic field is more intermittent than the velocity field, and that both fields are less intermittent in HMHD than in MHD.

To quantify the deviations from a Gaussian distribution in each run, we calculated the skewness and the kurtosis of the  $x$ -derivatives of the  $x$ -components of the velocity and magnetic fields. Note these quantities correspond respectively to the third- and fourth-moments of the PDFs in Figs. 4.5 and 4.6 in the limit of vanishing spatial increment. The skewness and kurtosis of a function  $f$  are defined as  $S(f) = \langle f^3 \rangle / \langle f^2 \rangle^{3/2}$  and  $K(f) = \langle f^4 \rangle / \langle f^2 \rangle^2$  respectively, where  $f$  can be, e.g., some component of the velocity (or magnetic) field gradient. The resulting values are listed in Table 4.1. In accordance with what can be expected from a visual inspection of Figs. 4.5 and 4.6, the skewness of  $\partial_x u_x$  and  $\partial_x b_x$  is reduced to almost zero for  $\epsilon = 1/8$ , which indicates a substantial reduction in the asymmetry of the PDF. The kurtosis of  $\partial_x u_x$  and  $\partial_x b_x$  also decreases with increasing  $\epsilon$ , which indicates a smoothing in the peakedness of the PDFs and a decrease in the intensity of the tails.

### 4.7 Effect of resolution

Recently, it was stressed the need of using well resolved numerical simulations to quantify high order statistics and intermittency in MHD [52]. In particular, it has been claimed that if the flow is not properly resolved, a partial thermalization of the small scales may result in artificial Gaussian statistics and an artificial decrease of the intermittency. Considering this, in this section we present results for simulations with the same parameters as in runs A and D, but with larger parallel or perpendicular spatial resolution. We consider two runs with  $768^2 \times 32$  grid points, namely runs A2 and D2, and two runs with  $512^2 \times 64$  grid points, runs A3 and D3. Runs A2 and A3 have the same parameters and initial conditions as run A, while runs D2 and D3 are the same as run D except for the change in resolution.

We computed structure functions, scaling exponents, and PDFs for runs A2, D2, A3 and D3 and compared the results with those found for runs A and D. In all cases, the results were consistent within error bars. As an illustration, in Fig. 4.7 we show the velocity field and mag-

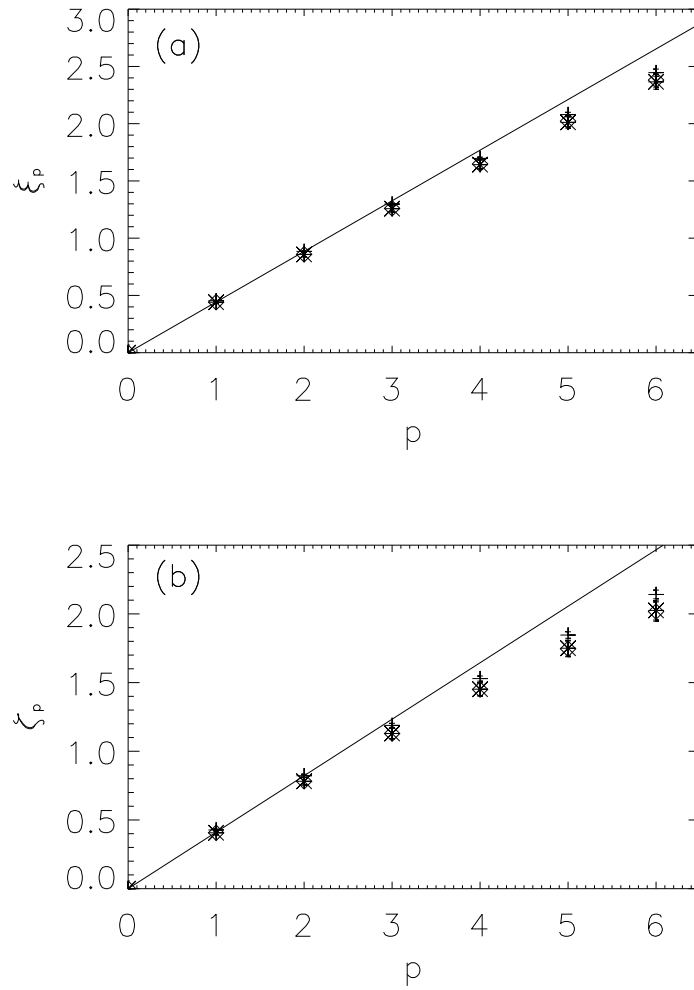


Figure 4.7: (a) Velocity field scaling exponents (with error bars) as a function of the order  $p$  up to sixth order, for runs D (stars), D2 (crosses), and D3 (diamonds) all with  $\epsilon = 1/8$ . Linear scaling of the exponents is indicated as a reference. (b) Same for the magnetic field scaling exponents.

## 4. Intermittency

---

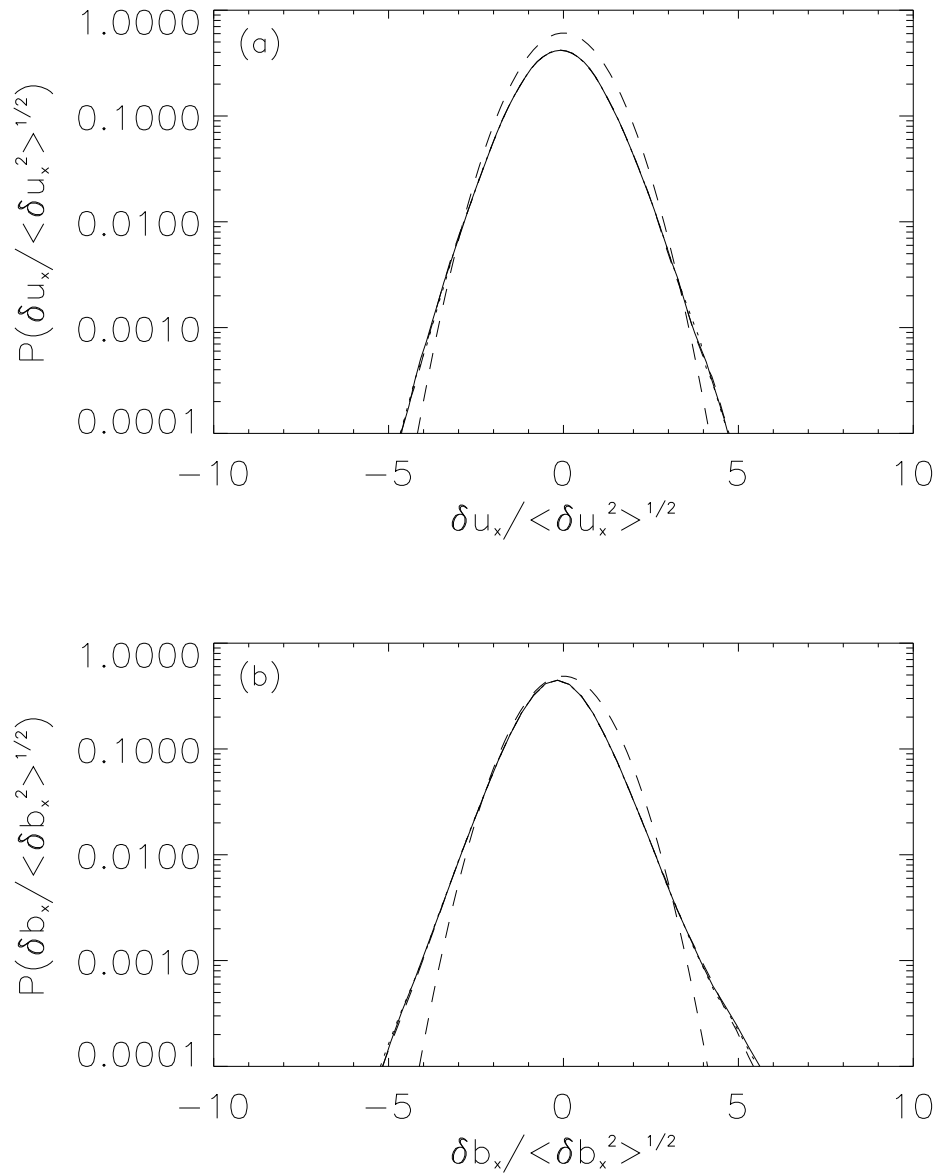


Figure 4.8: (a) PDFs of velocity field increments for  $l = 0.1$  and  $\epsilon = 1/8$ , for runs D (solid line), D2 (dotted), and D3 (dashed-dotted). The three PDFs are practically indistinguishable. The dashed line shows a Gaussian distribution as a reference. (b) Same for magnetic field increments.

netic field scaling exponents for runs D, D2, and D3 (all with  $\epsilon = 1/8$ , and respectively with  $512^2 \times 32$ ,  $768^2 \times 32$ , and  $512^2 \times 64$  grid points). Increasing the parallel or perpendicular resolution does not change the scaling exponents, nor does it change the fact that the exponents are close to the straight line and less intermittent than in the MHD case.

In run A2 the intermittency exponents are  $\mu^u = 0.52 \pm 0.08$  and  $\mu^b = 0.70 \pm 0.07$ , while in run A3 we obtain  $\mu^u = 0.57 \pm 0.07$  and  $\mu^b = 0.64 \pm 0.08$ , consistent within error bars with the values found in run A. In run D2 the intermittency exponents are  $\mu^u = 0.15 \pm 0.04$  and  $\mu^b = 0.24 \pm 0.06$ , while in run D3 the exponents are  $\mu^u = 0.14 \pm 0.12$  and  $\mu^b = 0.24 \pm 0.14$ , also consistent with the values obtained in run D.

Figure 4.8 shows the PDFs of velocity and magnetic field increments in runs D, D2 and D3, for a spatial increment  $l = 0.1$ . The PDFs are almost indistinguishable. Similar results were obtained for runs A, A2 and A3. When computing the PDFs of spatial derivatives of the fields, we obtained  $S(\partial_x u_x) = -0.19$ ,  $S(\partial_x b_x) = 0.41$ ,  $K(\partial_x u_x) = 18$ , and  $K(\partial_x b_x) = 26$  for run A2, and  $S(\partial_x u_x) = -0.18$ ,  $S(\partial_x b_x) = 0.36$ ,  $K(\partial_x u_x) = 19$ , and  $K(\partial_x b_x) = 27$  for run A3. For the runs with Hall effect, we found  $S(\partial_x u_x) = -0.001$ ,  $S(\partial_x b_x) = 0.08$ ,  $K(\partial_x u_x) = 8.4$ , and  $K(\partial_x b_x) = 6.5$  for run D2, and  $S(\partial_x u_x) = -0.001$ ,  $S(\partial_x b_x) = 0.07$ ,  $K(\partial_x u_x) = 5.9$ , and  $K(\partial_x b_x) = 5.8$  for run D3. These values should be compared with the values in Table 4.1 for runs A and D at lower resolution.

Wan et al. [52] argue that for an MHD simulation to be well resolved, the kurtosis of the current should remain independent of the spatial resolution. In our MHD and HMHD runs that condition is fulfilled, at least up to the level of statistical fluctuations that can be expected when comparing two simulations of a turbulent flow. To verify this, we computed the skewness and kurtosis of the component of the current density parallel to the external magnetic field, i.e.,  $S(j_z)$  and  $K(j_z)$ . In the MHD simulations ( $\epsilon = 0$ ), we obtained  $S(j_z) = 0,70$  and  $K(j_z) = 21$  in the simulation with  $512^2 \times 32$  grid points,  $S(j_z) = 0,71$  and  $K(j_z) = 22$  in the simulation with  $768^2 \times 32$  grid points, and  $S(j_z) = -0,70$  and  $K(j_z) = 21$  in the simulation with  $512^2 \times 64$  grid points. In the HMHD simulations with  $\epsilon = 1/8$ , we obtained  $S(j_z) = -0,02$  and  $K(j_z) = 4.5$  in the simulation with  $512^2 \times 32$  grid points,  $S(j_z) = -0,01$  and  $K(j_z) = 4.8$  in the simulation with  $768^2 \times 32$  grid points, and  $S(j_z) = -0,02$  and  $K(j_z) = 4.5$  in the simulation with  $512^2 \times 64$  grid points.

Although there is a small increase in  $S(j_z)$  and  $K(j_z)$  as the perpendicular resolution is increased in both the MHD and HMHD runs, the increase is smaller than 10% in most cases. Increasing the parallel resolution seems to have no significative effect. As a result, we conclude that the simulations are well resolved even with the more stringent criteria of Wan et al. [52]. Moreover, the reduction of the intermittency in presence of the Hall term is also confirmed by the skewness and kurtosis of the current at both spatial resolutions.

## 4. Intermittency

---

As a result, we conclude that increasing resolution has no significant effect on the results we reported in the previous section, and that the decrease in the intermittency of the flow presented above has its source in the Hall effect and not in a numerical artifact when the flow is not properly resolved.

### 4.8 Conclusions

We presented a study of intermittency in the velocity and magnetic field fluctuations of compressible Hall-magnetohydrodynamic turbulence with an external guide field. Unlike previous works, we were not interested in the characterization of geometrical properties or in the size of individual structures in the flow (that will be the topic in the next chapter), but rather interested in their overall statistical properties.

In the magnetohydrodynamic limit we recovered results found in previous studies, with the magnetic field being more intermittent than the velocity field. However, in the presence of the Hall effect, we found field fluctuations at scales smaller than the ion skin depth to be substantially less intermittent, with close to monofractal scaling.

As the intensity of the Hall effect was increased in the simulations (i.e., the ion skin depth was made larger in units of the box size), we found both the total energy spectrum and the structure functions to develop a steeper scaling in a wider subinertial range, for all scales smaller than the ion skin depth. The behavior of the scaling exponents for both the velocity and the magnetic field up to sixth order becomes closer to monofractal as the Hall effect is increased, and the intermittency exponent decreases accordingly.

In agreement with these results, the probability density functions of longitudinal velocity and magnetic field increments have weaker non-Gaussian tails and less asymmetry at scales smaller than the ion skin depth. For velocity and magnetic field gradients, the skewness and kurtosis also decrease as the Hall effect is increased.

The results were obtained for simulations with spatial resolution of  $512^2 \times 32$  grid points, and verified in simulations at larger spatial resolution, with  $768^2 \times 32$  grid points and with  $512^2 \times 64$  grid points. As a result, we can safely conclude that increasing the resolution has no effect on the results, and that the decrease in the intermittency of the flow has its source in the Hall effect.

It is interesting that although a decrease in the intermittency has been observed in high-frequency magnetic field fluctuations in the solar wind [16, 17, 53], the observations also show PDFs with strong non-Gaussian tails. These non-Gaussian tails are absent in our simulations, and considering the limitations of the HMHD model we are led to conjecture that their origin in the solar wind lies in other kinetic effects that are not captured by our model (see, e.g., [53, 54]).

# Bibliography

- [1] P. Rodriguez Imazio, **L. N. Martin**, and P. D. Mininni, *Phys. Plasma*, **20**, 052506 (2013). [65](#)
- [2] J. Birn and M. Hesse, *J. Geophys. Res.* **106**, 3737 (2001). [66](#)
- [3] M. Shay, J. F. Drake, B. N. Rogers, and R. E. Denton, *J. Geophys. Res.* **106**, 3759 (2001). [66](#)
- [4] Y. Ren, M. Yamada, S. Gerhardt, H. Ji, R. Kulsrud, and A. Kuritsyn, *Phys. Rev. Lett.* **95**, 55003 (2005). [66](#)
- [5] P. Dmitruk and W. H. Matthaeus, *Phys. Plasmas* **13**, 042307 (2006). [66](#)
- [6] L. N. Martin, P. Dmitruk, and D. O. Gómez, *Phys. Plasmas*, **19**, 052305 (2012). [66](#)
- [7] S. Donato, S. Servidio, P. Dmitruk, V. Carbone, M. A. Shay, and P. A. Cassak, *Phys. Plasmas*, **19**, 092307 (2012). [66](#)
- [8] S. Servidio, W. H. Matthaeus, M. A. Shay, P. A. Cassak and P. Dmitruk, *Phys. Rev. Lett.* **102**, 115003 (2009). [66](#)
- [9] M. Yamada, Y. Ren, H. Ji, J. Breslau, S. Gerhardt, R. Kulsrud, and A. Kuritsyn, *Phys. Plasmas*, **13**, 052119 (2006). [66](#)
- [10] P. D. Mininni, D. O. Gómez, and S. M. Mahajan, *Astrophys. J.* **567**, L81 (2002). [66](#)
- [11] P. D. Mininni, D. O. Gómez, and S. M. Mahajan, *Astrophys. J.* **584**, 1120 (2003). [66](#)
- [12] P. D. Mininni, D. O. Gómez, and S. M. Mahajan, *Astrophys. J.* **619**, 1019 (2005). [66](#)
- [13] P. D. Mininni, A. Alexakis and A. Pouquet, *J. Plasma Phys.* **73**, 377 (2007). [66](#)
- [14] D. O. Gómez, P. D. Mininni, and P. Dmitruk, *Phys. Rev. E* **82**, 036406 (2010). [66](#), [69](#)

## BIBLIOGRAPHY

---

- [15] O. Alexandrova, V. Carbone, P. Veltri, and L. Sorriso-Valvo, *Pl. and Space Sc.* **55**, 2224 (2007). [66](#)
- [16] O. Alexandrova, V. Carbone, P. Veltri, and L. Sorriso-Valvo, *Astrophys. J.* **674**, 1153 (2008). [66](#), [71](#), [82](#)
- [17] K. H. Kiyani, S. C. Chapman, Yu. V. Khotyaintsev, and M. W. Dunlop and F. Sahraoui, *Phys. Rev. Lett.* **103**, 075006 (2010). [66](#), [71](#), [82](#)
- [18] H. R. Strauss, *Phys. Fluids*, **19**, 134 (1976). [66](#)
- [19] D. Montgomery, *Phys. Scripta*, **T2**, 83 (1982). [66](#)
- [20] D. O. Gómez, S. M. Mahajan, and P. Dmitruk, *Phys. Plasmas*, **15**, 102303 (2008). [66](#)
- [21] L. N. Martin, P. Dmitruk, and D. O. Gomez, *Phys. Plasma* **17**, 112304 (2010). [66](#)
- [22] J. Cho and A. Lazarian, *Astrophys. J.* **701**, 236 (2009) [66](#)
- [23] **L. N. Martin** and P. D. Mininni, *Phys. Rev. E* **81**, 016310 (2010). [67](#), [68](#)
- [24] P. D. Mininni and A. Pouquet, *Phys. Fluids*, **22**, 035106 (2010). [67](#), [68](#)
- [25] P. Rodriguez Imazio and P. D. Mininni, *Phys. Rev. E* **83**, 066309 (2011). [67](#), [68](#)
- [26] I. Arad, B. Dhruva, S. Kurien, V. S. L'vov, I. Procaccia, and K. R. Sreenivasan, *Phys. Rev. Lett.* **81**, 5330 (1998). [68](#)
- [27] L. Biferale and I. Procaccia, *Phys. Rep.* **414**, 43 (2005). [68](#)
- [28] R. Benzi, S. Ciliberto, C. Baudet, G. Ruiz Chavarria, and R. Tripicciono, *Europhys. Lett.* **24**, 275 (1993). [68](#)
- [29] R. Benzi S. Ciliberto R. Tripicciono C. Baudet, F. Massaioli, and S. Succi, *Phys. Rev. E* **48**, R29 (1993). [68](#)
- [30] P. Dmitruk, D. O. Gómez, and W. H. Matthaeus, *Phys. Plasmas* **10**, 3584 (2003). [69](#)
- [31] P. D. Mininni and A. Pouquet, *Phys. Rev. Lett.* **99**, 254502 (2007). [69](#)
- [32] E. Lee, M. E. Brachet, A. Pouquet, and P. D. Mininni, *Phys. Rev. E* **81**, 016318 (2009). [69](#)
- [33] J. C. Perez, J. Mason, S. Boldyrev, and F. Cattaneo, *Phys. Rev. X* **2**, 041005 (2012). [69](#)
- [34] S. Galtier, S. V. Nazarenko, A. C. Newell, and A. Pouquet, *J. Plasma Phys.* **63**, 447 (2000). [69](#)

- [35] S. Galtier and A. Bhattacharjee, *Phys. Plasmas* **10**, 3065 (2003). [69](#)
- [36] S. Nazarenko, “Wave turbulence” (Springer, Berlin, 2011). [69](#)
- [37] A. Verdini and R. Grappin, *Phys. Rev. Lett.* **109**, 025004 (2012). [69](#)
- [38] S. Boldyrev and J. C. Perez, *Astrophys. J.* **758**, L44 (2012). [69](#)
- [39] P. Dmitruk and W. H. Matthaeus, *Phys. Plasmas* **16**, 062304 (2009) [69](#)
- [40] S. Ghosh, E. Siregar, D. A. Roberts, and M. L. Goldstein, *J. Geophys. Res.* **101**, 2493 (1996). [69](#)
- [41] S. Galtier and E. Buchlin, *Astrophys. J.* **656**, 560 (2007). [69](#)
- [42] S. Galtier, *Phys. Rev. E* **77**, 015302 (2008). [71](#)
- [43] G. G. Howes, J. M. TenBarge, W. Dorland, E. Quataert, A. A. Schekochihin, R. Numata, and T. Tatsuno, *Phys. Rev. Lett.* **107**, 035004 (2011). [71](#)
- [44] O. Alexandrova, J. Saur, C. Lacombe, A. Mangeney, J. Mitchell, S. J. Schwartz, and P. Robert, *Phys. Rev. Lett.* **103**, 165003 (2009). [71](#)
- [45] F. Sahraoui, M. L. Goldstein, P. Robert, and Yu. V. Khotyaintsev, *Phys. Rev. Lett.* **102**, 231102 (2009). [71](#)
- [46] E. Camporeale and D. Burgess, *Astrophys. J.* **730**, 114 (2011). [71](#)
- [47] R. Meyrand and S. Galtier, *Phys. Rev. Lett.* **109**, 194501 (2012). [71](#)
- [48] M. Wan, W. H. Matthaeus, H. Karimabadi, V. Roytershteyn, M. Shay, P. Wu, W. Daughton, B. Loring, and S. C. Chapman, *Phys. Rev. Lett.* **109**, 195001 (2012). [71](#)
- [49] P. D. Mininni and A. Pouquet, *Phys. Rev. Lett.* **99**, 254502 (2007). [71](#)
- [50] P. D. Mininni and A. Pouquet, *Phys. Rev. E.* **80**, 025401(R) (2009). [71](#), [74](#)
- [51] J. J. Podesta, D. A. Roberts, and M. L. Goldstein, *Astrophys. J.* **664**, 543 (2007). [74](#)
- [52] M. Wan, S. Oughton, S. Servidio and W.H. Matthaeus, *Phys. Plasmas* **17**, 082308 (2010). [78](#), [81](#)
- [53] K. H. Kiyani, S. C. Chapman, F. Sahraoui, B. Hnat, O. Fauvarque, and Yu. V. Khotyaintsev, *Astrophys. J.* **763**, 10 (2013). [82](#)
- [54] D. Perrone, F. Valentini, S. Servidio, S. Dalena, and P. Veltri, *Astrophys. J.* **762**, 99 (2013). [82](#)



# Chapter 5

## Statistical properties

[1]

### Contents

---

5.1	A brief review . . . . .	87
5.2	Set up . . . . .	89
5.3	Qualitative approach . . . . .	89
5.4	The signed Measure and the cancellation exponent . . . . .	89
5.5	Cancellation analysis in turbulent plasmas . . . . .	93
5.6	Conclusions . . . . .	101

---

Finally we present a signed measure analysis. Signed measure analysis allows to characterize the scaling behavior of the sign-oscillating flow structures and their geometrical properties (fractal dimensions of structures). Results show that as the Hall term is increased the fractal dimension of the current and vorticity sheets decreases. This observation, together with the previous analysis, provides a comprehensive description of the effect of the Hall term on the formation of structures. Finally we confirmed (now with quantitative evidence) the existence of two main processes, namely the widening and unraveling of the sheets.

### 5.1 A brief review

As we explained in the previous chapter, different studies have provided conflicting results regarding the effect of the Hall term in the generation of structures in magnetohydrodynamics turbulence, so the debate is still open. In particular, some numerical simulations have indicated that current sheets in presence of Hall effect become wider than in MHD (see, e.g., [2]), while, on the contrary, other studies have shown the presence of thinner structures [3].

## 5. Statistical properties

---

To this point we have made a very broad and comprehensive analysis about the Hall effect in a strong external magnetic field. In chapter 2 the effect of the Hall term has been analyzed in terms of global magnitudes (*e.g.*, the mean square current density  $\langle j^2 \rangle$  and vorticity  $\langle \omega^2 \rangle$ ), characteristic times of the flow, energy cascade and qualitative features of the flow structures (current sheets) [2]. We found that the Hall term turned out to affect mostly the scales between the Hall scale and the dissipation scale. This produces an enhancement of the energy transfer in such scale range, and therefore the accumulation of energy decreases. This corresponds to an effective shift of the dissipation scale toward smaller scales. This was estimated by observing an increasingly sharp steepening of the energy spectrum in the Hall range, when the separation between the Hall scale and the dissipation scale is larger. This suggests the possible generation of smaller scales when the Hall effect increases. Qualitative observation of current sheets showed that they become wider as the Hall effect increases; however, within them, smaller structures seem to emerge. The main objective of this chapter is to perform a quantification about this.

In chapter 3 [4], a detailed study of intermittency has been performed. In presence of Hall effect, field fluctuations at scales smaller than the ion skin depth become substantially less intermittent, with scaling properties close to self similarity. A quantitative measure of the intermittency is crucial to understand the topological distribution of dissipation in magneto-fluids and plasmas, and it can also provide constraints for theoretical study of phenomena such as magnetic energy dissipation and reconnection. But this, by itself, does not answer the question about the thickness of current sheets. The founded decrease in the intermittency can mean one of two things, HMHD small scale structures are thicker than in MHD, or, on the contrary, they are thinner but more space filling, causing intermittency decrease in one way or another. The main purpose of the present chapter is to quantitatively evaluate the characteristics of the small scale structures and their features with respect to the magnitude of the Hall effect. It is very important to note that numerical simulations quality was tested according to the stringent criteria of Wan et al. [5], because it is necessary a very high level of convergence for this type of analysis.

In order to gain more insight on the actual effect of the Hall term on flow structures, here we study the geometrical properties of the vorticity and current field, using an explicit and quantitative approach. Our study focuses on the estimation of the cancellation exponents, as introduced by Ott et al. [6]. Such exponents provide a simple characterization of the flows, and are phenomenologically related with the fractal dimension of the typical structure [7].

## 5.2 Set up

Simulations analyzed in this chapter are the same to those described in previous chapters. Here we review the important points. Simulations have  $512^2$  grid points in the plane perpendicular to the external magnetic field and 32 grid points in the parallel direction.  $B_0 = 8$ , the kinetic and magnetic Reynolds numbers are defined respectively as  $R = 1/\nu$ ,  $R_m = 1/\eta$ , based on unit initial r.m.s. velocity fluctuation, unit length, and dimensionless values for the viscosity and diffusivity. For all the runs, we used  $R = R_m = 1600$  (i.e.,  $\nu = 1/1600$ ,  $\eta = 1/1600$ ). We also considered a Mach number  $M_S = 1/4$ , and an Alfvén Mach number  $M_A = 1$ .

Again the same four values of the Hall parameter were considered, namely  $\varepsilon = 0$  (MHD case),  $1/32$ ,  $1/16$ , and  $1/8$ . In the same way as in the previous chapter, data from simulations with such values of  $\varepsilon$  will be labeled as Run A, B, C and D, respectively. As the numerical domain used has size  $2\pi$  (see above), these values correspond respectively to ion skin depths with associated wave numbers  $k_\varepsilon = \infty, 32, 16$ , and  $8$ , and to scales of  $\rho_{ii} = 0, 0.03, 0.06$  and  $0.4$ .

## 5.3 Qualitative approach

Figures 5.1 and 5.2 show some example of current components. Left hand panels show, for each Run, two dimensional cuts in the perpendicular plane of one perpendicular component  $j_x$  (Figure 5.1) and of the parallel component  $j_z$  (Figure 5.2), for one snapshot of the simulation in the statistically steady state ( $t = 4.5$ , when the turbulence was fully developed; see figure 3.1). On the right panels, the same field is plotted with an arbitrary tilt angle, in order to highlight the chaotic alternation of positive and negative fluctuations of the fields. From visual inspection, it appears evident that structures become more fragmented as  $\varepsilon$  increases.

Figure 5.3 shows the total energy spectra  $E(k)$ , integrated on spheres of radius  $k$ , for the four runs. The ion skin depth scale is also indicated. The large scale part of the spectra is compatible with the typical Kolmogorov scaling  $\alpha = 5/3$ . For the largest  $\varepsilon$  (Run D), a secondary power-law region emerges at scales smaller than the ion skin depth, compatible with the typical spectral index for reduced Hall MHD,  $\alpha = 7/3$ .

## 5.4 The signed Measure and the cancellation exponent

As discussed before, turbulent plasmas are often characterized by scale dependent formation of energetic and localized structures. These represents regions where dissipation of energy is enhanced, and are believed to be responsible for the anomalous scaling of the structure functions. Intermittency and multifractality are strictly related to their presence [8]. Structures such as current sheets and vorticity filaments are continuously observed in numerical simulations

## 5. Statistical properties

---

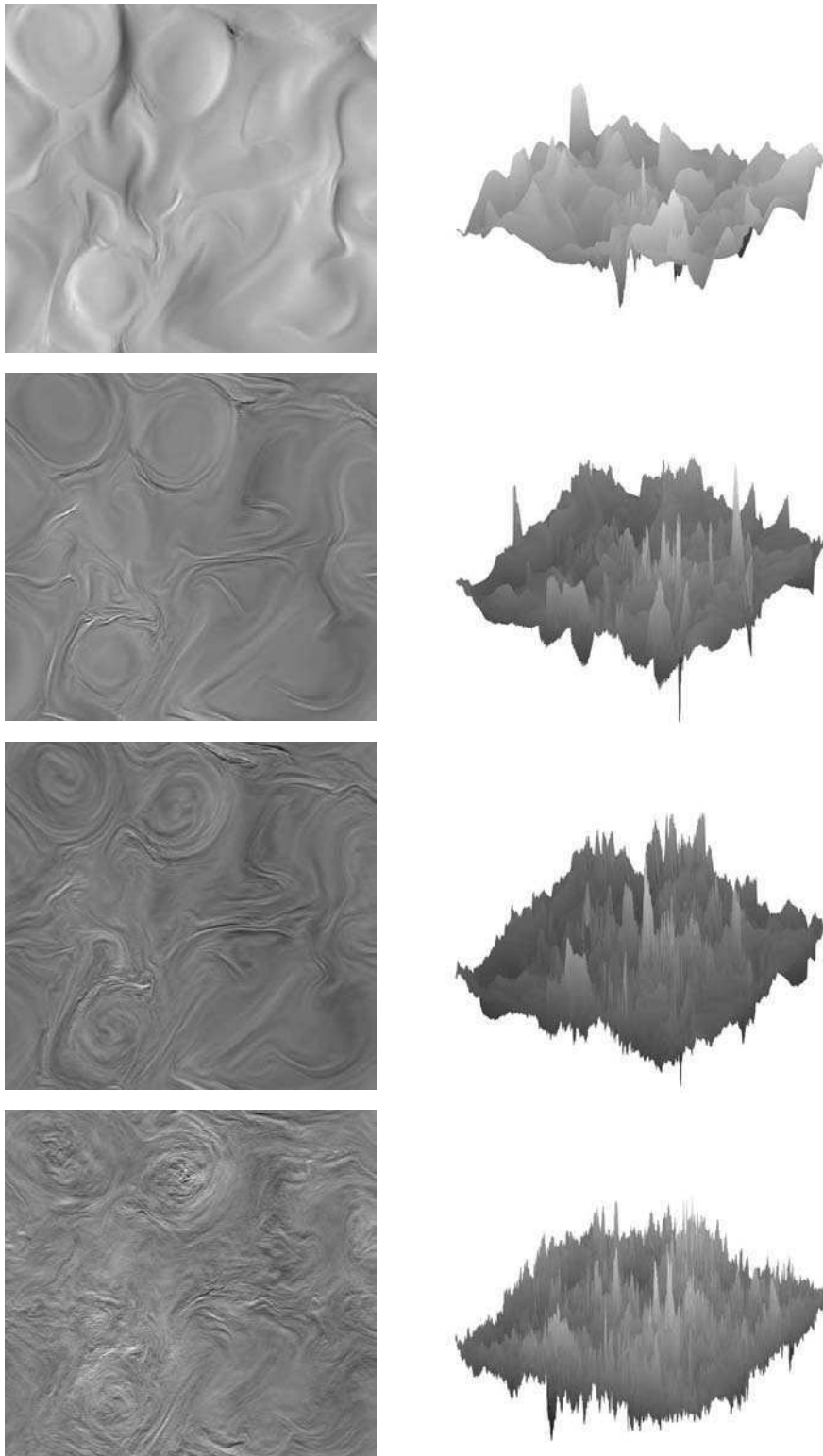


Figure 5.1: Left panels: slices of the perpendicular current component  $j_x$  in the perpendicular plane, for the four different values of  $\varepsilon$  used ( $\varepsilon$  increasing from top to bottom). Right panels: the same fields, seen at an arbitrary tilt angle. The scale of grays is arbitrary.

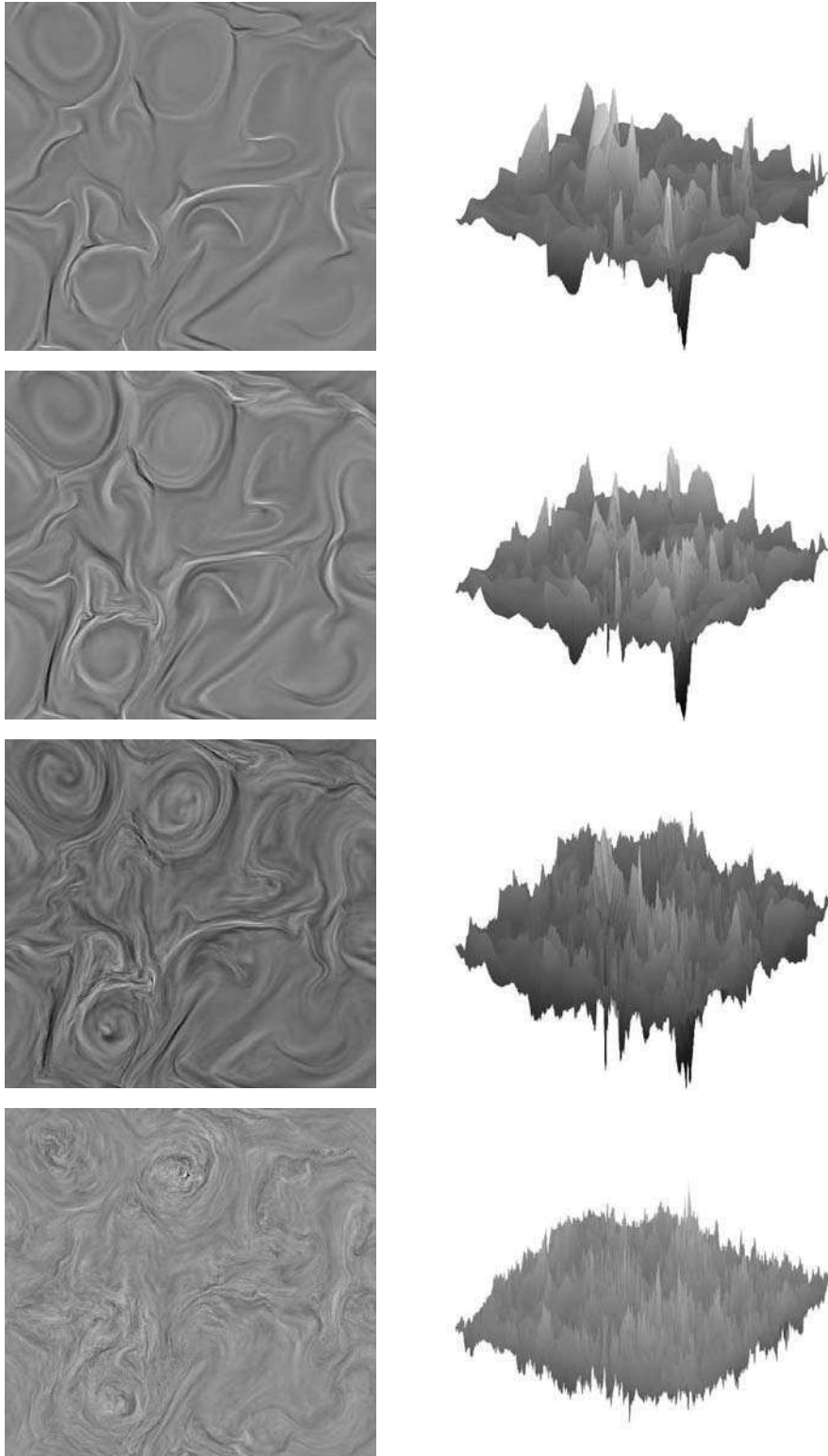


Figure 5.2: Left panels: slices of the parallel current component  $j_z$  in the perpendicular plane, as in previous figure. Right panels: the same fields, seen at an arbitrary tilt angle.

## 5. Statistical properties

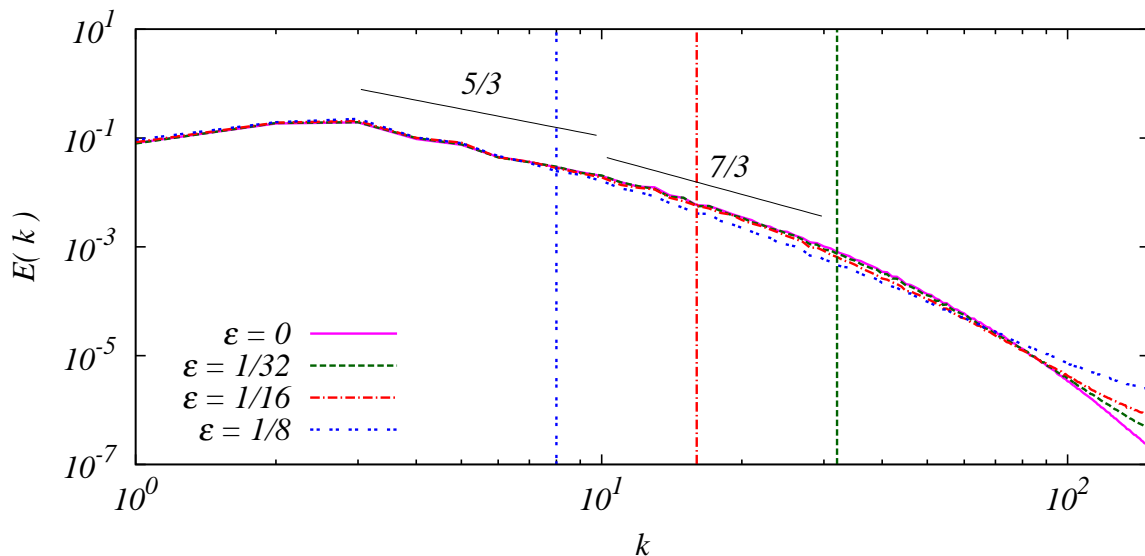


Figure 5.3: The total energy spectra for the four Runs (see legend). Phenomenological predictions for the MHD range and for the Hall range are also indicated

[9, 10, 11, 12, 13, 3]. Solar wind measurements have also revealed the presence of structures of different type (current sheets, rotational discontinuities, vortices) [14, 15, 16, 17]. Since structures can be seen as smooth regions embedded in a highly fluctuating field, they can be associated to scale dependent changes of the sign of the fields gradients. The introduction of a sign-singular measure (as opposed to a positive defined probability measure) allows the characterization of the scaling properties of sign oscillations of the fields [6]. The signed measure of a mean-less scalar field  $f(\mathbf{r})$ , defined on a  $d$ -dimensional set  $Q(L)$  of size  $L$ , can be introduced as follow. Let  $\{Q_i(l)\} \subset Q(L)$  be a partition of  $Q(L)$  in disjoint subsets of size  $l$ . Then, for each scale  $l$  and for each set of boxes  $Q_i(l)$ , the signed measure is defined as

$$\mu_i(l) = \frac{\int_{Q_i(l)} \mathbf{dr} \mathbf{f}(\mathbf{r})}{\int_{Q(L)} \mathbf{dr} |\mathbf{f}(\mathbf{r})|}. \quad (5.1)$$

As the scale of the subset  $Q_i(l)$  increases, cancellations between small size structures of opposite sign become more probable within each box. The way this happens can be statistically characterized through the partition function

$$\chi(l) = \sum_{Q_i(l)} |\mu_i(l)| \quad (5.2)$$

where the sum is extended to all disjoint subset  $Q_i(l)$ . When the partition function shows power law scaling  $\chi(l) \sim l^{-\kappa}$ , the measure is said *sign singular*, and  $\kappa$  is called *cancellation exponent*, representing a quantitative measure of the cancellation efficiency. For example, a

smooth field has constant partition function ( $\kappa = 0$ ), whereas for a stochastic process  $\kappa = d/2$  ([18]). More generally, if a field  $\mathbf{g}(\mathbf{r})$  is homogeneous with a Hölder scaling exponent  $h$ , that is if  $\langle \|\Delta \mathbf{g}(\mathbf{l})\| \rangle = \langle \|\mathbf{g}(\mathbf{r} + \mathbf{l}) - \mathbf{g}(\mathbf{r})\| \rangle \sim l^h$ , then the cancellation exponent of its derivative  $f \equiv dg/dr$  is  $\kappa = 1 - h$  [18, 19]. Thus, cancellation exponents characterize the topology of structures. A simple geometrical argument, based on the separation of the field in correlated (the structures) and uncorrelated (the background field) subsets, allows to establish a phenomenological relationship between the cancellation exponent and the fractal dimension  $D$  of the typical dissipative structures of the flow

$$\kappa = (d - D)/2 \quad (5.3)$$

(see e.g. [7] for details). It should be kept in mind that, because multifractality is ubiquitous in MHD turbulence, the use of one single fractal dimension cannot capture all the features of the scaling. Nonetheless,  $D$  still represents a useful indicator for the topological characteristics of the “mean” intermittent structures of the flow (and even more when there are using other elements of analysis as we have done). Cancellation analysis has been performed in the past to describe the formation of structures in two dimensional MHD plasmas [7, 20], and successfully applied to solar active regions, where the time evolution of the topological properties of the surface current has allowed to predict the occurrence of large flares [21, 22, 23].

In this paper, we show results of the cancellation analysis of the fields with the aim of pointing out the effect of the Hall term on the topology of the small scales structures.

## 5.5 Cancellation analysis in turbulent plasmas

For our analysis, we have considered four snapshots of RHMHD simulations, realized using four different values of the Hall parameter  $\varepsilon$ , as indicated in Section 5.2. All the snapshots are taken in a statistically steady state of the system, realized when  $t = 4.5$ . The fields analyzed here are the three components of the current  $\mathbf{j}$  and of the vorticity  $\boldsymbol{\omega}$ , already shown in Figures 5.1 and 5.2. To estimate the partition functions, we divided the simulation domain of size  $L^3 = (2\pi)^3$  in boxes of variable size  $l_x \times l_y \times l_z$ , with  $l_x = l_y = l_\perp$  and  $l_z = l_\parallel$ .

Figure 5.4 shows some examples of two dimensional cuts of the signed measure computed for the parallel component of the current  $j_z$  in the plane  $x$ - $y$ , for two values of  $\varepsilon$ , and for four different partition box sizes. It is evident that the coarse graining of the set partition leads to cancellations at larger scales, so that small scale structures (the current filaments clearly evident at small scale, see left panel) gradually disappear. Similar behavior is seen for all fields components, and for any value of the Hall parameter (not shown).

From the signed measures, partition functions (5.2) have been computed for all components of the current  $\mathbf{j}$  and of the vorticity  $\boldsymbol{\omega}$  as a function of the two scale parameters  $l_\perp$  and  $l_\parallel$ . Ex-

## 5. Statistical properties

---

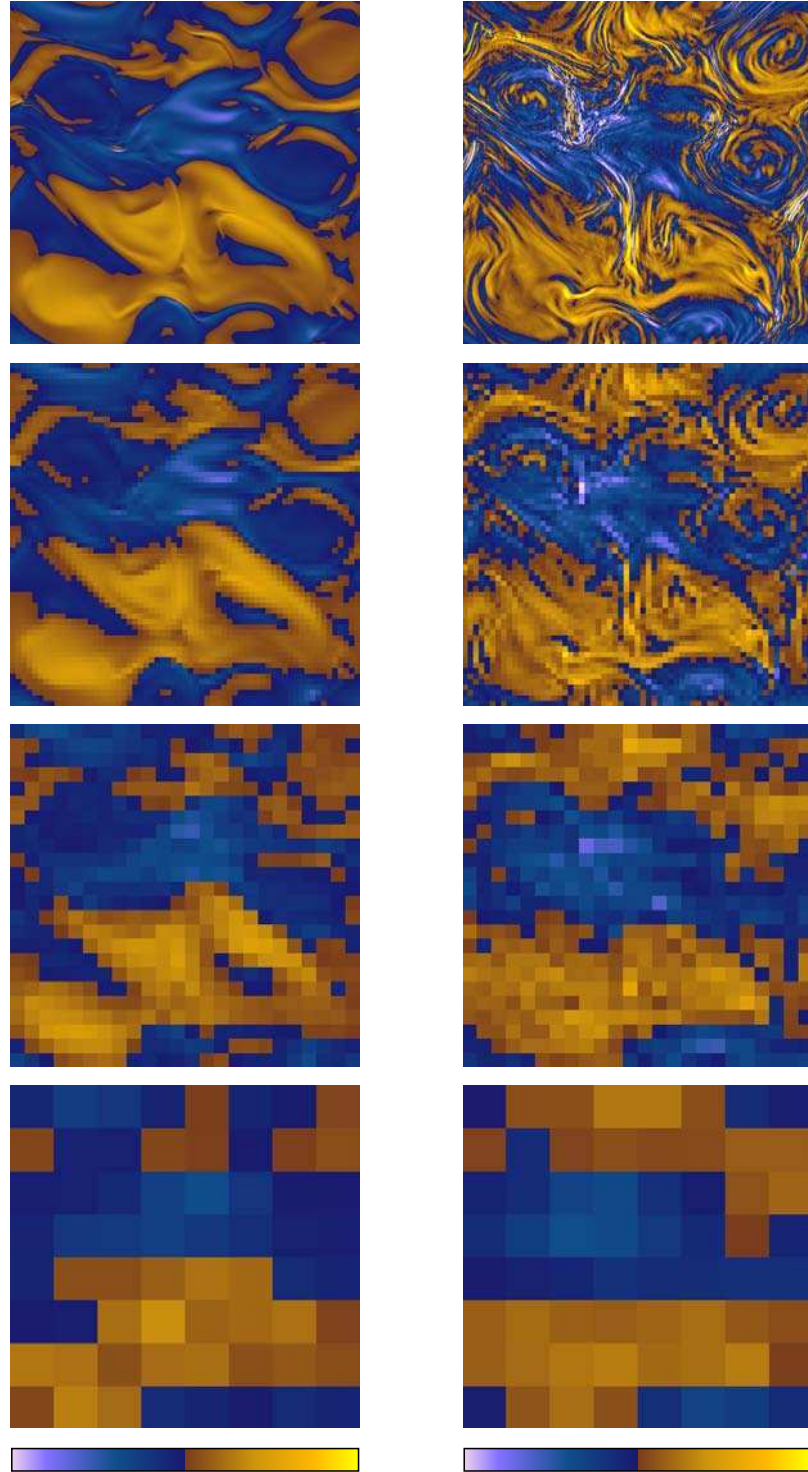


Figure 5.4: The signed measure  $\mu$  as estimated for  $j_x$  in the plane  $y$ - $z$ , for Run A ( $\varepsilon = 0$ , left panels) and Run C ( $\varepsilon = 1/16$ , right panels), for four different partition box sizes (from top to bottom,  $l_{\perp} = 0.12, 0.04, 0.016$  and  $0.002$ ). The color scale is arbitrary.

amples of the results are presented in Figure 5.5. While it is evident that scaling properties are present and well developed in the perpendicular direction  $l_{\perp}$ , the partition functions decrease with the parallel scale  $l_{\parallel}$  is somewhat smoother and less defined. This is due to the fact that in RHMHD the turbulent cascade is mainly developed in the perpendicular plane to the mean field. For this reason, we will mainly concentrate on the scaling properties in the perpendicular plane, by selecting one particular parallel scale. We analyzed the results for different parallel scales, and no significant difference was observed.

Figures 5.6 and 5.7 show examples of the partition functions of the fields for a fixed value of  $l_{\parallel} = 0.03$ , and for different  $\varepsilon$ . When appropriate, power law fits  $\chi(l_{\perp}) \sim l_{\perp}^{-\kappa}$  have been performed through a least square method. The fitting curves are displayed in the figures. For a visual test, the partition functions have been compensated by dividing them by the fitted power law  $l_{\perp}^{-\kappa}$ , and represented in the bottom panels of each figure. Scaling ranges are seen as flat regions in the compensated plots. Compensated plots and fitting power laws have been represented as full lines for the Hall range, and with double-dashed lines for the MHD range.

As can be seen in all panels of figures 5.6 and 5.7, the partition functions suggests presence of power law scaling, and therefore sign singularity, in a range of perpendicular scales corresponding to the inertial range of the energy spectra (cf. figure 5.3). This holds for all fields and Hall parameters, and is the signature of the MHD turbulent cascade among structures of different size [7]. A second power law range emerges at small scales when the strength of the Hall term increases (panels *g-h* of figures 5.6 and 5.7). This suggests that a secondary sign singularity is present, with fragmentation of dissipative structures along the scales, presumably due to the nonlinear Hall cascade. The small scale power law is observed for the current and vorticity components lying on the plane perpendicular to  $B_0$ , while for the parallel components the secondary sign singularity only appears for the largest value of  $\varepsilon$  analyzed here (panels *g* and *h*). This is in agreement with the emergence of a small scale power law range in the energy spectra (see figure 5.3), which has HMHD phenomenological spectral index.

As mentioned in a previous Section, values of the cancellation exponents provide information on the topology of the fields. In order to discuss more easily the analysis results, cancellation exponents have been converted into the typical fractal dimension of the structures, as  $D = 3 - 2\kappa$ . Values of  $D$  are then displayed in Figure 5.8 as a function of  $\varepsilon$ , for the three components of the current (panels *a* and *c*) and of the vorticity (panels *b* and *b*), so that the influence of increasing Hall effect on the scaling can be evaluated. In the following, we will use the notation  $D_{\perp}^{(f)}$  for fractal dimension estimated for the perpendicular partition function  $\chi(l_{\perp})$ , and  $D_{\parallel}^{(f)}$  for the parallel partition function  $\chi(l_{\parallel})$ , where  $f = j, \omega$  indicates the field under study. When the superscript  $^{(f)}$  is omitted, we are indicating both fields. It is also possible to introduce a parameter for estimating the “global” fractal dimension of the fields, by averaging

## 5. Statistical properties

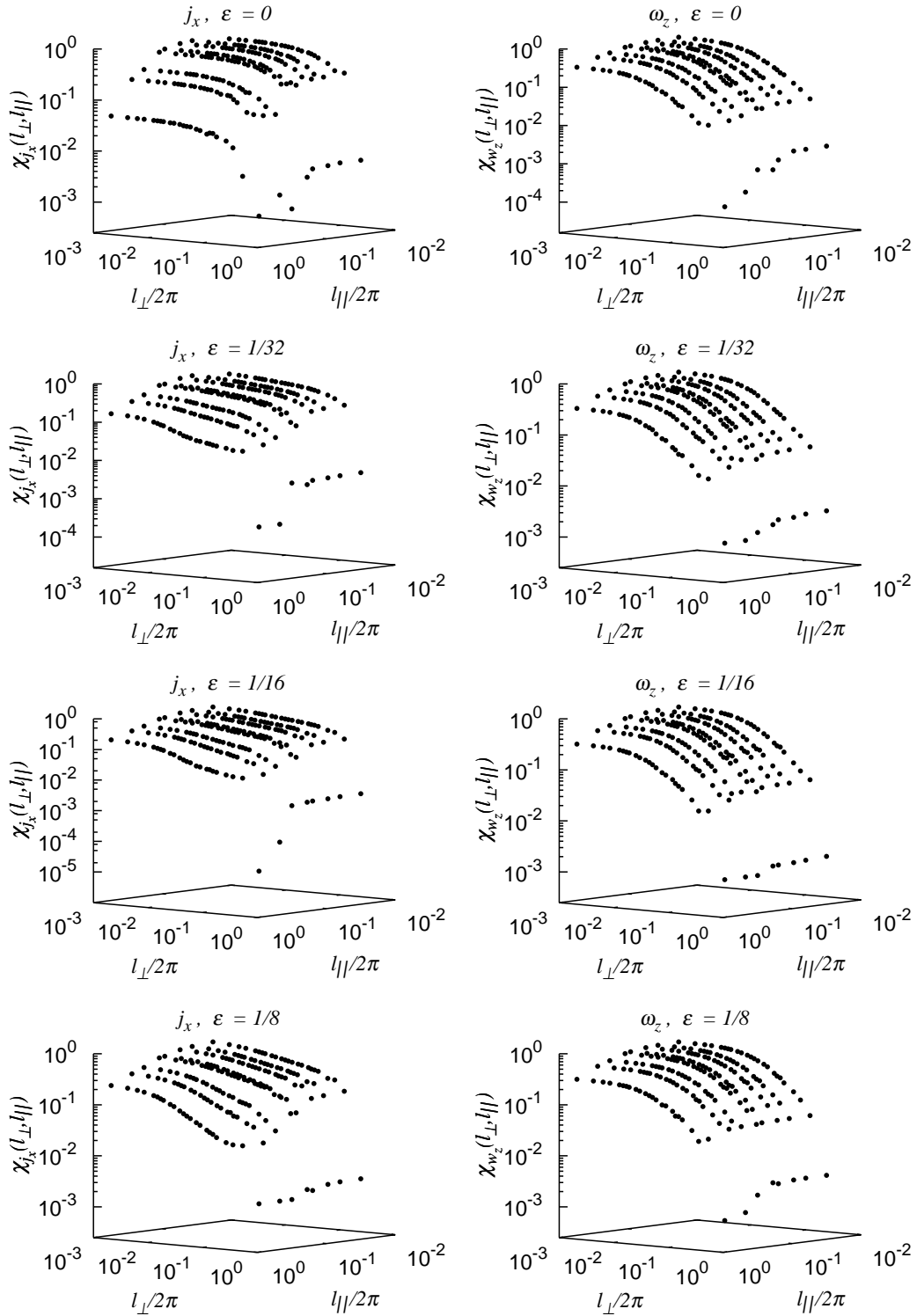


Figure 5.5: The partition function  $\chi(l_{\perp}, l_{\parallel})$  versus the two scale parameters  $l_{\parallel}$  and  $l_{\perp}$ . The examples given here refer to the parallel components of the current ( $j_z$ , left hand plots) and one of the perpendicular components of the vorticity ( $w_x$ , right hand plots), for the four values of the Hall parameter (sorted from top to bottom for increasing  $\varepsilon$ , as indicated in each plot).

## 5.5. Cancellation analysis in turbulent plasmas

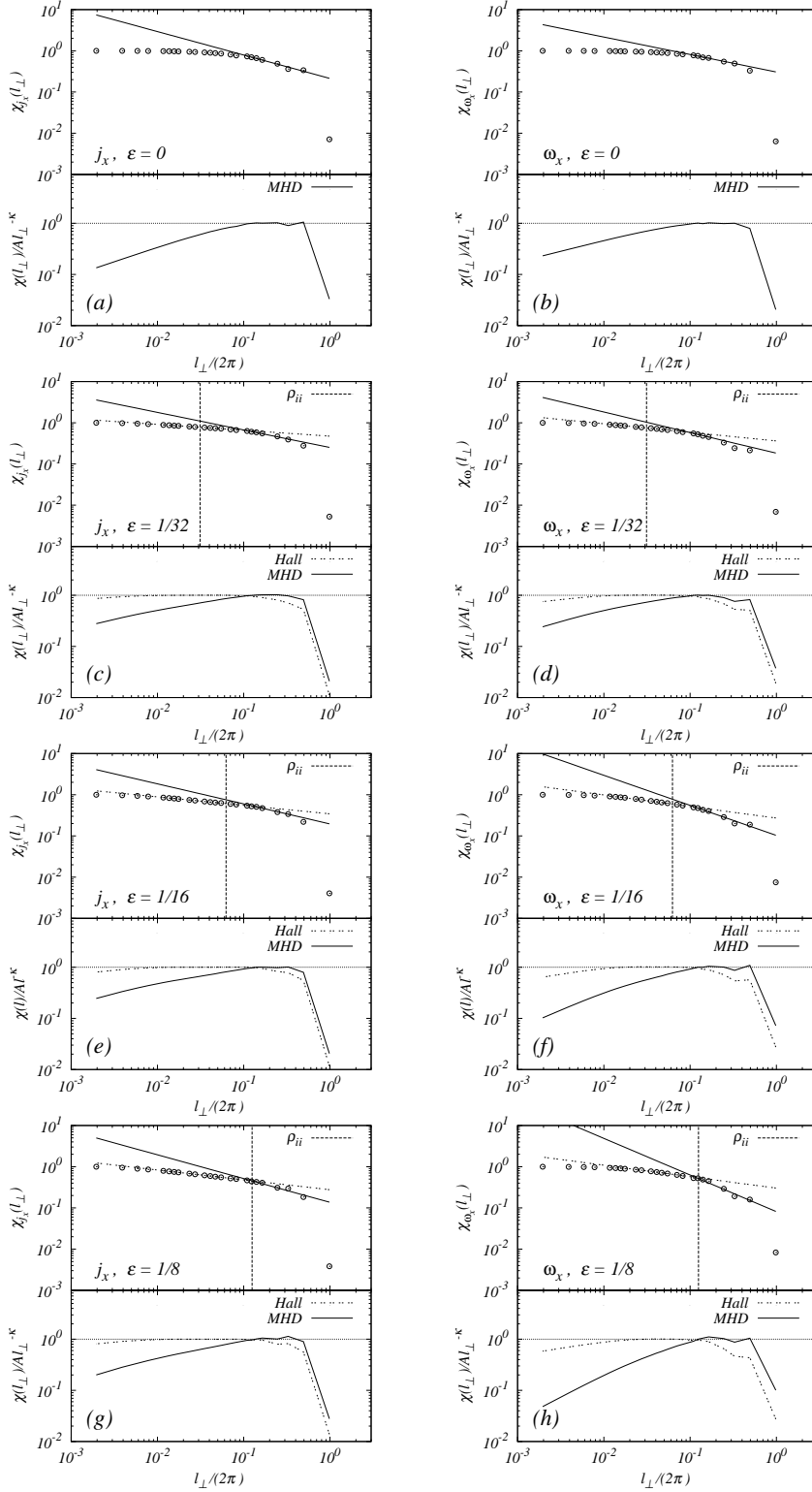


Figure 5.6: The partition function  $\chi(l_{\perp})$  versus the scale parameter  $l_{\perp}$  for  $j_x$  (left) and  $\omega_x$  (right), for the four runs ( $\varepsilon$  increasing from top to bottom), and at  $l_{\parallel}/2\pi = 0.03$ . Power law fits  $\chi(l_{\perp}) = A(l_{\perp}/2\pi)^{-\kappa}$  are superimposed. The ion skin depth is indicated (dashed line). Finally, the bottom part of each plot shows the compensated partition function  $\chi(l_{\perp})/A(l_{\perp}/2\pi)^{-\kappa}$ .

## 5. Statistical properties

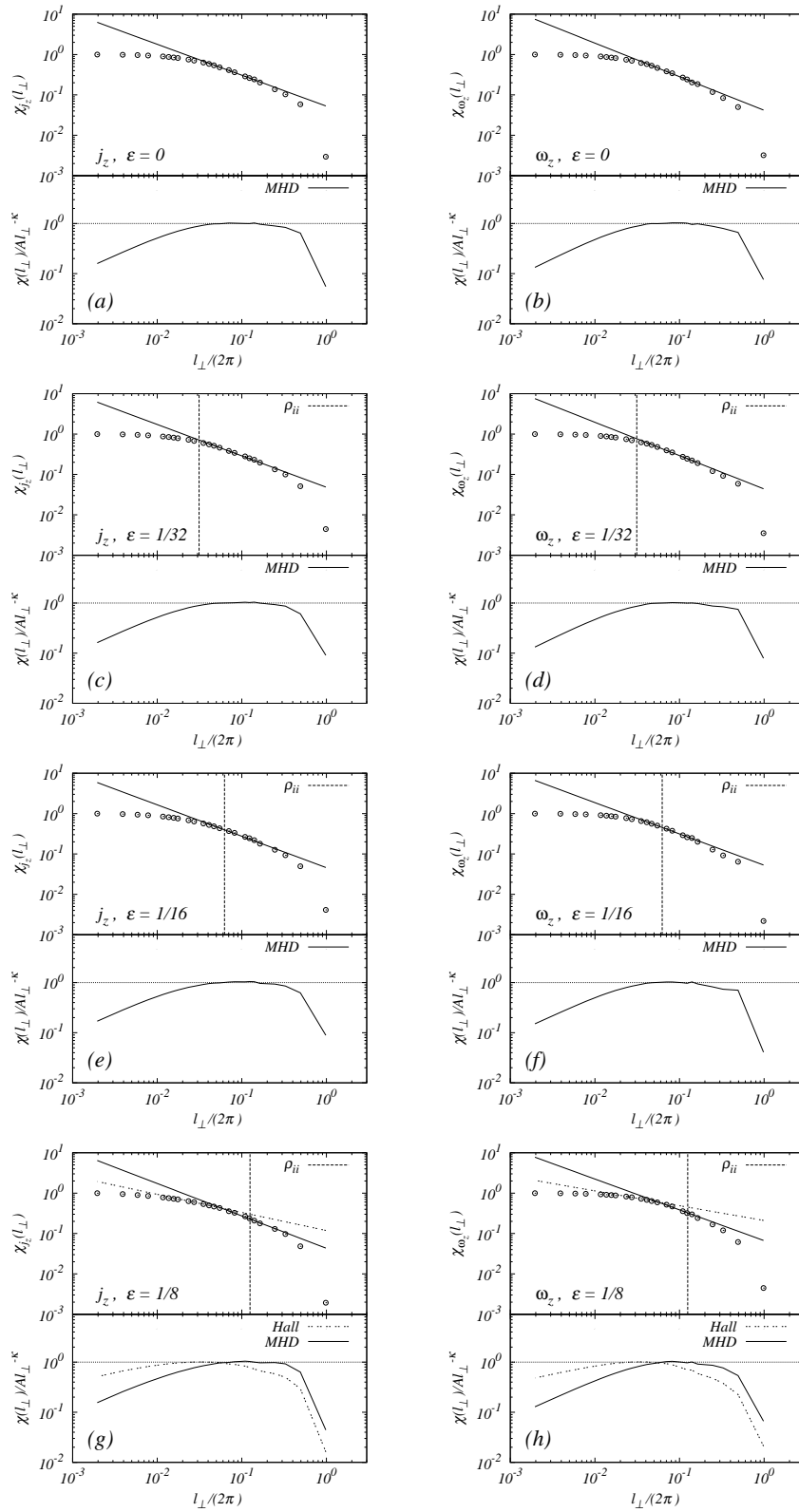


Figure 5.7: Same as Figure 5.6, for the parallel component:  $j_z$  (left hand plots) and  $\omega_z$  (right hand plots).

the three values  $D_i^{(f)}$  of the fractal dimension obtained for the  $i$ -th component of each field  $f$ ,  $D_{\perp}^{*(f)} = (D_x^{(f)} + D_y^{(f)} + D_z^{(f)})/3$  (we have temporarily suppressed the subscript  $\perp$  in this formula, to simplify the notation).

We remind that, in the RHMHD configuration, most of the nonlinear structures are generated in the plane perpendicular to  $B_0$ . Therefore, the parallel component of the current  $j_z$  and vorticity  $\omega_z$ , which depend on the perpendicular components of the magnetic and velocity fields, are of particular interest. The perpendicular components  $j_x, j_y, \omega_x, \omega_y$ , on the contrary, include both the perpendicular and parallel components of magnetic and velocity fields. This results in mixing the turbulent perpendicular dynamics with the quasi-linear parallel dynamics, so that results are not easily interpreted.

In the MHD inertial range, marked as ‘‘MHD’’ in the figures, the estimated fractal dimension for the parallel component of the current is almost constant, showing a weak decrease from  $D_{\perp}^{(j)} = 1.5$  in the MHD regime to  $D_{\perp}^{(j)} = 1.4$  in the Hall regime (red plot in Figure 5.8, panel *a*). Similar values, but with opposite weak trend, are observed for the vorticity  $\omega_z$  (panel *b*). Such values of  $D$  are representative of severely disrupted, almost filamented current sheets. The relative independence of  $D_{\perp}^{(j)}$  on the Hall parameter for the parallel components of vorticity and current is consistent with the fact that, in the MHD inertial range, the Hall term is not expected to play a relevant role, since it should only be effective at smaller scales.

For the current perpendicular components (green and blue plots in Figure 5.8, panel *a*),  $D_{\perp}^{(j)}$  starts around 2 (indicating current sheets) with no Hall effect. As the Hall term is turned on, the dimension first weakly increases to about  $D_{\perp}^{(j)} \simeq 2.2$ , and then steadily decreases back to  $D_{\perp}^{(j)} \simeq 2$ , showing that structures are becoming more complex. This suggests that inertial range fields are reacting to the onset of the Hall effect, probably in response to the inertial range modification. For the vorticity components perpendicular to  $B_0$  (green and blue plots in Figure 5.8, panel *b*), the effect of the Hall term is even more evident, causing a decrease of the dimension from  $D_{\perp}^{(\omega)} \simeq 2.3$  to  $D_{\perp}^{(\omega)} \simeq 1.5$ , indicating with fragmentation of the vorticity sheets. The ‘‘global’’ fractal dimensions  $D_{\perp}^*$  are shown in Figure 5.8, panel *e* (for the current) and panel *f* (for the vorticity), for both the MHD and Hall ranges. For the current in the MHD range, the structures topology is roughly constant for all values of the Hall effect. Vorticity, on the contrary, shows a more evident decrease of the ‘‘global’’ fractal dimension with  $\varepsilon$ , from  $D_{\perp}^{*(\omega)} \simeq 2.3$  to  $D_{\perp}^{*(\omega)} \simeq 1.5$ . This result shows that magnetic field and velocity are decoupled in the MHD range, so that their structures have different topological properties.

We now turn our attention to the range of scales smaller than the ion skin depth, where the Hall term becomes relevant when  $\varepsilon$  becomes larger. Results here are very similar for both current and vorticity, suggesting that velocity and magnetic fields decouple only in the MHD range. If no Hall cascade is present ( $\varepsilon = 0$ , see panels *a* and *b* of figures 5.6 and 5.7), the

## 5. Statistical properties

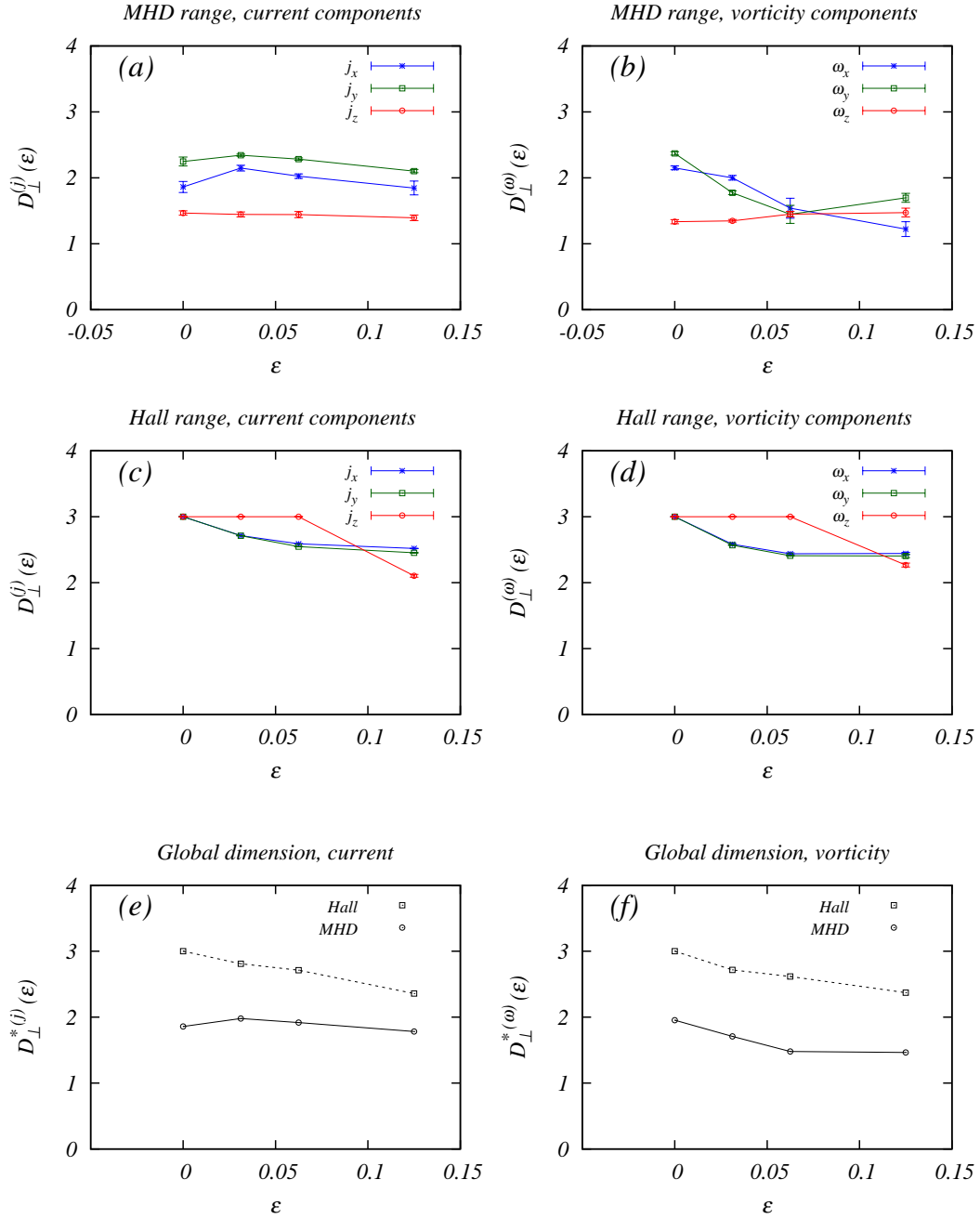


Figure 5.8: The fractal dimension  $D_{\perp}$  estimated through equation 5.3, for the three components of current (a for the MHD range, c for the Hall range) and vorticity (b for the MHD range, d for the Hall range), labeled with different colors and line style (see inset). The indicators  $D_{\perp}^*$  (see text) are also plotted for the two fields (panels e and f, black lines).

small scale range is characterized by smooth fluctuations (for which we assume  $D_{\perp} = 3$ ) for all components of the fields, as expected when dissipation is active and numerically well resolved. This is reflected in the absence of power law, or sign singularity, in the transition from the MHD range toward the constant partition function value for smooth fields ( $\chi = 1 \rightarrow \kappa = 0 \rightarrow D = 3$ ) at small scales. As the Hall effect comes into play, the perpendicular components of current and vorticity start to develop a power law range, with cancellation exponents  $\kappa$  increasing with  $\varepsilon$  (panels *c-f* of figure 5.6). The scaling of the partition function indicates the presence of strongly persistent structures, in the range of scales larger than the typical dissipative scales. In terms of fractal dimension (green and blue plots in Figure 5.8, panels *c* and *d*), a decrease is observed from  $D_{\perp} = 3$  to  $D_{\perp} \simeq 2.4$ , indicating that the smooth fields in the MHD regime (Run A) are developing toward more complex, broken structures (Runs B, C and D). On the other hand, for the parallel component of current and vorticity the sign singularity in the Hall range is only observed at  $\varepsilon = 1/8$  (see panels *c-f* of figure 5.7). At this value of the Hall parameter, the field is no longer smooth (as instead happens for dissipative range), but rather shows presence of quasi two-dimensional sign persistent structures (red plots in Figure 5.8, panels *c* and *d*). At these small scales, the “global” fractal dimension calculated for the current and the vorticity steadily decreases from  $D_{\perp}^* = 3$  to  $D_{\perp}^* \simeq 2.3$  as the Hall term coefficient increases, confirming once more that the turbulent structures are being fragmented by the nonlinear Hall cascade.

Finally, we quickly review the results obtained for the scaling in the parallel direction. Figure 5.9 shows some examples of partition functions of the current and vorticity components, as a function of the parallel scale,  $\chi(l_{\parallel})$ . Partition functions were estimated for  $l_{\perp}/2\pi = 0.002$ . As evident, the power law range is severely reduced because of the lower resolution of the numerical simulations. However, we have fitted the partition functions with the usual power law, obtaining the cancellation exponents  $\kappa$  and, therefore, the fractal dimensions  $D$ . These are shown in figure 5.10 as a function of the Hall parameter. As expected from the RHMHD model, for both fields the component parallel to the magnetic field has almost constant  $D_{\parallel} \simeq 2.2$  (see the red plots in panels *a* and *b* of figure 5.10). On the contrary, for the two components on the perpendicular plane,  $D_{\parallel}$  increases with  $\varepsilon$  from very small values ( $D_{\parallel} \simeq 0.8$ ) to about  $D_{\parallel} \simeq 1.9$  (green and blue plots in panels *a* and *b* of figure 5.10), similarly to what is observed for the perpendicular partition functions. The “global” fractal dimension increases from  $D_{\parallel}^* = 1.3$  to  $D_{\parallel}^* = 2$ .

## 5.6 Conclusions

In this last chapter, a set of simulations of a RHMHD flow realized with different values of the Hall parameter  $\varepsilon$  was analyzed by using the sign-singular measure. The presence of power law

## 5. Statistical properties

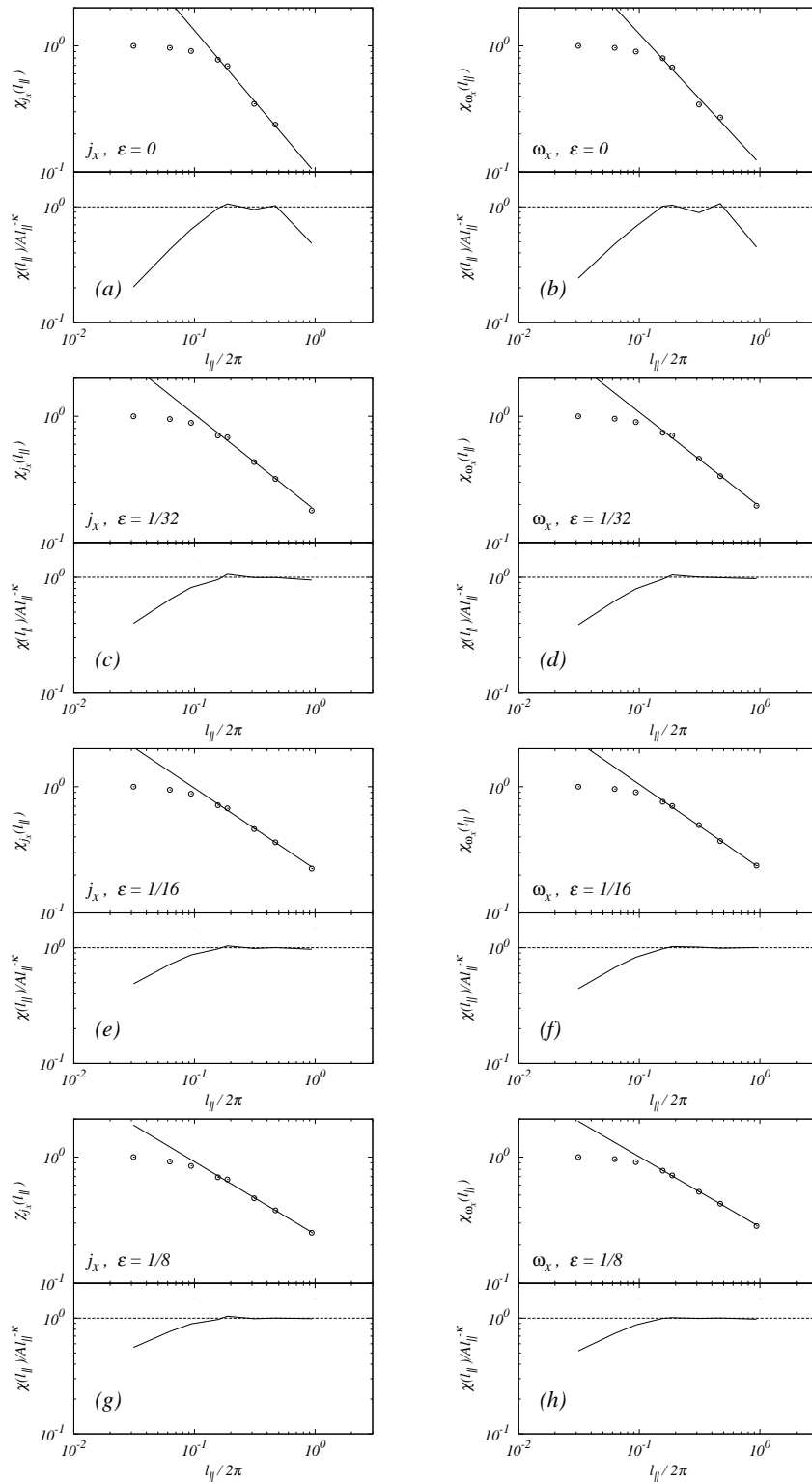


Figure 5.9: The partition function  $\chi(l_{\parallel})$ , for  $j_x$  (left) and  $\omega_x$  (right), for the four runs ( $\varepsilon$  is indicated in each plot), and at  $l_{\perp}/2\pi = 0.002$ . Power law fits are superimposed. The bottom part of each plot shows the compensated partition function  $\chi(l_{\parallel})/A(l_{\parallel}/2\pi)^{-\kappa}$ .

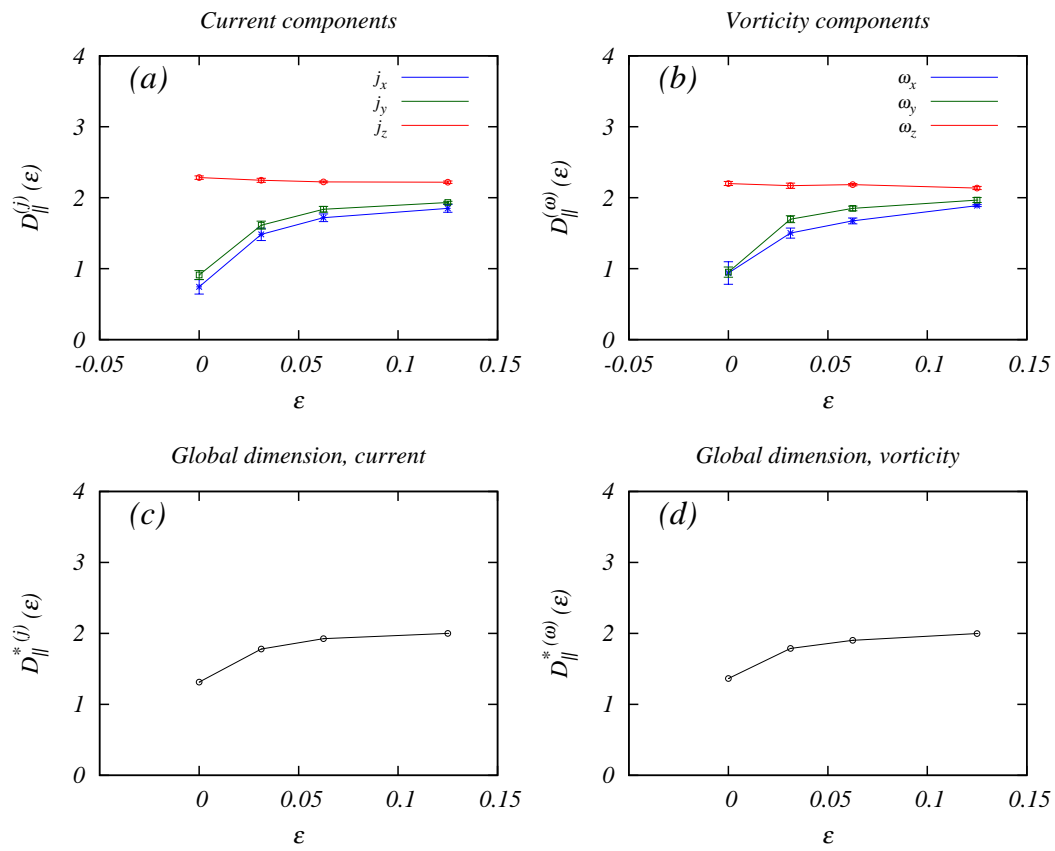


Figure 5.10: The fractal dimension  $D$  of the parallel partition function, for the three components of current (left panels) and vorticity (right panels). The overall indicators  $D_{\parallel}^*$  are also plotted for the two fields (bottom panels).

## 5. Statistical properties

---

scaling of the partition function was observed in two distinct ranges of scales, corresponding to the MHD and Hall MHD ranges. This is interpreted as the presence of an active nonlinear turbulent cascade generating structures (i.e. parts of the fields with persistent sign) on all scales. The cancellation exponents, measured by fitting the partition functions, indicate the degree of cancellation occurring between structures of opposite sign, and are related to the gross fractal dimension of the typical turbulent structures in the flow. In the MHD range, current structures are only weakly sensitive to the Hall effect, showing slightly decreasing fractal dimension in particular in the perpendicular current components. The vorticity structures have a more evident fragmentation, suggesting that velocity and magnetic field may have decoupled dynamics in this range. In the Hall range, current and vorticity have similar behaviour, showing increasingly unraveled structures. The nonlinear Hall term is thus responsible for disruption and unraveling of the MHD current sheets, and for the generation of small scale structures.

The results obtained here, together with previous analysis [2, 4], provide a comprehensive approach that might answer the basic question: do the sheets get wider or narrower with the Hall effect? We can conclude that the Hall term has dual effects on the current sheets at different scales. On one hand, it increases the “macroscale” of the sheets by proportionally increasing their characteristic size. On the other hand, it causes these structures to unravel, which corresponds to generating microstructures on smaller scales. The decrease of the fractal dimension is a manifestation of the emerging microscales, while the widening of the macroscale of the sheet produces an increase of the filling factor of these microstructures, and the subsequent reduction of the observed intermittency [4].

These results may settle both the numerical and observational debate about the widening *vs* narrowing of the current sheets, which was probably due the extremely complex nature of the structures. Therefore, more comprehensive analysis, based on multiple approach to the same set of data (global magnitudes, characteristic times, energy cascade, intermittency, geometrical and topological properties) is desirable in order to fully understand the effect of the Hall term on the flow dynamics, and in particular on the topological characteristics of the current sheets. This work, along with Refs. [2, 4], may be an example of such comprehensive approach.

# Bibliography

- [1] L. N. Martin, G. De Vita, L. Sorriso-Valvo, P. Dmitruk, G. Nigro, L. Primavera, V. Carbone, Phys. Rev. E, **Accepted on 01/07/2013**. [87](#)
- [2] L. N. Martin, P. Dmitruk, and D. O. Gómez, Phys. Plasmas, **19**, 052305 (2012). [87](#), [88](#), [104](#)
- [3] S. Donato, S. Servidio, P. Dmitruk, V. Carbone, M. A. Shay, and P. A. Cassak, Phys. Plasmas, **19**, 092307 (2012). [87](#), [92](#)
- [4] P. Rodriguez Imazio, L. N. Martin, and P. D. Mininni, Phys. Plasma, **20**, 052506 (2013). [88](#), [104](#)
- [5] M. Wan, S. Oughton, S. Servidio and W.H. Matthaeus, Phys. Plasmas **17**, 082308 (2010). [88](#)
- [6] E. Ott, Du. K. R. Sreenivasan, A. Juneja, and A. K. Suri, Phys. Rev. Lett. **69**, 2654 (1992). [88](#), [92](#)
- [7] L. Sorriso-Valvo, V. Carbone, A. Noullez and H. Politano, A. Pouquet, P. Veltri, Phys. Plasmas, **9**, 89-95 (2002). [88](#), [93](#), [95](#)
- [8] U. Frisch, *Turbulence: The legacy of A.N. Kolmogorov*, Cambridge Univ. Press, Cambridge, UK (1995). [89](#)
- [9] A. Brandenburg, I. Procaccia and D. Segel, Phys. Plasmas **2**, 1148 (1995). [92](#)
- [10] H. Politano, A. Pouquet and P. L. Sulem, Phys. Plasmas **2** (8), 2931 (1995). [92](#)
- [11] R. M. Kerr and A. Brandenburg, Phys. Rev. Lett. **83** 1155 (1999). [92](#)
- [12] D. Biskamp and H. Welter, Phys. Fluids B **1**, 1964 (1989). [92](#)
- [13] H. Karimabadi et al., Phys. Plasmas **20**, 012303 (2013). [92](#)

## BIBLIOGRAPHY

---

- [14] P. Veltri, *Plasma Phys. Cont. Fus.* **41**, A787-A79 (1999). [92](#)
- [15] C. Salem, A. Mangeney, S.D. Bale, P. Veltri, *Astrophys. J.* **702**, 537-553 (2009). [92](#)
- [16] A. Greco, P. Chuychai, W. H. Matthaeus, S. Servidio, P. Dmitruk, *Geophys. Res. Lett.* **35**, L19111 (2008). [92](#)
- [17] D. Sundkvist, A. Retinò, A. Vaivads, S. D. Bale, *Phys. Rev. Lett.* **99**, 025004 (2007). [92](#)
- [18] S. I. Vainshtein, Y. Du, and K. R. Sreenivasan, *Phys. Rev. E* **49**, R2521 (2007). [93](#)
- [19] A. L. Bertozzi and A. B. Chhabra, *Phys. Rev. E* **49**, 4716 (1994). [93](#)
- [20] J. Graham, P. D. Mininni, and A. Pouquet, *Phys. Rev. E* **72**, 045301(R) (2005). [93](#)
- [21] V. B. Yurchyshyn, V. I. Abramenko, and V. Carbone, *Astrophys. J.*, **538**, 968 (2000). [93](#)
- [22] V. I. Abramenko, V. B. Yurchyshyn, and V. Carbone, *Solar Phys.* **178**, 35, (1998). [93](#)
- [23] L. Sorriso-Valvo, V. Carbone, P. Veltri, V. I. Abramenko, A. Noullez, H. Politano, A. Pouquet, V. B. Yurchyshyn, *Planet. Space Sci.* **52**, 937 – 943 (2004). [93](#)

# Chapter 6

## Beyond the Hall effect: electron inertia

### Contents

---

<b>6.1 Electron Inertia Hall-MHD model (EIHMHD)</b> . . . . .	<b>107</b>
<b>6.2 2.5D Setup</b> . . . . .	<b>109</b>
6.2.1 Linear modes . . . . .	110
6.2.2 Ideal invariants in 2.5D . . . . .	111
<b>6.3 Preliminar results for turbulence</b> . . . . .	<b>112</b>

---

In this chapter we go beyond the Hall-MHD model by developing a two-fluid model for a fully ionized hydrogen plasma. We are currently using this model to expand the studies done in this thesis regarding to magnetohydrodynamics turbulence but not neglecting the electron mass. Since the ratio of electron mass to proton mass is small (by three orders of magnitude) This introduces additional small length and timescales into the dynamics.

We developed the electron inertia Hall MHD model, introduce new parameters, and consider the general invariants of the system. We then consider a simplified case in 2.5 dimensions, analyze the linear modes of the system and further present preliminar results for a fully turbulent case.

### 6.1 Electron Inertia Hall-MHD model (EIHMHD)

The equations of motion for a plasma made of protons and electrons with mass  $m_{p,e}$ , charge  $\pm e$ , density  $n_p = n_e = n_o$  (quasi-neutrality), pressure  $p_{p,e}$  and velocity  $\mathbf{u}_{p,e}$  respectively, can be

## 6. Beyond the Hall effect: electron inertia

written as

$$m_p n_o \frac{d\mathbf{u}_p}{dt} = en_o \left( \mathbf{E} + \frac{1}{c} \mathbf{u}_p \times \mathbf{B} \right) - \nabla p_p + \mu_p \nabla^2 \mathbf{u}_p + R_{pe} \quad (6.1)$$

$$m_e n_o \frac{d\mathbf{u}_e}{dt} = -en_o \left( \mathbf{E} + \frac{1}{c} \mathbf{u}_e \times \mathbf{B} \right) - \nabla p_e + \mu_e \nabla^2 \mathbf{u}_e + R_{ep} \quad (6.2)$$

$$\mathbf{j} = \frac{c}{4\pi} \nabla \times \mathbf{B} = en_o (\mathbf{u}_p - \mathbf{u}_e) \quad (6.3)$$

where (6.3) corresponds to Ampere's law neglecting the displacement current, and  $c$  is the speed of light. The conservation of mass for each species implies

$$\frac{\partial(m_{p,e}n_o)}{\partial t} + \nabla \cdot (m_{p,e}n_o \mathbf{u}_{p,e}) = 0 \quad (6.4)$$

This set of equations can be written in a dimensionless form in terms of a typical length scale  $L_0$ , a constant particle density  $n_0$ , a value for the magnetic field  $B_0$  and a typical value of velocity  $u_0 = v_A = B_0 / \sqrt{4\pi n_0 M}$  where  $M \equiv m_p + m_e$ ,

$$(1 - \delta) \frac{d\mathbf{u}_p}{dt} = \frac{1}{\epsilon} (\mathbf{E} + \mathbf{u}_p \times \mathbf{B}) - \nabla p_p + \nu_p \nabla^2 \mathbf{u}_p + r_{pe} \quad (6.5)$$

$$\delta \frac{d\mathbf{u}_e}{dt} = -\frac{1}{\epsilon} (\mathbf{E} + \mathbf{u}_e \times \mathbf{B}) - \nabla p_e + \nu_e \nabla^2 \mathbf{u}_e + r_{ep} \quad (6.6)$$

$$\epsilon \mathbf{j} = \mathbf{u}_p - \mathbf{u}_e \quad (6.7)$$

where we have introduced the parameters  $\delta \equiv m_e / M$  and  $\epsilon \equiv c / \omega_M L_0$ ,  $\nu_{p/e} = \mu_{p/e} / (n_0 M v_A L_0)$ ,  $r_{ep/pe} = \frac{B_0^2}{4\pi M n_0 L_0} R_{ep/pe}$  and  $\omega_M = \sqrt{4\pi e^2 n / M}$  is related to the plasma proton frequency  $\omega_{cp} = \sqrt{4\pi e^2 n / m_p}$  as  $\omega_M = \omega_{cp} \sqrt{m_p / M}$ . Note that in the limit of electron inertia equal to zero, we obtain  $\omega_M = \omega_{cp}$ , and therefore  $\epsilon = \epsilon_H = c / \omega_{cp} L_0$  which is the usual Hall parameter.

Using the definition of the hydrodynamic velocity field

$$\mathbf{u} \equiv \frac{m_p \mathbf{u}_p + m_e \mathbf{u}_e}{m_p + m_e} = (1 - \delta) \mathbf{u}_p + \delta \mathbf{u}_e \quad (6.8)$$

we can readily show the relations between the hydrodynamic variables and the velocity of each species as

$$\mathbf{u}_p = \mathbf{u} + \delta \epsilon \mathbf{j} \quad (6.9)$$

$$\mathbf{u}_e = \mathbf{u} - (1 - \delta) \epsilon \mathbf{j} \quad (6.10)$$

The plasma fluid equation, is the sum of the corresponding equations of motion (6.5) and (6.6),

$$\frac{d\mathbf{u}}{dt} = \mathbf{j} \times [\mathbf{B} - \delta(1 - \delta)\epsilon^2 \nabla^2 \mathbf{B}] + \nabla p + \nu \nabla^2 \mathbf{u} + \nu_0 \nabla^2 \mathbf{j} \quad (6.11)$$

where  $p \equiv p_p + p_e$  is the hydrodynamic pressure,  $\nu = \nu_p + \nu_e$  and  $\nu_0 = \nu_p \delta \epsilon - \nu_e \delta (1 - \delta) \epsilon$ . On the other hand, the equation of motion for electrons (6.6), using  $\mathbf{E} = -\partial_t \mathbf{A} - \nabla \phi$  and

$(\mathbf{u}_e \cdot \nabla)\mathbf{u}_e = \boldsymbol{\omega}_e \times \mathbf{u}_e + \nabla(u_e^2/2)$  (with  $\boldsymbol{\omega}_e = \nabla \times \mathbf{u}_e$ ) can be turn into

$$\begin{aligned} \frac{\partial}{\partial t}(\mathbf{A} - \delta\epsilon\mathbf{u}_e) &= \mathbf{u}_e \times (\mathbf{B} - \delta\epsilon\boldsymbol{\omega}_e) + \\ &+ \nabla(\epsilon p_e + \delta\epsilon\frac{u_e^2}{2} - \phi) - \nu_e\nabla^2\mathbf{u}_e - \eta\mathbf{j} \end{aligned} \quad (6.12)$$

where we have modeled  $R_{ep} = \eta\mathbf{j}$ .

We define,

$$\mathbf{B}' \equiv \mathbf{B} - \delta\epsilon\boldsymbol{\omega}_e = \mathbf{B} - (1 - \delta)\delta\epsilon^2\nabla^2\mathbf{B} - \delta\epsilon\boldsymbol{\omega} \quad (6.13)$$

where  $\boldsymbol{\omega} = \nabla \times \mathbf{u}$  is the hydrodynamic vorticity. Taking the curl of equation (6.12), it is possible to obtain a dynamical equation for the magnetic field

$$\partial_t \mathbf{B}' = \nabla \times [\mathbf{u} - (1 - \delta)\epsilon\mathbf{j}] \times \mathbf{B}' - \nu_e\epsilon\nabla^2\boldsymbol{\omega} + \eta\nabla^2\mathbf{B} - \nu_e\epsilon^2(1 - \delta)\nabla^4\mathbf{B} \quad (6.14)$$

We consider electron inertia (and the resulting momentum transport due to the electrons)

Just as in three-dimensional Hall-MHD, the electron inertia Hall-MHD model has three ideal invariants in the ideal case, namely, the energy and the generalized helicities

$$E = \int d^3r \left( \sum_s m_s n_s \frac{u_s^2}{2} + \frac{B^2}{8\pi} \right), \quad (6.15)$$

$$H_{p/e} = \int d^3r \left( \mathbf{A} + \frac{cm_{p/e}}{q_{p/e}}\mathbf{u}_{p/e} \right) \cdot \left( \mathbf{B} + \frac{cm_{p/e}}{q_{p/e}}\boldsymbol{\omega}_{p/e} \right) \quad (6.16)$$

where  $\boldsymbol{\omega}_{p/e} = \nabla \times \mathbf{u}_{p/e}$ . Note that in the Hall-MHD limit (i.e.  $\delta \rightarrow 0$ ), the conservation of the ion helicity and electron helicity yields the conservation of the hybrid helicity and magnetic helicity respectively.

## 6.2 2.5D Setup

In a 2.5D setup, the vector fields depend on two coordinates, say  $x$  and  $y$  but they maintain three components. Considering the incompressible case, i.e.  $\nabla \cdot \mathbf{u} = 0$ , we can write the magnetic and velocity fields as

$$\mathbf{B} = \nabla \times [\hat{\mathbf{z}} a(x, y, t)] + \hat{\mathbf{z}} b(x, y, t) \quad (6.17)$$

$$\mathbf{u} = \nabla \times [\hat{\mathbf{z}} \varphi(x, y, t)] + \hat{\mathbf{z}} u(x, y, t) \quad (6.18)$$

## 6. Beyond the Hall effect: electron inertia

where  $a(x, y, t)$  and  $\varphi(x, y, t)$  are the scalar potential for the magnetic and velocity fields respectively. In terms of these scalar potentials, the equations (6.11) and (6.14) take the form

$$\partial_t \omega = [\varphi, \omega] - [a, j] - (1 - \delta)\delta\epsilon[b, \nabla^2 b] + \nu\nabla^2\omega + \nu_0\nabla^4 b \quad (6.19)$$

$$\partial_t u = [\varphi, u] - [a, b] - (1 - \delta)\delta\epsilon[j, b] + \nu\nabla^2 u + \nu_0\nabla^2 j \quad (6.20)$$

$$\partial_t a' = [\varphi - (1 - \delta)\delta\epsilon^2 b, a'] + \eta\nabla^2 a + \nu_e\epsilon^2(1 - \delta)\nabla^4 a + \nu\epsilon\nabla^2 u \quad (6.21)$$

$$\partial_t b' = [\varphi - (1 - \delta)\delta\epsilon^2 b, b'] + [u - (1 - \delta)\epsilon j, a'] + \eta\nabla^2 b + \nu\epsilon\nabla^2(b - b') \quad (6.22)$$

where

$$\omega = -\nabla^2\varphi \quad (6.23)$$

$$j = -\nabla^2 a \quad (6.24)$$

$$a' = a + (1 - \delta)\delta\epsilon^2 j - \delta\epsilon u \quad (6.25)$$

$$b' = b - (1 - \delta)\delta\epsilon^2\nabla^2 b - \delta\epsilon\omega \quad (6.26)$$

and the nonlinear terms are the standard Poisson brackets, i.e.  $[p, q] = \partial_x p \partial_y q - \partial_y p \partial_x q$ . The set of equations (6.19) - (6.22) describe the dynamical evolution of the magnetic and velocity fields. When  $\delta = 0$  this set of equations reduces to the incompressible 2.5D HMHD equations.

### 6.2.1 Linear modes

Retaining the linear terms in the incompressible system of equations (6.19)-(6.22) it is possible to obtain a dispersion relationship

$$[\sigma^2(1 + (1 - \delta)\delta\epsilon^2 k^2) - k^2 \cos^2(\theta_{kB})]^2 = \sigma^2\epsilon^2 k^2(2\delta - 1) \quad (6.27)$$

where  $\theta_{kB}$  is the angle between the propagation vector and the magnetic field. The solution of equation (6.27) yields the normal modes of oscillation of the equations (6.19)-(6.22).

Figure 6.1 shows the different modes of propagation of waves in EIHMHD, for  $\theta_{kB} = 0$ ,  $\epsilon = 0.1$ ,  $\delta = 4/100$ . The negative branch represents the shear ion-cyclotron waves, and converges to the ion cyclotron frequency as in HMHD. The top branch corresponds to the whistler branch and, in contrast to HMHD, it has a maximum value given by the electron cyclotron frequency  $\omega_{ce}$ . The fact that the linear modes have bounded frequencies represents an advantage, from the numerical point of view, with respect to the unbounded dispersion relation in HMHD. The maximum frequency in EIHMHD implies a minimum time-step in the numerical integration scheme which is independent of the spatial resolution  $\Delta t = 1/\omega_{max} = 2/\omega_{ce}$ . Instead, in HMHD, the whistler branch implies a  $k$ -dependent maximum frequency  $\omega_{max} \sim k_{max}^2$  and so the minimum time-step in the numerical integration scheme (CFL condition) depends on the spatial resolution,  $\Delta t = 1/\omega_{max} \sim 1/k_{max}^2 \sim \Delta x^2$ . Interestingly then, HMHD is more

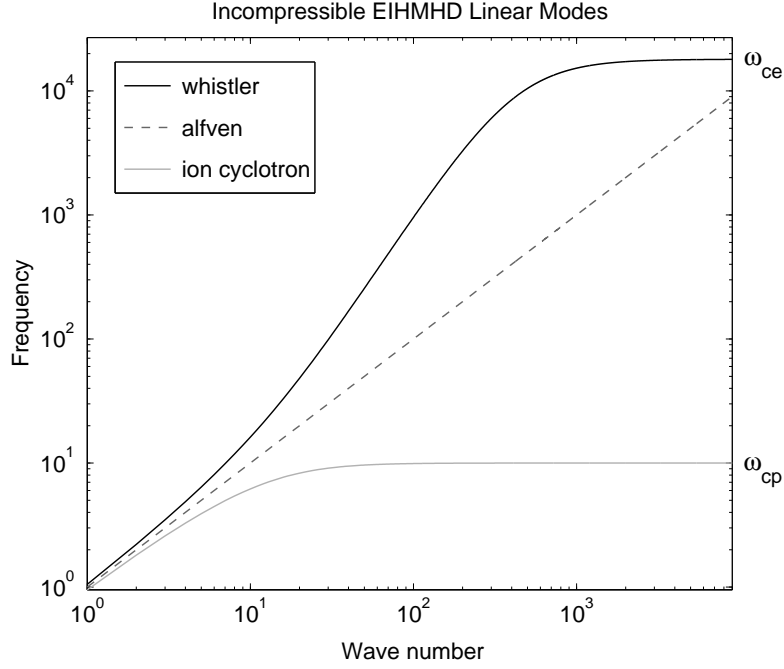


Figure 6.1: Different linear modes in Eihmhd model for a realistic ratio of ion mass to electron mass,  $\theta_{kB} = 0$  and  $\epsilon = 0.1$ .

demanding in terms of numerical integration in time as the spatial resolution is increased, as compared to the more complete EIHMHd model.

### 6.2.2 Ideal invariants in 2.5D

In a 2.5D setup, the total energy, electron and proton helicity can be written as (in dimensionless form)

$$\begin{aligned}
 E &= \int d^3r \left[ (1 - \delta) \frac{u_p^2}{2} + \delta \frac{u_e^2}{2} + \frac{B^2}{2} \right] = \\
 &= \frac{1}{2} \int d^3r [ |\nabla\varphi|^2 + u^2 + |\nabla a|^2 + b^2 + \\
 &\quad (1 - \delta)\delta\epsilon^2 |\nabla b|^2 + (1 - \delta)\delta\epsilon^2 j^2 ] \tag{6.28}
 \end{aligned}$$

$$\begin{aligned}
 H_p &= \int d^2r \{ ab + \\
 &\quad ((1 - \delta)\epsilon) [(u + \delta\epsilon j)b + a(\omega - \delta\epsilon\nabla^2 b)] + \\
 &\quad ((1 - \delta)\epsilon)^2 [(u + \delta\epsilon j)(\omega - \delta\epsilon\nabla^2 b)] \} \tag{6.29}
 \end{aligned}$$

$$\begin{aligned}
 H_e &= \int d^2r \{ ab - \\
 &\quad (\delta\epsilon) [(u - (1 - \delta)\epsilon j)b + a(\omega + (1 - \delta)\epsilon\nabla^2 b)] + \\
 &\quad (\delta\epsilon)^2 [(u - (1 - \delta)\epsilon j)(\omega + (1 - \delta)\epsilon\nabla^2 b)] \} \tag{6.30}
 \end{aligned}$$

## 6. Beyond the Hall effect: electron inertia

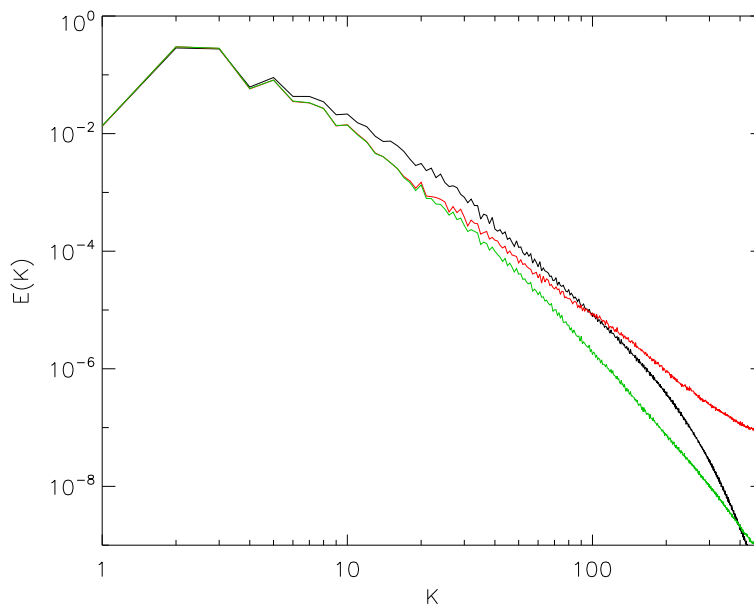


Figure 6.2: Energy spectra for  $\delta = 0$  and  $\epsilon = 0$  (black line, MHD case),  $\delta = 0$  and  $\epsilon = 1/10$  (red line, Hall-MHD case), and  $\delta = 4/100$  and  $\epsilon = 1/10$  (green line, EIHMH case)

We performed 2.5D EIHMH simulations using a pseudo-spectral code, which yields exponentially fast numerical convergence and negligible numerical dissipation. The accuracy of the numerical scheme is tested by looking at the behavior of the ideal invariants of the EIHMH equations in time. The only non-zero invariant, the total energy, is conserved by the numerical scheme with an error of less than  $10^{-8}$ .

### 6.3 Preliminary results for turbulence

Consider the 2.5D EIHMH equations, for different values of  $\epsilon$  and  $\delta$ , and  $\nu, \nu_0, \nu_e$ . Note interestingly that the presence of non-zero  $\nu_e$  introduce high order derivative terms ( $\nabla^4$  terms in the equations), acting as hyperviscosity terms. This certainly has an impact at large values of  $k$ , affecting the distribution of energy at the small scales and the dissipation range.

The energy spectrum for these preliminary simulations is shown in figure 6.2. The impact of the electron inertia at the small scales can already be observed in these results. In particular, we want to understand whether the phenomena on these small scales can be well described by a theory of continuous media (two fluid) without recourse to the more demanding kinetic theory. This will help us to understand the nature of the physical phenomena on these scales and in particular the relevance for energy dissipation mechanisms.

## Concluding remarks and perspectives

We have developed a new tool to characterize systems where both the Hall effect and a strong mean magnetic field are relevant. This model consists of a system of reduced Hall-MHD (RHMHD) equations derived from the incompressible Hall MHD following the same asymptotic procedure, which is employed to obtain the conventional RMHD from MHD. The main advantage of this model lies in the drastic reduction of computational cost. Also we have implemented minor modifications to the model to describe the compressibility effects.

Then we compare the general compressible Hall-MHD model and the RHMHD system, and found a perfectly degree of agreement when the different assumptions of RHMHD, like spectral anisotropy, are satisfied. Nevertheless, when the initial conditions are isotropic but the mean magnetic field is maintained strong, the results differ at the beginning but asymptotically reach a good agreement at relatively short times, also we show that the parallel fluctuations do not grow up in time. We also found evidence that the compressibility still plays a role in the dynamics of these systems, and the weak compressible RHMHD model is able to capture these effects. In conclusion the RHMHD model is a valid approximation of the Hall MHD turbulence in the relevant physical context. The model reproduces the global magnitudes, the energy spectrum and it is able to generate all the scales. Therefore we can say that this is a robust model for study the dynamics of this kind of systems.

In the study of global magnitudes, we have seen two effects that occur simultaneously as the Hall coefficient is increased: the decrease in the dissipation and the delay in reaching the maximum point (and hence the time that it takes to develop all the scales). The first effect have a direct impact on the dissipation scale of the respective flows while the second shows how the Hall term modifies its characteristic times.

Regarding energy spatial distribution. As the Hall parameter is increased the energy spectrum is steeper at intermediate scales preceding the dissipation range. At the same time there

## 7. Concluding remarks and perspectives

---

is an increase in the energy on scales smaller (larger  $K$ ) than the dissipation range (and consequently an increase in the number of scales where the dynamics is developed). The effect of the Hall term is then twofold: first there is a slow down of the energy transfer up to the Hall scale, resulting in a steeper spectrum, and then there seems to be a driving of energy from the Hall length up to the small scales. This is corroborated by a shift in the effective dissipation scale to larger scales (this is manifested as a decrease in the global dissipation values). The longer time to reach the peak of dissipation is explained from the increase on the number of effective scales on which the dynamics occurs. The Hall term affects the total width of the dissipation range decreasing mildly the  $K_{diss}$  (and therefore mildly increasing the dissipation scale) and extending the range of dissipation up to smaller scales with increase of the  $\epsilon$ . The delay suffered by the dissipation peak is due to the development of a greater number of scales in the dissipative range due to a major accumulation of energy in these scales.

Current sheets (fundamental structures for energy dissipation) seem to be affected in two ways by increasing the Hall effect. First, widening of the sheet and secondly an internal filamentation. In the case where the Hall term is sufficiently intense, the current sheet is fully delocalized. These results are complementary to the results observed in the spectra and global magnitudes and corroborate the idea that the Hall effect results in an effective shift of the dissipation scale (current sheet thickness getting larger) but also an increase in the dynamical scale range (increase of filamentation).

We did a quantification of the level of intermittency through both PDFs and structure functions. As the Hall coefficient  $\epsilon$  is increased, the structure functions steepen at scales smaller than the ion-skin depth. Consistently, the Hall term steepens the scaling of the energy spectrum. This is precisely what causes accumulation of energy in smaller scales (dissipation scales) and the subsequent generation of a greater number of scales which would explain the observed filamentation of the current sheets.

The velocity and magnetic field scaling exponents approach a linear behavior characteristic of a self-similar (non-intermittent) flows. This result is confirmed by an analysis of PDFs of velocity and magnetic field increments and spatial derivatives. This show that the Hall effect reduces intermittency in the velocity and magnetic fields.

In the magnetohydrodynamic limit we recover the usual results with the magnetic field being more intermittent than the velocity field, which is consistent with observations of large-scale fluctuations in the solar wind, and with numerical simulations of MHD turbulence at higher spatial resolution.

It is important to note that our results reproduce observations that indicated that while large scales are compatible with multifractal intermittent turbulence, small scales show non-

---

Gaussian self-similarity.

We carried out a cancellation analysis (and an analysis of fractality) of the fields with the aim of pointing out the effect of the Hall term on the topology of the small scales structures and in particular to quantify the effect on structures like current sheets.

Results show that as the Hall term is increased the fractal dimension of the current and vorticity sheets decreases. This observation, together with previous analysis, provided us a comprehensive description of the effect of the Hall force on the formation and modifications of structures. With this analysis we confirm that the Hall effect affects current sheets mainly in two ways. On one hand, the current (and vorticity) sheets widen, while on the other hand they unravel, reaching a more complex topology. This fragmentation (which could be seen as formation of “micro-sheets”) turns out to be more and more evident as the Hall effect increases. This is a quantitative proof of what we had initially interpreted from the simple qualitative evidence. Now we are sure that the nonlinear Hall term is responsible for disruption and unraveling of the MHD current sheets, and for the generation of small scale structures.

Study of the cancellation exponents and of the fractality of the flow show us that magnetic and velocity fields are decoupled in the MHD range, so that their structures have different topological properties (this is consistent with the result obtained regarding the intermittency). When we turn our attention to the range of scales smaller than the ion skin depth, where the Hall term becomes relevant, we found very similar results for both current and vorticity, suggesting that velocity and magnetic fields decouple only in the MHD range.

If no Hall cascade is present, the small scale range is characterized by smooth fluctuations for all components of the fields, as expected when dissipation is active and numerically well resolved. As the Hall effect comes into play, the scaling of the partition function indicates the presence of strongly persistent structures, in the range of scales larger than the typical dissipative scales. In terms of fractal dimension, a decrease is observed from  $D_{\perp} = 3$  to  $D_{\perp} \simeq 2.4$ , indicating that the smooth fields in the MHD regime are developing toward more complex, broken structures as the Hall term coefficient increases, confirming that the turbulent structures are being fragmented by the nonlinear Hall cascade.

*Although at small scales in the solar wind several kinetic effects may play important roles, we found that a simple Hall magnetofluid reproduces some of observations. The Hall effect modifies the transfer of energy across scales, slowing down the transfer of energy from the large scales up to the Hall scale (ion skin depth) and carrying faster the energy from the Hall scale to smaller scales. The final outcome is an effective shift of the dissipation scale to larger scales but also a development of smaller scales. Current sheets (fundamental*

## 7. Concluding remarks and perspectives

---

*structures for energy dissipation) are affected in two ways by increasing the Hall effect, with a widening but at the same time generating an internal structure within them. In the case where the Hall term is sufficiently intense, the current sheet is fully delocalized. In the presence of the Hall effect, field fluctuations at scales smaller than the ion skin depth show a substantial decrease in the level of intermittency, with close to monofractal scaling. The decrease of the fractal dimension is a manifestation of the emerging microscales, while the widening of the macroscale of the sheet produces an increase of the filling factor of these microstructures, and the subsequent reduction of the observed intermittency.*

*Finally, we have also considered the equations for two – fluid dynamics, not neglecting the electron mass. This leads to the newly introduced EIHMD equations. Preliminary results for this system, indicates the presence of new important parameters at the electron scales, and modification of the energy spectrum at small scales.*